Shape-Memory Effect in Bulk and Thin-Film Polycrystals

Thesis by

Yi-Chung Shu

In Partial Fulfillment of the Requirements
for the Degree of
Doctor of Philosophy

California Institute of Technology
Pasadena, California

1999

(Submitted September 14, 1998)

© 1999
Yi-Chung Shu
All Rights Reserved

Acknowledgements

I would like to begin by expressing my gratitude to my advisor, Professor Kaushik Bhattacharya, for his invaluable advice and constant encouragement over the past four years. His extreme enthusiasm for the subject has always been an inspiration for me. His guidance and training has instilled a sense of confidence in my future scientific pursuits.

I thank Professor James K. Knowles who has always been there to offer me direction and encouragement. I thank Professor Michael Ortiz for his generous support on all aspects of my research. I thank Professor Guruswaminaidu Ravichandran for his great help in many direct and indirect ways. I thank Professors Oscar P. Bruno, William L. Johnson and Rob Phillips for participating in my education through graduate school and teaching me the importance of being clear, concise, and composed. I thank Professor Brent Fultz for his invaluable time taken in my thesis defense and constructive comments on its content.

I am indebted to Professor Stefan Müller for his invitation to Max-Planck-Institute for Mathematics in the Sciences in Germany and for sharing with me some of his insights. I am grateful for helpful discussions with Professors Andrea Braides, Irene Fonseca, Gilles Francfort and Robert V. Kohn. I also thank Drs. Jenö Beyer and Lie Zhao for kindly allowing me to use their experimental data in Section 3.3.1.

I would like to thank all of my friends for their support through my graduate career. With their kindness and friendship, my life at Caltech has been an enjoyable one. In particular, I thank Dr. Xiaoguang Zhong for his sincere encouragement and suggestions; I thank Nancy Winfree for always being a valuable source of technical advice; and I thank Dr. Ali Taheri for his many useful discussions.

Finally, I am deeply grateful to my wife, Shujuan, and my family for their infinite patience and support, and for continually helping me keep things in perspective.

Abstract

Shape-memory effect (SME) is a phenomenon where deformation suffered below a critical temperature can be recovered on heating. About 20-30 alloys are known to exhibit SME in single crystals. However, the degree to which they retain their shape-memory behavior in polycrystals is widely varied. In particular, Ti-Ni and Cu-Zn-Al undergo cubic to monoclinic transformation and recover similar strains as single crystals; yet, the observed shape-memory behavior in the former is much better than that in the latter. We develop a model based on energy minimization to understand this difference. Using this model, we establish that texture is the very important reason why the strains recoverable in Ti-Ni are so much larger than those in Cu-based shape-memory alloys in rolled, extruded and drawn specimens. We find that even the qualitative behavior of combined tension-torsion can critically depend on the texture. The results are in good agreement with experimental observations.

We extend our analysis to the behavior of very thin films with three competing length scales: the film thickness, the length scales of heterogeneity and material microstructure. We start with three-dimensional nonhomogeneous nonlinear elasticity enhanced with an interfacial energy of the van der Waals type, and derive the effective energy density as all length scales tend to zero with given limiting ratios. We do not require any priori selection of asymptotic expansion or ansatz in deriving our results. Depending on the dominating length scale, the effective energy density can be identified by three procedures: averaging, homogenization and thin-film limit. We apply our theory to martensitic thin films and use a model example to show that the shape-memory behavior can crucially depend on the relative magnitudes of these length scales. Using this theory, we show that sputtering textures in both Ti-Ni and Cu-based shape-memory thin films are not favorable for large recoverable strain. We comment on multilayers made of shape-memory and elastic materials.

Finally, we suggest textures for improved SME in bulk and thin-film polycrystals.

Contents

Acknowledgements **iii**

Abstract **v**

1 Introduction **1**

1.1 Martensitic Phase Transformation 3

1.2 Single Crystals 4

1.3 Bulk Polycrystals 5

1.4 Thin Films 7

2 Continuum Model **9**

2.1 Geometrically Linear Theory 9

2.2 Well Structure 12

2.2.1 Tetragonal Martensite 12

2.2.2 Trigonal Martensite 13

2.2.3 Orthorhombic Martensite 13

2.2.4 Monoclinic Martensite 13

2.3 Microstructure 15

3 Shape-Memory Effect in Bulk Polycrystals **19**

3.1 Recoverable Strain and Energy Minimization 19

3.1.1 Recoverable Strain in a Single Crystal 19

3.1.2 Recoverable Strain in a Polycrystal 23

3.1.3 Bounds on Recoverable Strain in a Polycrystal 24

3.2 Maximum Recoverable Strain in Tension and Torsion 27

3.2.1 Extension or Compression 27

3.2.2 Maximum Recoverable Strain in a Laminated Polycrystal . . . 31

3.2.3 Combined Tension-Torsion 35

3.3 Results for Uniaxial Loading 39

3.3.1 Rolling Texture: Comparison with Experimental Observations 39

3.3.2 Rolling Texture: Prediction 42

3.3.3 Other Textures 43

3.4 Results for Combined Tension-Torsion 47

4 Shape-Memory Effect in Thin Films **49**

4.1 Effective Energy of a Thin Film 49

4.2 Mathematical Preliminaries 53

4.3 Strong Interfacial Energy 57

4.4 Film Thickness Much Smaller than Heterogeneity 66

4.5 Film Thickness Comparable to Heterogeneity 76

4.6 Film Thickness Much Larger than Heterogeneity 83

4.7 Recoverable Strain in Polycrystalline Thin Films 84

4.7.1 Model Example 84

4.7.2 Martensitic Thin Films 93

4.8 Multilayers 99

5 Discussion and Conclusion **101**

Bibliography **106**

A Expression of $\mathcal{S}$ **116**

List of Figures

1.1 The shape-memory effect. 5

1.2 A heterogeneous thin film with three different length scales. 7

2.1 The behavior of φ at high and low temperature. Notice that the change of well structure depends on the temperature. 10

2.2 A fine microstructure of $\mathbf{e}^{(1)}$ and $\mathbf{e}^{(2)}$ can accommodate the average strain $\mathbf{e}^{\text{ave}} = \lambda\mathbf{e}^{(1)} + (1-\lambda)\mathbf{e}^{(2)}$ for $0 < \lambda < 1$. 16

3.1 The micro, meso and macro scales in the modeling of shape-memory polycrystals, and the energies at these length scales. 20

3.2 Recoverable strains in a single crystal. Let the plane of the paper be the space of all strains. $\mathbf{e}^{(0)} = \mathbf{0}$ is the stress-free strain of the austenite while $\mathbf{e}^{(1)}, \cdots, \mathbf{e}^{(k)}$ are the stress-free or transformation strains of the martensitic variants. A single crystal can recover all strains in the shaded set $\mathcal{S}$ if all pairs of martensitic variants are compatible. Note that $\mathbf{e}^{(0)}$ is a part of this set as a result of self-accommodation. For a specific loading, the maximum recoverable strain ϵ_R is given by the maximum projection of the set $\mathcal{S}$ on the loading direction. 20

3.3 The set of recoverable strains $\mathcal{S}_{\text{mono}}$ in a single crystal undergoing cubic-monoclinic transformation. This nonconvex set $\mathcal{S}_{\text{mono}}$ is bounded by orthorhombic and monoclinic estimates. 22

3.4 Recoverable strains in a polycrystal (made of two grains of equal volume fraction). Each grain has its own set of recoverable strains (the two triangles) obtained by a rotation of the basic set $\mathcal{S}$. The polycrystal can recover all strains inside the inner bound $\mathcal{P}_i$, but none outside the outer bound $\mathcal{P}_o$. For a specific loading, the maximum recoverable strain is between ϵ_R^i and ϵ_R^o which are the projections on the loading direction of $\mathcal{P}_i$ and $\mathcal{P}_o$, respectively. ϵ_R^o also has an alternative meaning: it is the average of the maximum recoverable strain of the individual grain. We believe that typically ϵ_R^i is a reasonable estimate while ϵ_R^o is a large overestimate. 24

3.5 Inner and outer bounds of recoverable strain can be wide apart. 27

3.6 The stress-strain curve under the tensile loading. 30

3.7 A rank-two laminate containing four orientations $\mathbf{R}_i$ and $i = 1, \cdots, 4$. . . 31

3.8 Maximum recoverable strain for the rank-two laminates subjected to uniaxial tension in different directions. (a) Ti-40Ni-10Cu (B19) (b) γ_1' Cu-14Al-4Ni (wt.%). 35

3.9 Constraints from neighboring grains can suppress the most favorably oriented variant. Volume fractions of the different orthorhombic variants in the grains with orientation R_2 for the case $\theta = 60°$. (a) Ti-40Ni-10Cu (B19) (b) γ_1' Cu-14Al-4Ni (wt.%). 36

3.10 Directions in a rolled sheet and texture observed by Zhao and Beyer. . . 40

3.11 Comparison of theory and experiment for the Zhao-Beyer texture. Here, • Expt is the measured recoverable strain. OB, IE and IB mean outer bound ϵ_R^o, inner estimate ϵ_R^e, and inner bound ϵ_R^i, respectively. (a) ideal texture (b) texture with 5° wobble. 41

3.12 Comparison of theory and experiment for the Inoue-Miwa-Inakazu textures. Here, • Expt is the measured recoverable strain. OB, IE and IB mean outer bound ϵ_R^o, inner estimate ϵ_R^e, and inner bound ϵ_R^i, respectively. (a) PL-CR specimens with $\{111\}\langle uvw\rangle$ texture (b) PL-RX specimens with $\langle 110\rangle$ partial fiber with components from $\{111\}\langle 110\rangle$ to $\{110\}\langle 110\rangle$. 42

3.13 The predicted uniaxial recoverable extension in Ti-Ni for various rolling textures. The upper dashed line is the inner estimate ϵ_R^e while the lower continuous line is the inner bound ϵ_R^i. 44

3.14 The predicted uniaxial recoverable extension in Cu-Zn-Al for various rolling textures. The upper dashed line is the inner estimate ϵ_R^e while the lower continuous line is the inner bound ϵ_R^i. 45

3.15 The predicted recoverable torsion (normalized twist) for different applied extension in Ti-Ni and Cu-Zn-Al polycrystals with random texture, $\langle 110 \rangle$ and $\langle 100 \rangle$ fiber textures, respectively. Notice that torsion (normalized twist) means outer radius times angle of twist. Here, IE and IB mean inner estimate γ_R^e and inner bound γ_R^i. 48

4.1 (a) The sequence that minimizes the energy with density $\varphi^{(1)}$ for $\alpha' \geq 0$. Here the darkly shaded and white regions represent $\mathbf{F}_1^{(1)}$ and $\mathbf{F}_2^{(1)}$ defined by (4.99), respectively. (b) The sequence that minimizes the energy with density $\varphi^{(2)}$ only for $\alpha' = 0$. Here the darkly shaded and white regions represent $\mathbf{F}_1^{(2)}$ and $\mathbf{F}_2^{(2)}$ defined by (4.101), respectively. (c) The sequence that minimizes the energy with density $\varphi^{(2)}$ for $\alpha' \geq 0$. Here the darkly shaded and white regions represent $\mathbf{F}_1^{(2)}$ and $\mathbf{F}_2^{(2)}$ defined by (4.101), respectively. 82

4.2 (a) A polycrystalline thin film with the texture containing two orientations. (b) The test field $\nabla\eta$. The darkly shaded regions form the support of $\nabla\eta$ and the straight lines within them are level sets of η. (c) The test divergence-free flow $\mathbf{g}$. The darkly shaded strips form the support of $\mathbf{g}$ and the arrows within them point out the direction of the flow. (d) The test field $\nabla\eta$ when $\beta = \beta_0 = \frac{1}{2}\cot\theta$. The darkly shaded regions form the support of $\nabla\eta$ and the straight lines within them are level sets of η. (e) The recoverable strain $(= \frac{1}{2}|\mathcal{P}|)$ versus different values β. (f) The behavior of $\bar{\varphi}(\xi)$ for ξ near zero with different values β. Notice that $\bar{\varphi}(\xi)$ grows quadratically if $\beta > \beta_0$, becomes flat (zero) if $\beta < \beta_0$, and has an exact cubic growth near the origin if $\beta = \beta_0$. 89

4.3 The effective behavior of a multilayer thin film is determined by the energies above for small and large values of $\frac{\kappa}{h}$. 99

List of Tables

1.1 Experimental observations of the recoverable strains in some Cu-based SMAs and Ti-Ni. 2

2.1 Transformation strains associated with different changes of symmetry. Only $\mathbf{e}^{(1)}$ is shown here; the rest $\mathbf{e}^{(2)}, \cdots, \mathbf{e}^{(k)}$ can be obtained from $\mathbf{e}^{(1)}$ by symmetry by permuting the basis. The symmetry of the austenite is cubic. We choose variant 1 so that $\delta > 0$ (orthorhombic and monoclinic cases) and $\epsilon > 0$ (monoclinic case). The compositions of all alloys are given in atomic percentages unless otherwise specified. 15

3.1 Orientation, normals and volume fraction of the rank-two laminates used in the calculation for Ti-40Ni-10Cu (B19) and γ_1' Cu-14Al-4Ni (wt.%). . . . 34

3.2 Some common texture fibers observed in BCC metals and alloys. The α-fiber II is the characteristic texture of Ti-Ni with the B2-lattice. 43

3.3 The predicted uniaxial recoverable extension for various textures in bulk polycrystals. 46

4.1 Summary of the effective behavior of a heterogeneous thin film. **A** means averaging, **H** means homogenizing and **T** means thin-film limit. "**TH**" denotes that the effective energy density $\bar{\varphi}$ is obtained by taking thin-film limit first, and then homogenizing in the plane of the film. On the other hand, "**HT**" denotes homogenization first followed by thin-film limit. Finally, a stacked symbol $\overset{\mathbf{H}}{\mathbf{T}}$ denotes performing these operations simultaneously. . . 51

4.2 The predicted uniaxial recoverable extension for various textures. ϵ_R^∞ and ϵ_R^0 are the inner estimate and inner bound for films with $\beta = \infty$ and $\beta = 0$, respectively. 98

Chapter 1 Introduction

Shape-memory effect (SME) is a phenomenon where deformation suffered below a critical temperature can be recovered on heating. About 20-30 alloys are known to exhibit SME in single crystals. However, the degree to which they retain their shape-memory behavior in polycrystals is widely varied. Some materials have good shape-memory behavior as single crystals but little or none as polycrystals, while others display good SME even as polycrystals. Typically, shape-memory materials are prepared by casting followed by hot-working (rolling for strips or drawing for wires) followed by heat treatment. Therefore, it is natural to expect that the polycrystals are textured and this has been experimentally confirmed by various groups: Eucken and Hirsch [34], Li *et al.* [54], Mulder *et al.* [66], Inoue *et al.* [43], Kitamura *et al.* [45], Zhao and Beyer [100, 101] for Ti-Ni rolled sheets; Willemse *et al.* [98] and Yamauchi *et al.* [99] for Ti-Ni-Cu wires and Ti-Ni rods; Park and Bunge [79, 80, 81] for Cu-Zn-Al rolled sheets; and Park *et al.* [82] for Cu-Zn-Al drawn wires. It is also natural to expect textures in thin films prepared by rapid solidification [34, 35, 33, 27] and sputtering [40, 96]. The purpose of this thesis is to develop a theoretical framework and use it to understand the effect of texture on the shape-memory effect in bulk and thin-film polycrystals.

After some preliminaries in Chapter 2, we explore the effect of texture on SME in bulk specimens such as sheets, strips, wires and tubes in Chapter 3. We use "recoverable strain" as a measure of SME and develop a model to estimate it for a polycrystal with given texture. We note that the strains recoverable by superelasticity or pseudoelasticity are essentially identical to those recoverable by SME; so our model also provides a means to evaluate the effect of texture on superelasticity.

Our model is based on a framework developed by Bhattacharya and Kohn [11]. Using their framework, they argue that crystallographic symmetry is a very important factor in determining the recoverable strains in polycrystals: alloys which undergo

SMA	Recoverable Strain	
	Single Crystals	Polycrystals
Cu-Zn-Al Cu-Al-Ni	2-9% depending on orientation [76, 83]	around 2% in general [13, 53, 91, 70], but can be up to 6% in textured ribbons [34, 28]
Ti-Ni	3-10% depending on orientation [61, 90]	5-8% in drawn wires and rolled sheets [64, 84, 87, 55]

Table 1.1: Experimental observations of the recoverable strains in some Cu-based SMAs and Ti-Ni.

small change in symmetry (cubic to tetragonal or trigonal) have virtually no recoverable strains in polycrystals, while alloys which undergo large change in symmetry (cubic to orthorhombic or monoclinic) always recover at least some strain even in polycrystals. While this explains much experimental observation, it fails to make any distinction within the latter group of alloys. In particular, it is unable to explain why Ti-Ni is so much better than Cu-based shape-memory alloys (SMAs) (Table 1.1) since both undergo cubic to monoclinic transformation. They speculated on, but did not systematically explore, the role of texture. We show that texture is a very important reason for the difference between Ti-Ni and Cu-based SMAs: the texture that develops during rolling or drawing is very desirable from the point of view of SME in Ti-Ni while these textures are undesirable in Cu-based alloys. Finally, we explore in some detail the predicted recoverable strains for various textures in an attempt to recommend textures for large SME.

We extend these ideas to the behavior of very thin films in Chapter 4. Shape-memory materials have the largest energy output per unit volume per cycle of known actuator systems [51]. This fact, together with the enhanced rate of heat transfer in thin films, makes these alloys ideal for microactuator, micropump and for microelectromechanical system (MEMS) applications and this has motivated many experimental efforts (see for example [44, 59, 42, 52, 24, 23]). All of these efforts have concentrated on Ti-Ni-based alloys and use sputtering to produce polycrystalline films. However, it is not clear that Ti-Ni is the ideal material since the sputtering texture may be very different. More importantly the microstructure of martensite can be significantly different in thin films as compared to bulk materials. We develop a framework to understand the microstructure and behavior of heterogeneous thin films by combining the homogenization results of Braides [15], Müller [67] and Francfort and Müller [37] with the 3D-2D asymptotic analysis of Bhattacharya and James [10]. We find that sputtering textures in both Ti-Ni and Cu-based SMAs are not favorable for large recoverable strain. This is consistent with experimental observations. We also use this theory to explore multilayered films and the novel properties that they may possess.

We conclude in Chapter 5 with a discussion.

1.1 Martensitic Phase Transformation

The source of the SME is a martensitic phase transformation. It is a first order, diffusionless and solid-to-solid phase transformation. The lattice has different structure at high and low temperature and the change in lattice structure is sudden. There is no diffusion or rearrangement of atoms during transformation and one can obtain one structure by a deformation of the other. The transformation is usually hysteretic, but it is possible to define a thermodynamic transformation temperature Θ_c where both phases are equally stable (energetically favorable). The high temperature phase is called *austenite* while the low temperature phase *martensite.*

The key feature of a martensitic phase transformation is the microstructure it generates. In SMAs, the high temperature austenite phase is cubic while the low temperature martensite phase typically has smaller symmetry. This gives rise to symmetry-related *variants* of martensite and these variants often form microstructure or fine-scale mixtures. Ball and James [5, 6] have proposed a theoretical approach to model these fine phase mixtures based on the minimization of the free energy. We follow their approach but use the geometrically linear rather than nonlinear theory to derive quantitative results. Some shape-memory alloys can recover strains up to 10%, so it may be questionable whether we can use such a small-strain theory. The extension to geometrically nonlinear theory is conceptionally straightforward though operationally inaccessible at this time. Further, we believe that our main conclusions remain valid even in the nonlinear theory. An extensive discussion on the differences between geometrically linear and nonlinear theories can be found in [9].

1.2 Single Crystals

Consider a single crystal specimen at the temperature above Θ_c shown in Figure 1.1(a). It is in the austenite phase with a cubic lattice. On cooling, it transforms to the martensite with a different lattice structure as shown in Figure 1.1(b). However, the variants of martensite arrange themselves in a way that there is no macroscopic shape change. This is known as *self-accommodation.* When a load is applied to the crystal, it deforms if it can by rearranging the microstructure. In Figure 1.1(c), the new microstructure is obtained by converting one variant to another. The resulting deformation appears macroscopically plastic: there is no restoring force since all the variants are equally energetically favorable. However, this deformation is recovered on heating because the material reverts to the unique austenite irrespective of the martensitic microstructure. This is the *shape-memory effect.* The deformation is recovered because it is accomplished not by slip or motion of dislocations but by rearrangement of the microstructure.

Notice that not all deformations are recoverable. Suppose we have deformed the crystal till it has accommodated all strain if it can by rearranging variants (as in Figure 1.1(c)). If we further deform the crystal, elastic stresses build up and this provides a restoring force for the incremental deformation till the plastic limit of the martensite. Beyond that, there is true plastic deformation by slip and the incremental deformation is unrecoverable.

Thus, the strains that are recoverable in a single crystal are exactly those that are associated with microstructures of martensite. This is characterized by the set $\mathcal{S}$ of recoverable strains in a single crystal shown schematically in Figure 3.2. We provide an energetic basis for this argument in Chapter 2 and 3.

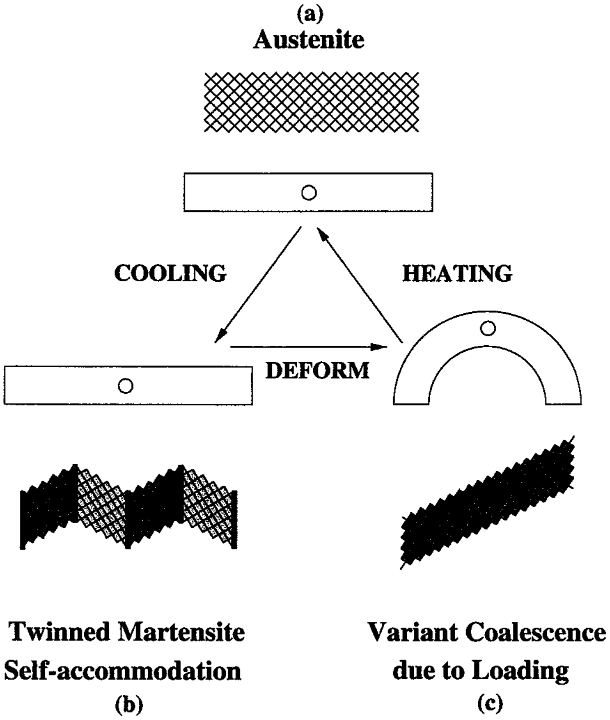

Figure 1.1: The shape-memory effect.

1.3 Bulk Polycrystals

Next consider a polycrystal consisting of a large number of grains with different orientations. At low temperature, each grain deforms by rearranging its microstructure. However, it can not do so freely because of the constraints of the neighboring grains. In other words, each grain has its own set of recoverable strains $\mathcal{S}(\mathbf{x})$ (which is obtained by "rotating" the basic set $\mathcal{S}$ through the orientation of the grain $\mathbf{x}$). A recoverable strain field in a polycrystal is a possibly inhomogeneous strain field that is recoverable in each grain. We characterize it using the set of recoverable strains in a polycrystal $\mathcal{P}$. We also provide an energetic basis for $\mathcal{P}$ in Chapter 3.

However, this set $\mathcal{P}$ is very difficult to calculate. Further, its calculation requires the knowledge of the shape and orientation of each grain which is difficult to obtain. Finally, even if we measure the exact texture and solve the problem for a specific specimen, the resulting set is valid only for that specimen; we have to repeat the process for each specimen. Therefore, we need an easily computable, but reasonable estimate of this set which can use readily measurable and characterizable information about the texture. We accomplish this using bounds – the inner or the Taylor bound and the outer or the Sachs bound. The inner bound is obtained by imposing the same strain on each grain while the outer bound is obtained by ignoring compatibility between grains. All these are shown schematically in Figure 3.4.

We specialize to specific loads in Section 3.2. We consider uniaxial tension or compression as an example of homogeneous loading and combined tension-torsion as an example of inhomogeneous loading. We show that under uniaxial loading of single crystals, our model essentially coincides with that of Saburi and Nenno [86]. In polycrystals, we again provide an inner bound and an outer bound of the recoverable strain. For monoclinic martensites, we also provide an inner estimate.

We believe that the inner bound is in fact a reasonable estimate of the actual recoverable strains. We provide examples to justify this in Section 3.2.2. Bhattacharya and Kohn [12] as well as Kohn and Niethammer [48] have derived rigorous results in dimensionally reduced problems to support this argument. Therefore, we use the inner bound, which can be rewritten as a linear programming problem (3.16) and (3.17), as our fundamental tool for evaluating the effect of texture.

The outer bound, on the other hand, often is a large over-estimate. In uniaxial tension, the outer bound is the average of the strain of the most favorable martensitic variant in each grain. Various authors [66, 45] have used this as a model for the recoverable strain and have predicted almost twice the observed recoverable strain.

We use our models to explore the effect of texture on recoverable strains in uniaxial tension in Section 3.3 and in combined tension-torsion in Section 3.4. Recently Zhao and Beyer [100, 101] as well as other groups [66, 43, 45] have measured both the recoverable strain and the texture of rolled Ti-Ni and closely related materials. We calculate the recoverable strains for their observed texture and find good agreement with their observations in Section 3.3.1. Ti-Ni and Cu-based alloys, and in fact, most SMAs have a parent phase whose crystal structure is almost body-centered-cubic (BCC). We calculate recoverable strains for typical BCC rolling and drawing textures,

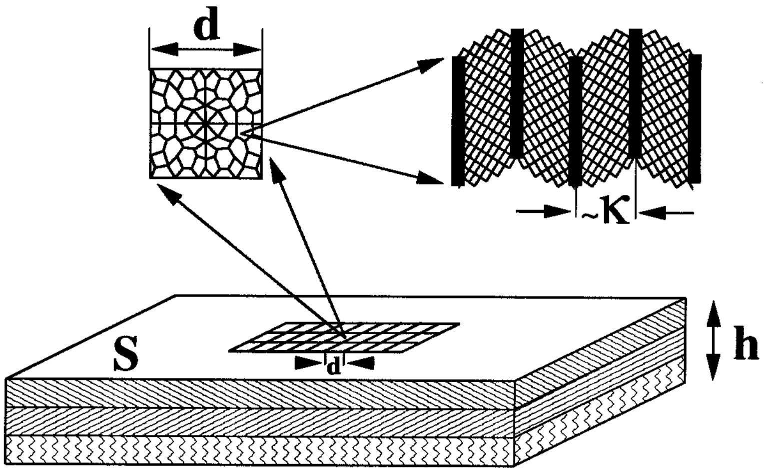

Figure 1.2: A heterogeneous thin film with three different length scales.

and also for textures formed by rapid solidification. Figure 3.13 and Figure 3.14 highlight the striking contrast in SME between Ti-Ni and Cu-based alloys in rolling textures. The results for various other textures are shown in Table 3.3. In Section 3.4, we find that even the qualitative behavior of combined tension-torsion can depend on the texture as shown in Figure 3.15.

1.4 Thin Films

The mechanism of the shape-memory effect in thin-film polycrystals is very similar to that in bulk polycrystals. However, the nature of the microstructure and the effective behavior can be very different in thin films as interfacial energy and surface relaxation effect become very important. Much of Chapter 4, Section 4.1 to 4.6, is devoted to developing a theoretical framework for studying the effect of varying length scales that arise in thin films on microstructure and behavior. Depending on the deposition technique, the size of grains (d) within the film can be larger than, comparable to or smaller than the thickness of film (h). Furthermore, depending on the material, the length scale of microstructure ($\approx \kappa$) can also be larger than, comparable to or smaller than that of grains (d). These length scales are shown in Figure 1.2.

We apply our mathematical results to study SME in Section 4.7. We use examples to show that the shape-memory behavior of martensitic films can crucially depend on the limiting ratios of these length scales. For the case of strong interfacial energy (i.e., $\kappa >> d$), the shape-memory behavior is expected to be negligible in general polycrystals since materials can not form microstructures within each grain to accommodate deformation. On the other hand, for small interfacial energy (i.e., $\kappa << d$), materials can form microstructures freely and our model example exploring the whole range of $\frac{h}{d}$ shows that this set $\mathcal{P}$ significantly depends on the ratio of $\frac{h}{d}$. We further consider cubic-monoclinic shape-memory thin films. For flat grains ($d >> h$), the intergranular constraints are mainly in-plane; any out-of-plane incompatibility is easily overcome with very small elastic energy. While for long grains ($d << h$), it is no longer possible to overcome out-of-plane constraints. Therefore, the intergranular constraints are fully three-dimensional. Table 4.2 contrasts the behavior of films with long or rod-like grains and films with flat or pancake shaped grains. It shows that recoverable strains in films with flat columnar grains differs from (are larger than) those with long columnar grains.

Finally, we consider a multilayer thin film made of a finite number of alternating layers of a martensitic material and a purely elastic material. We find quite different behavior when $\frac{\kappa}{h}$ tends to zero and infinity. We conclude that such a multilayer thin film provides an opportunity to design materials with unusual transformation properties.

Chapter 2 Continuum Model

2.1 Geometrically Linear Theory

Consider a single crystal and choose the undistorted austenite state at temperature Θ_c as the reference configuration. Let it occupy the bounded domain $\Omega \in I\!R^3$ in this reference configuration. A deformation of the crystal is characterized by the function $\mathbf{y} : \Omega \to I\!R^3$. We assume that the specimen remains free of defects such as cracks or dislocations and therefore we assume that the deformation $\mathbf{y}$ is continuous and its gradient $\nabla \mathbf{y} : \Omega \to I\!M^{3\times 3}$ exists a.e. in Ω where $I\!M^{m\times n}$ is the set of all $m \times n$ matrices.

Our basic modeling postulate states that the specimen will occupy the state that minimizes its total energy given by

$$\int_{\Omega} \varphi(\nabla \mathbf{y}(\mathbf{x}), \Theta) d\mathbf{x} \tag{2.1}$$

where $\varphi : I\!M^{3\times 3} \times I\!R^+ \to I\!R^+ \cup \{0\}$ is the (Helmholtz) free energy density at temperature Θ.

In much of this thesis, we work with a geometrically linear theory, and here it is conventional to use the displacement $\mathbf{u} = \mathbf{y} - \mathbf{x}$ rather than the deformation, displacement gradient $\nabla \mathbf{u} = \nabla \mathbf{y} - \mathbf{I}$, and *strain* $\mathbf{e}[\mathbf{u}] = \frac{1}{2}(\nabla \mathbf{u} + (\nabla \mathbf{u})^T)$. So, with an above notation, the free energy density $\varphi = \varphi(\nabla \mathbf{u}, \Theta)$. Frame-indifference in this theory implies that the free energy density φ is invariant under infinitesimal rotations. It follows that φ depends only on the strain or the symmetric part of the displacement gradient and

$$\begin{aligned} \varphi(\mathbf{H}, \Theta) &= \varphi(\mathbf{e}[\mathbf{H}], \Theta), \\ \mathbf{e}[\mathbf{H}] &= \frac{1}{2}(\mathbf{H} + \mathbf{H}^T). \end{aligned} \tag{2.2}$$

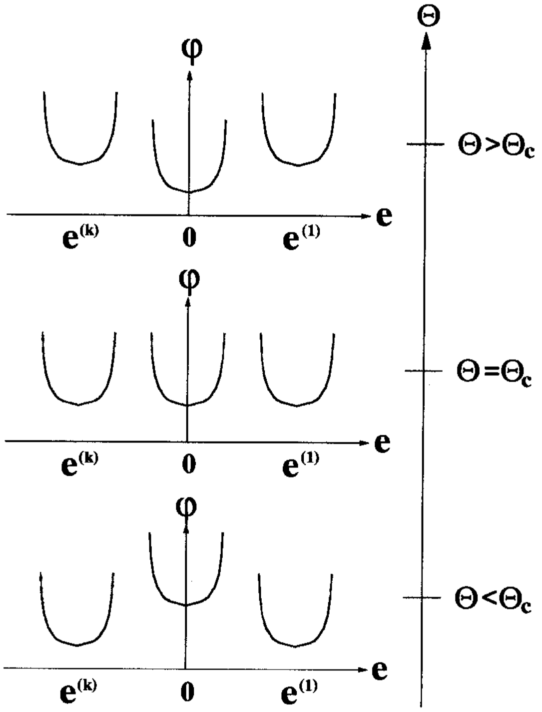

Figure 2.1: The behavior of φ at high and low temperature. Notice that the change of well structure depends on the temperature.

We further expect φ to reflect the symmetry which the material may possess. Thus, we assume that the free energy density is unaffected by the point group (strictly speaking the Laue group) of the material at its high temperature state, $\mathcal{P}^0$ [31, 32]. The point group is the set of rotations that map a lattice back to itself. It follows

$$\varphi(\mathbf{e}, \Theta) = \varphi(\mathbf{R}^T \mathbf{e} \mathbf{R}, \Theta) \tag{2.3}$$

for all $\mathbf{R} \in \mathcal{P}^0$ and for all symmetric $\mathbf{e}$.

Austenite is the stable phase above Θ_c. So we expect the zero matrix $\mathbf{0}$ to minimize φ for $\Theta > \Theta_c$. Recall that the martensitic transformation is diffusionless and hence there is a strain matrix $\mathbf{e}^{(1)}$, known as the *Bain strain* or *transformation strain* which takes the austenite to the martensite. Since martensite is the stable phase below Θ_c, we expect $\mathbf{e}^{(1)}$ to minimize the energy φ for $\Theta < \Theta_c$. Finally, we expect both $\mathbf{0}$ and $\mathbf{e}^{(1)}$ to minimize φ at $\Theta = \Theta_c$ (see Figure 2.1).

Material symmetry (2.3) implies the existence of other minimizers besides $\mathbf{e}^{(1)}$ below Θ_c. Indeed, let $\mathbf{e}^{(i)}$ be the minimizers of φ and k be the total number of variants. They can be determined by

$$\{\mathbf{e}^{(1)}, \cdots, \mathbf{e}^{(k)}\} = \{\mathbf{R}^T \mathbf{e}^{(1)} \mathbf{R}, \quad \forall \mathbf{R} \in \mathcal{P}^0\} \tag{2.4}$$

and

$$k = \frac{\text{order of the point group of the austenite}}{\text{order of the point group of the martensite}}.$$

Putting all this together,

$$\begin{array}{lll} \varphi(\mathbf{f}, \Theta) \leq \varphi(\mathbf{g}, \Theta) & \text{for all } \mathbf{f} \in \mathcal{A} & \Theta > \Theta_c, \\ \varphi(\mathbf{f}, \Theta) \leq \varphi(\mathbf{g}, \Theta) & \text{for all } \mathbf{f} \in \mathcal{A} \cup \mathcal{M} & \Theta = \Theta_c, \\ \varphi(\mathbf{f}, \Theta) \leq \varphi(\mathbf{g}, \Theta) & \text{for all } \mathbf{f} \in \mathcal{M} & \Theta < \Theta_c, \end{array} \tag{2.5}$$

for all $\mathbf{g} \in I\!M^{3\times 3}$ where

$$\mathcal{A} = \{\mathbf{I} + \mathbf{W} : \mathbf{W} = -\mathbf{W}^T\}, \tag{2.6}$$

$$\mathcal{M}_i = \{\mathbf{e}^{(i)} + \mathbf{W} : \mathbf{W} = -\mathbf{W}^T\}, \tag{2.7}$$

$$\mathcal{M} = \mathcal{M}_1 \cup \mathcal{M}_2 \cdots \cup \mathcal{M}_k. \tag{2.8}$$

We call $\mathcal{A}$ the *austenite well*, $\mathcal{M}_i$ the ith *martensite well*, and $\mathcal{M}$ the collection of all martensite wells.

If we treat the austenite and each variant of martensite as linearly elastic materials, then φ has the form (see Figure 2.1)

$$\varphi(\mathbf{e}, \Theta) = \min_{i=0,1,\cdots,k} \left\{ \frac{1}{2}(\mathbf{e} - \mathbf{e}^{(i)}) \cdot \mathbf{A}^{(i)}(\mathbf{e} - \mathbf{e}^{(i)}) + w^{(i)}(\Theta) \right\} \tag{2.9}$$

where $i = 0$ refers to the austenite, and $i = 1, \cdots, k$ to the martensitic variants, $\mathbf{A}^{(i)}$ is the elastic modulus and $w^{(i)}(\Theta)$ controls the relative stability of the phases depending on temperature. The variants of martensite are symmetry-related, so $w^{(1)} = \cdots = w^{(k)}$.

2.2 Well Structure

All known martensites exhibiting the shape-memory effect have cubic lattice structure in the austenite. So we choose an orthonormal basis parallel to the cubic axes, the *cubic basis*, to describe the well structure of four common martensites below. We also note that the 24 elements of the point group $\mathcal{P}^0$ of a cubic Bravais lattice are

$$\begin{gathered}\mathbf{I}, \mathbf{R}^{\frac{\pi}{2}}(\hat{\mathbf{e}}_i), \mathbf{R}^{\pi}(\hat{\mathbf{e}}_i), \mathbf{R}^{\frac{3\pi}{2}}(\hat{\mathbf{e}}_i), \mathbf{R}^{\pi}(\frac{1}{\sqrt{2}}(\hat{\mathbf{e}}_i \pm \hat{\mathbf{e}}_j)),\\ \mathbf{R}^{\frac{2\pi}{3}}(\frac{1}{\sqrt{3}}(\hat{\mathbf{e}}_1 \pm \hat{\mathbf{e}}_2 \pm \hat{\mathbf{e}}_3)), \mathbf{R}^{\frac{4\pi}{3}}(\frac{1}{\sqrt{3}}(\hat{\mathbf{e}}_1 \pm \hat{\mathbf{e}}_2 \pm \hat{\mathbf{e}}_3)),\end{gathered} \tag{2.10}$$

for $i, j = 1, 2, 3, i \neq j$, and $\mathbf{R}^{\theta}(\hat{\mathbf{e}})$ is the proper rotation with $\hat{\mathbf{e}}$ as axis and θ as rotation angle.

2.2.1 Tetragonal Martensite

There are two lattice parameters α, β, and three variants of martensite with transformation strains given by

$$\begin{pmatrix} \alpha & 0 & 0 \\ 0 & \alpha & 0 \\ 0 & 0 & \beta \end{pmatrix}, \begin{pmatrix} \alpha & 0 & 0 \\ 0 & \beta & 0 \\ 0 & 0 & \alpha \end{pmatrix}, \begin{pmatrix} \beta & 0 & 0 \\ 0 & \alpha & 0 \\ 0 & 0 & \alpha \end{pmatrix}.$$

2.2.2 Trigonal Martensite

There are two lattice parameters α, β, and four variants of martensite with transformation strains given by

$$\begin{pmatrix} \beta & \alpha & \alpha \\ \alpha & \beta & \alpha \\ \alpha & \alpha & \beta \end{pmatrix}, \begin{pmatrix} \beta & -\alpha & -\alpha \\ -\alpha & \beta & \alpha \\ -\alpha & \alpha & \beta \end{pmatrix}, \begin{pmatrix} \beta & \alpha & -\alpha \\ \alpha & \beta & -\alpha \\ -\alpha & -\alpha & \beta \end{pmatrix}, \begin{pmatrix} \beta & -\alpha & \alpha \\ -\alpha & \beta & -\alpha \\ \alpha & -\alpha & \beta \end{pmatrix}.$$

2.2.3 Orthorhombic Martensite

There are two kinds of cubic to orthorhombic transformation; we consider only one kind in this thesis since we are unaware of any example of the other. There are three lattice parameters α, β, δ, and six variants of martensite with transformation strains given by

$$\begin{pmatrix} \alpha & \delta & 0 \\ \delta & \alpha & 0 \\ 0 & 0 & \beta \end{pmatrix}, \begin{pmatrix} \alpha & 0 & \delta \\ 0 & \beta & 0 \\ \delta & 0 & \alpha \end{pmatrix}, \begin{pmatrix} \beta & 0 & 0 \\ 0 & \alpha & \delta \\ 0 & \delta & \alpha \end{pmatrix},$$
$$\begin{pmatrix} \alpha & -\delta & 0 \\ -\delta & \alpha & 0 \\ 0 & 0 & \beta \end{pmatrix}, \begin{pmatrix} \alpha & 0 & -\delta \\ 0 & \beta & 0 \\ -\delta & 0 & \alpha \end{pmatrix}, \begin{pmatrix} \beta & 0 & 0 \\ 0 & \alpha & -\delta \\ 0 & -\delta & \alpha \end{pmatrix}.$$

We choose variant 1 so that $\delta > 0$.

2.2.4 Monoclinic Martensite

There are two kinds of cubic to monoclinic transformation. In Monoclinic-I, the axis of monoclinic symmetry corresponds to $\langle 110 \rangle_{\text{cubic}}$ while in Monoclinic-II, the axis of monoclinic symmetry corresponds to $\langle 100 \rangle_{\text{cubic}}$.

Monoclinic-I Martensite

There are four lattice parameters α, β, δ, ϵ, and twelve variants of martensite with transformation strains given by

$$\begin{pmatrix} \alpha & \delta & \epsilon \\ \delta & \alpha & \epsilon \\ \epsilon & \epsilon & \beta \end{pmatrix}, \begin{pmatrix} \alpha & \delta & -\epsilon \\ \delta & \alpha & -\epsilon \\ -\epsilon & -\epsilon & \beta \end{pmatrix}, \begin{pmatrix} \alpha & -\delta & -\epsilon \\ -\delta & \alpha & \epsilon \\ -\epsilon & \epsilon & \beta \end{pmatrix}, \begin{pmatrix} \alpha & -\delta & \epsilon \\ -\delta & \alpha & -\epsilon \\ \epsilon & -\epsilon & \beta \end{pmatrix},$$
$$\begin{pmatrix} \alpha & \epsilon & \delta \\ \epsilon & \beta & \epsilon \\ \delta & \epsilon & \alpha \end{pmatrix}, \begin{pmatrix} \alpha & -\epsilon & \delta \\ -\epsilon & \beta & -\epsilon \\ \delta & -\epsilon & \alpha \end{pmatrix}, \begin{pmatrix} \alpha & -\epsilon & -\delta \\ -\epsilon & \beta & \epsilon \\ -\delta & \epsilon & \alpha \end{pmatrix}, \begin{pmatrix} \alpha & \epsilon & -\delta \\ \epsilon & \beta & -\epsilon \\ -\delta & -\epsilon & \alpha \end{pmatrix},$$
$$\begin{pmatrix} \beta & \epsilon & \epsilon \\ \epsilon & \alpha & \delta \\ \epsilon & \delta & \alpha \end{pmatrix}, \begin{pmatrix} \beta & -\epsilon & -\epsilon \\ -\epsilon & \alpha & \delta \\ -\epsilon & \delta & \alpha \end{pmatrix}, \begin{pmatrix} \beta & -\epsilon & \epsilon \\ -\epsilon & \alpha & -\delta \\ \epsilon & -\delta & \alpha \end{pmatrix}, \begin{pmatrix} \beta & \epsilon & -\epsilon \\ \epsilon & \alpha & -\delta \\ -\epsilon & -\delta & \alpha \end{pmatrix}.$$

We choose variant 1 so that $\delta > 0$ and $\epsilon > 0$.

Monoclinic-II Martensite

There are four lattice parameters α, β, δ, ϵ, and twelve variants of martensite with transformation strains given by

$$\begin{pmatrix} \alpha+\epsilon & \delta & 0 \\ \delta & \alpha-\epsilon & 0 \\ 0 & 0 & \beta \end{pmatrix}, \begin{pmatrix} \alpha+\epsilon & -\delta & 0 \\ -\delta & \alpha-\epsilon & 0 \\ 0 & 0 & \beta \end{pmatrix}, \begin{pmatrix} \alpha-\epsilon & \delta & 0 \\ \delta & \alpha+\epsilon & 0 \\ 0 & 0 & \beta \end{pmatrix}, \begin{pmatrix} \alpha-\epsilon & -\delta & 0 \\ -\delta & \alpha+\epsilon & 0 \\ 0 & 0 & \beta \end{pmatrix},$$
$$\begin{pmatrix} \alpha+\epsilon & 0 & \delta \\ 0 & \beta & 0 \\ \delta & 0 & \alpha-\epsilon \end{pmatrix}, \begin{pmatrix} \alpha+\epsilon & 0 & -\delta \\ 0 & \beta & 0 \\ -\delta & 0 & \alpha-\epsilon \end{pmatrix}, \begin{pmatrix} \alpha-\epsilon & 0 & \delta \\ 0 & \beta & 0 \\ \delta & 0 & \alpha+\epsilon \end{pmatrix}, \begin{pmatrix} \alpha-\epsilon & 0 & -\delta \\ 0 & \beta & 0 \\ -\delta & 0 & \alpha+\epsilon \end{pmatrix},$$
$$\begin{pmatrix} \beta & 0 & 0 \\ 0 & \alpha+\epsilon & \delta \\ 0 & \delta & \alpha-\epsilon \end{pmatrix}, \begin{pmatrix} \beta & 0 & 0 \\ 0 & \alpha+\epsilon & -\delta \\ 0 & -\delta & \alpha-\epsilon \end{pmatrix}, \begin{pmatrix} \beta & 0 & 0 \\ 0 & \alpha-\epsilon & \delta \\ 0 & \delta & \alpha+\epsilon \end{pmatrix}, \begin{pmatrix} \beta & 0 & 0 \\ 0 & \alpha-\epsilon & -\delta \\ 0 & -\delta & \alpha+\epsilon \end{pmatrix}.$$

Symmetry of Martensite	k	Transformation Strain $\mathbf{e}^{(1)}$	Examples	Measured Parameters
Tetragonal	3	$\begin{pmatrix} \alpha & 0 & 0 \\ 0 & \alpha & 0 \\ 0 & 0 & \beta \end{pmatrix}$	Ni-36.8Al [21, 89]	$\alpha = -0.0608$ $\beta = 0.1302$
Trigonal	4	$\begin{pmatrix} \beta & \alpha & \alpha \\ \alpha & \beta & \alpha \\ \alpha & \alpha & \beta \end{pmatrix}$	Ti-50.5Ni (R-phase) [60]	$\alpha = 0.0047$ $\beta = 0$
Orthorhombic	6	$\begin{pmatrix} \alpha & \delta & 0 \\ \delta & \alpha & 0 \\ 0 & 0 & \beta \end{pmatrix}$	γ_1' Cu-14Al-4Ni (wt.%) [78]	$\alpha = 0.0425$ $\beta = -0.0822$ $\delta = 0.0194$
			Ti-40Ni-10Cu (B19) [69]	$\alpha = 0.0240$ $\beta = -0.0420$ $\delta = 0.0310$
Monoclinic-I	12	$\begin{pmatrix} \alpha & \delta & \epsilon \\ \delta & \alpha & \epsilon \\ \epsilon & \epsilon & \beta \end{pmatrix}$	Ti-49.8Ni [46, 77]	$\alpha = 0.0243$ $\beta = -0.0437$ $\delta = 0.0580$ $\epsilon = 0.0427$
			Ti-45Ni-5Cu [69]	$\alpha = 0.0232$ $\beta = -0.0410$ $\delta = 0.0532$ $\epsilon = 0.0395$
Monoclinic-II	12	$\begin{pmatrix} \alpha+\epsilon & \delta & 0 \\ \delta & \alpha-\epsilon & 0 \\ 0 & 0 & \beta \end{pmatrix}$	Cu-15Zn-17Al [22]	$\alpha = 0.0483$ $\beta = -0.0907$ $\delta = 0.0249$ $\epsilon = 0.0383$
			β_1' Cu-14Al-4Ni (wt.%) [75]	$\alpha = 0.0442$ $\beta = -0.0822$ $\delta = 0.0160$ $\epsilon = 0.06$

Table 2.1: Transformation strains associated with different changes of symmetry. Only $\mathbf{e}^{(1)}$ is shown here; the rest $\mathbf{e}^{(2)}, \cdots, \mathbf{e}^{(k)}$ can be obtained from $\mathbf{e}^{(1)}$ by symmetry by permuting the basis. The symmetry of the austenite is cubic. We choose variant 1 so that $\delta > 0$ (orthorhombic and monoclinic cases) and $\epsilon > 0$ (monoclinic case). The compositions of all alloys are given in atomic percentages unless otherwise specified.

We choose variant 1 so that $\delta > 0$ and $\epsilon > 0$.

Table 2.1 lists the measured parameters for some important examples.

2.3 Microstructure

We now explain why martensitic materials form microstructure below the transformation temperature. We show that energy minimization forces a material to form microstructure to accommodate a given boundary condition using the following example. Consider a hypothetical material with only two variants of martensite. So φ is minimized only at $\mathbf{e}^{(1)}$ and $\mathbf{e}^{(2)}$ below Θ_c; i.e.,

$$0 = \varphi(\mathbf{e}^{(1)}) = \varphi(\mathbf{e}^{(2)}) \leq \varphi(\mathbf{e}) \quad \forall \;\; \mathbf{e} \in I\!M^{3\times3}. \tag{2.11}$$

We assume φ satisfies the growth condition

$$\varphi(\mathbf{e}) \leq C(1 + |\mathbf{e}|^p) \tag{2.12}$$

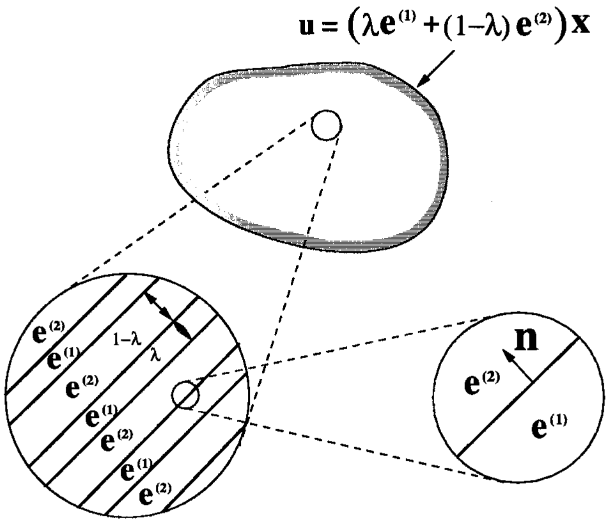

Figure 2.2: A fine microstructure of $\mathbf{e}^{(1)}$ and $\mathbf{e}^{(2)}$ can accommodate the average strain $\mathbf{e}^{\text{ave}} = \lambda \mathbf{e}^{(1)} + (1-\lambda)\mathbf{e}^{(2)}$ for $0 < \lambda < 1$.

for some constant C and for all $\mathbf{e} \in I\!M^{3\times 3}$. Suppose $\mathbf{e}^{(1)}$ and $\mathbf{e}^{(2)}$ are compatible or twin-related; i.e., they satisfy

$$\mathbf{e}^{(1)} - \mathbf{e}^{(2)} = \frac{1}{2}(\mathbf{a} \otimes \mathbf{n} + \mathbf{n} \otimes \mathbf{a}) \tag{2.13}$$

for some $\mathbf{a}$ and $\mathbf{n}$. We assume that the specimen is clamped by the boundary condition

$$\mathbf{u} = \mathbf{e}^{\text{ave}}\mathbf{x}, \qquad \mathbf{e}^{\text{ave}} = \lambda \mathbf{e}^{(1)} + (1-\lambda)\mathbf{e}^{(2)} \tag{2.14}$$

for $\mathbf{x} \in \partial\Omega$ and $0 < \lambda < 1$. We seek to find out energy minimizing deformation below the transformation temperature.

From (2.11), $\varphi(\mathbf{e}^{\text{ave}}) > 0$ if $0 < \lambda < 1$ and $\Theta < \Theta_c$. However, we will show that the material can accommodate such a boundary condition with vanishing total energy by making coherent mixtures of $\mathbf{e}^{(1)}$ and $\mathbf{e}^{(2)}$ as shown in Figure 2.2. Indeed, set

$$\mathbf{f}(\mathbf{x}) = \begin{cases} (1-\lambda)(\mathbf{a}\otimes\mathbf{n})\mathbf{x} + m(\lambda - 1)\mathbf{a} & \text{if } m \le \mathbf{x}\cdot\mathbf{n} < m + \lambda\ , \\ \lambda\,(-\mathbf{a}\otimes\mathbf{n})\,\mathbf{x} + (m+1)\lambda\mathbf{a} & \text{if } m + \lambda \le \mathbf{x}\cdot\mathbf{n} < m + 1 \end{cases}$$

where $m \in \mathbb{Z}$. Now define a sequence of deformations by

$$\mathbf{u}^{(\varepsilon)} = \mathbf{e}^{\mathrm{ave}}\mathbf{x} + \varepsilon\, \mathbf{f}(\frac{\mathbf{x}}{\varepsilon}). \tag{2.15}$$

Clearly, $\mathbf{u}^{(\varepsilon)}$ converges strongly to $\mathbf{e}^{\mathrm{ave}}\mathbf{x}$ in $L^p(\Omega, \mathbb{R}^3)$ as $\varepsilon \to 0$. The associated strain is

$$\mathbf{e}^{(\varepsilon)}(\mathbf{x}) = \frac{1}{2}(\nabla\mathbf{u}^{(\varepsilon)} + (\nabla\mathbf{u}^{(\varepsilon)})^T) = \begin{cases} \mathbf{e}^{(1)} & \text{if } \varepsilon m \leq \mathbf{x}\cdot\mathbf{n} < (m+\lambda)\varepsilon\ , \\ \mathbf{e}^{(2)} & \text{if } (m+\lambda)\varepsilon \leq \mathbf{x}\cdot\mathbf{n} < (m+1)\varepsilon\ . \end{cases}$$

Notice that $\mathbf{e}^{(\varepsilon)}$ converges weakly to $\mathbf{e}^{\mathrm{ave}}$ in $L^p(\Omega, \mathbb{R}^6)$ as $\varepsilon \to 0$. While $\varphi(\mathbf{e}^{(\varepsilon)}(\mathbf{x})) = 0$ a.e. in Ω, this deformation $\mathbf{u}^{(\varepsilon)}$ does not satisfy the boundary condition given by (2.14). Therefore, we introduce the cut-off function $\eta_\varepsilon(\mathbf{x}) \in C_0^\infty(\Omega)$ satisfying

$$0 \leq \eta_i \leq 1, \quad \eta_\varepsilon = 1 \quad \text{in} \quad \Omega_\varepsilon \quad \text{and} \quad |\nabla\eta_\varepsilon| \leq \frac{\nu}{R_\varepsilon} \tag{2.16}$$

where ν is some constant independent of ε, Ω_ε is compactly contained in Ω satisfying

$$R_\varepsilon = \mathrm{dist}(\Omega_\varepsilon, \partial\Omega) = ||\mathbf{u}^{(\varepsilon)} - \mathbf{e}^{\mathrm{ave}}\mathbf{x}||_{L^p(\Omega)}.$$

Since $\mathbf{u}^{(\varepsilon)}$ converges strongly to $\mathbf{e}^{\mathrm{ave}}\mathbf{x}$, we can choose a subsequence of it such that $R_\varepsilon \searrow 0$ as $\varepsilon \to 0$.

Now consider a new sequence defined by

$$\bar{\mathbf{u}}^{(\varepsilon)} = \mathbf{e}^{\mathrm{ave}}\mathbf{x} + \eta_\varepsilon\,(\mathbf{u}^{(\varepsilon)} - \mathbf{e}^{\mathrm{ave}}\mathbf{x}).$$

Obviously, $\bar{\mathbf{u}}^{(\varepsilon)}$ satisfies the boundary condition (2.14). Let $\bar{\mathbf{e}}^{(\varepsilon)}$ be the associated strain and note that $\varphi(\bar{\mathbf{e}}^{(\varepsilon)}) > 0$ if $\mathbf{x} \in \Omega\backslash\Omega_\varepsilon$. However, as $\varepsilon \to 0$, the energy of the specimen converges to zero. Indeed, using the growth condition (2.12), we have

$$\begin{aligned}\int\limits_{\Omega} \varphi(\bar{\mathbf{e}}^{(\varepsilon)})d\mathbf{x} &\leq C \int\limits_{\Omega\backslash\Omega_\varepsilon} \left(1 + |\mathbf{e}^{\mathrm{ave}}|^p + |\mathbf{e}^{(\varepsilon)} - \mathbf{e}^{\mathrm{ave}}|^p + (\frac{\nu}{R_\varepsilon})^p|\mathbf{u}^{(\varepsilon)} - \mathbf{e}^{\mathrm{ave}}\mathbf{x}|^p\right) d\mathbf{x} \\ &\leq C \int\limits_{\Omega\backslash\Omega_\varepsilon} \left(1 + \nu^p + |\mathbf{e}^{\mathrm{ave}}|^p + |\mathbf{e}^{(\varepsilon)} - \mathbf{e}^{\mathrm{ave}}|^p\right) d\mathbf{x}\end{aligned}$$

since $\varphi(\bar{\mathbf{e}}^{(\varepsilon)}(\mathbf{x})) = 0$ if $\mathbf{x} \in \Omega_\varepsilon$. Let ε tend to zero, note that

$$\left|\mathbf{e}^{(\varepsilon)}(\mathbf{x})\right| \leq \max\left(|\mathbf{e}^{(1)}|, |\mathbf{e}^{(2)}|\right),$$

we have $\int\limits_{\Omega} \varphi(\bar{\mathbf{e}}^{(\varepsilon)})\, d\mathbf{x} \xrightarrow{\varepsilon} 0$.

We make two important comments. First, in the example above, we constructed a sequence of deformations where the gradient oscillates very rapidly. Such sequences are examples of *weakly converging sequences.* The rapid oscillations in the gradients model the fine scale coherent microstructure [5, 6] and thus these weakly converging sequences are an ideal tool for studying materials with microstructure.

Second, the energy density in our example above is zero only at $\mathbf{e}^{(1)}$ and $\mathbf{e}^{(2)}$. Yet our specimen was able to have an average strain $\mathbf{e}^{\mathrm{ave}} = \lambda\mathbf{e}^{(1)} + (1-\lambda)\mathbf{e}^{(2)}$ with zero energy. Thus by forming microstructure, the specimen can accommodate with zero energy many more average strains than the martensitic variants.

Chapter 3 Shape-Memory Effect in Bulk Polycrystals

3.1 Recoverable Strain and Energy Minimization

In this section, we describe the general framework of Bhattacharya and Kohn [12] who discuss the behavior of shape-memory polycrystals at three distinct length scales - the length scale of polycrystalline specimen which we call "macroscopic," that of individual grains which we call "mesoscopic" and that of the martensitic domains which we call "microscopic" - as shown schematically in Figure 3.1. We assume that there is a wide separation of length scales: i.e., the martensitic domains are much smaller than the grains and those grains are much smaller than the specimen.

Related work addressing the micromechanics of shape-memory polycrystals includes that of Ono and co-workers [72, 73, 71], Bruno *et al.* [18] and Smyshlyaev and Willis [95].

3.1.1 Recoverable Strain in a Single Crystal

Consider a single crystal of austenite and choose this as the reference configuration, so the austenite has stress-free strain $\mathbf{e}^{(0)} = 0$. As it is cooled, it transforms to martensite. In SMAs, the austenite lattice has cubic symmetry while the martensite lattice has smaller symmetry such as tetragonal, trigonal, orthorhombic or monoclinic symmetry as we described in Section 2.2. This gives rise to k symmetry-related variants of martensite. Schematically, we mark each transformation strain $\mathbf{e}^{(i)}$ as a point $\bullet$ in Figure 3.2.

The total energy of the crystal is given by (2.1) where we call the integrand φ the *microscopic energy.* It is nonconvex, with multi-well structure - one well for each variant and is given by (2.9). We only consider the behavior at some fixed

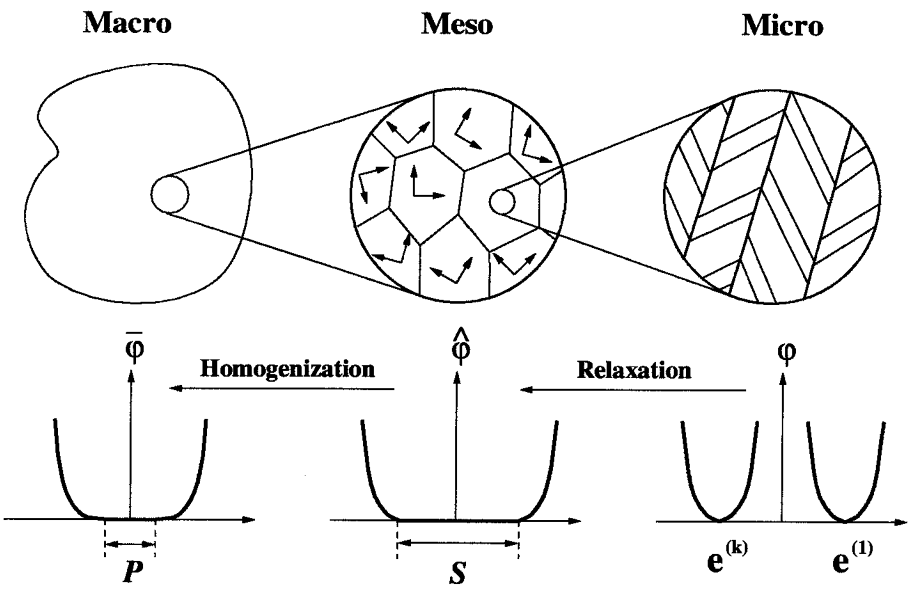

Figure 3.1: The micro, meso and macro scales in the modeling of shape-memory polycrystals, and the energies at these length scales.

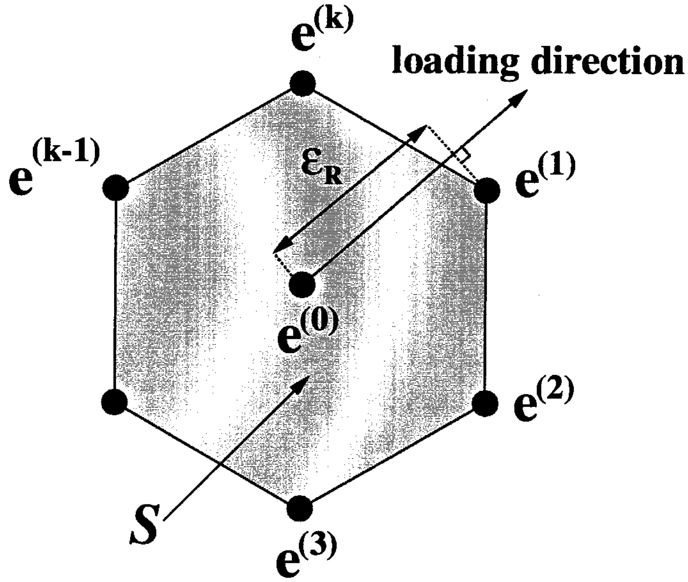

Figure 3.2: Recoverable strains in a single crystal. Let the plane of the paper be the space of all strains. $\mathbf{e}^{(0)} = \mathbf{0}$ is the stress-free strain of the austenite while $\mathbf{e}^{(1)}, \cdots, \mathbf{e}^{(k)}$ are the stress-free or transformation strains of the martensitic variants. A single crystal can recover all strains in the shaded set $\mathcal{S}$ if all pairs of martensitic variants are compatible. Note that $\mathbf{e}^{(0)}$ is a part of this set as a result of self-accommodation. For a specific loading, the maximum recoverable strain ϵ_R is given by the maximum projection of the set $\mathcal{S}$ on the loading direction.

temperature Θ_1 below the transition temperature Θ_c, so we may assume $w^{(1)} = \cdots = w^{(k)} = 0$ and $w^{(0)} > 0$ in (2.9) and omit the temperature dependence in the rest part of this work.

When subjected to some boundary condition, a single crystal generally forms a microstructure of martensitic variants rather than a single variant. Indeed, as we demonstrated in Section 2.3, energy minimization with the multi-well energy (2.9) leads to minimizing sequences which we interpret as microstructure or fine-scale mixtures of variants [5, 6]. Therefore, the behavior of a single crystal is governed not by the microscopic energy, φ, but the *mesoscopic energy* $\hat{\varphi}$. Physically, $\hat{\varphi}(\mathbf{e})$ is the average stored energy when the average strain is $\mathbf{e}$ after taking into account the microstructure. Mathematically, it is obtained by the relaxation of φ and may be defined as

$$\hat{\varphi}(\bar{\mathbf{e}}) = \min_{\mathbf{u}=\bar{\mathbf{e}}\cdot\mathbf{x}\ at\,\partial\Omega} \fint_{\Omega} \varphi(\mathbf{e}[\mathbf{u}])\, d\mathbf{x} \tag{3.1}$$

in which the slashed integral $\fint$ denotes the average over the specimen. The relaxed energy $\hat{\varphi}$ is shown schematically in Figure 3.1. Notice that it is zero on the set $\mathcal{S}$:

$$\mathcal{S} = \{\mathbf{e} : \hat{\varphi}(\mathbf{e}) = 0\}\,. \tag{3.2}$$

This is exactly the set of strains that the material can accommodate by making a mixture of martensitic variants. Thus, the elements of $\mathcal{S}$ are the overall strains which are recoverable for this crystal, and we call $\mathcal{S}$ the *set of recoverable strains for a single crystal.*

We can also give a geometric interpretation for the set $\mathcal{S}$. Suppose two variants are compatible or twin-related; i.e., they satisfy (2.13). Then, as demonstrated in Section 2.3, we can form fine twins whose overall strain is the average of the transformation strains of these two variants. Geometrically, this average strain is a point on the line connecting these two variants, and by choosing the appropriate volume fraction we conclude that all strains on the line joining $\mathbf{e}^{(1)}$ and $\mathbf{e}^{(2)}$ are recoverable.

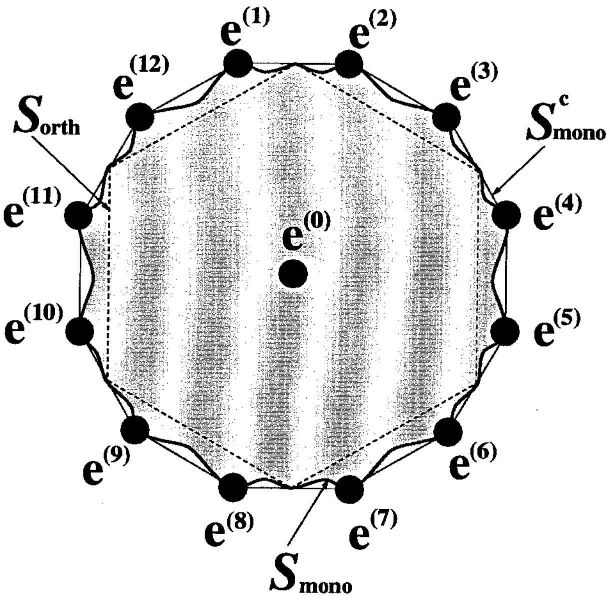

Figure 3.3: The set of recoverable strains $\mathcal{S}_{\text{mono}}$ in a single crystal undergoing cubic-monoclinic transformation. This nonconvex set $\mathcal{S}_{\text{mono}}$ is bounded by orthorhombic and monoclinic estimates.

Furthermore, if all the variants are pair-wise compatible, the set of recoverable strains $\mathcal{S}$ in a single crystal is the convex hull[1] of these stress-free variants as shown in Figure 3.2 [9]. The variants are pair-wise compatible in cubic-tetragonal, cubic-trigonal and cubic-orthorhombic transformation and we can obtain $\mathcal{S}$ easily in these cases; explicit formulas for $\mathcal{S}$ in these cases are given in Appendix A.

In contrast, if all pairs of martensitic variants are not compatible, the set $\mathcal{S}$ is not necessarily the convex hull of the variants. For example, the transformation strains of monoclinic martensites are *not* pair-wise compatible and the set of recoverable strains $\mathcal{S}_{\text{mono}}$ is *not* the convex hull of the stress-free variants. We do not know the precise set $\mathcal{S}_{\text{mono}}$, so we bound it using "orthorhombic" and "monoclinic" estimates as shown in Figure 3.3. Let $\mathcal{S}^{c}_{\text{mono}}$ be the convex hull of the monoclinic variants and let $\mathcal{S}_{\text{orth}}$ be the convex hull of a fictitious cubic-orthorhombic transformation obtained by setting $\epsilon = 0$ in $\mathrm{e}^{(1)}, \cdots, \mathrm{e}^{(12)}$. We can show that $\mathcal{S}_{\text{orth}} \subset \mathcal{S}_{\text{mono}} \subset \mathcal{S}^{c}_{\text{mono}}$ [11, 12]. Explicit formulas for $\mathcal{S}^{c}_{\text{mono}}$ are given in Appendix A.

---

[1] A convex hull of a few points is the smallest polygon that contains all these points.

Finally, shape-memory alloys are self-accommodating: they can undergo the austenite-martensite transformation with no apparent shape change. In other words, there is a microstructure of martensitic variants whose average strain is $\mathbf{e}^{(0)}$ or $\mathbf{e}^{(0)} \in \mathcal{S}$. One can show that any material with cubic austenite that undergoes volume-preserving transformation is self-accommodating [8]. This is certainly the case for SMAs. Therefore, we assume that $\mathbf{e}^{(0)} \in \mathcal{S}$ as in Figure 3.2 and Figure 3.3.

3.1.2 Recoverable Strain in a Polycrystal

We now turn to a polycrystal. A polycrystal is an aggregate of a great number of single crystal grains with different orientations. We describe the texture of a polycrystal by a rotation-valued function $\mathbf{R}(\mathbf{x})$. $\mathbf{R}(\mathbf{x})$ gives the orientation of the crystal at the point $\mathbf{x}$ relative to some fixed reference crystal. In a typical polycrystal, $\mathbf{R}(\mathbf{x})$ is piecewise constant, though we shall not assume any such restriction here.

In order to discuss the behavior of the polycrystal, we introduce the *macroscopic energy* of the polycrystal $\bar{\varphi}$ obtained from $\hat{\varphi}$ by homogenization. Thus, $\bar{\varphi}(\mathbf{e})$ is the average energy of a polycrystal in which the average strain is $\mathbf{e}$. A convenient definition is based on the affine boundary conditions:

$$\bar{\varphi}(\bar{\mathbf{e}}) = \min_{\mathbf{u}=\bar{\mathbf{e}}\cdot\mathbf{x}\ at\,\partial\Omega} \fint_{\Omega} \hat{\varphi}\left(\mathbf{R}^T(\mathbf{x})\mathbf{e}[\mathbf{u}](\mathbf{x})\mathbf{R}(\mathbf{x})\right) d\mathbf{x}\,. \tag{3.3}$$

The macroscopic energy $\bar{\varphi}$ vanishes on the set $\mathcal{P}$ as shown in Figure 3.1. This is exactly the set of strains that can be accommodated in each grain by a mixture of martensitic variants. We define the *set of recoverable strains for a polycrystal*

$$\mathcal{P} = \{\mathbf{e} : \bar{\varphi}(\mathbf{e}) = 0\}\,. \tag{3.4}$$

To understand this set, note that each grain has its own set of recoverable strain $\mathcal{S}(x) = \mathbf{R}(\mathbf{x})\,\mathcal{S}\,\mathbf{R}^T(\mathbf{x})$ which is obtained by the rotation of the basic set $\mathcal{S}$ through $\mathbf{R}(\mathbf{x})$ as shown in Figure 3.4. The elements of $\mathcal{P}$ are the macroscopic strains consistent

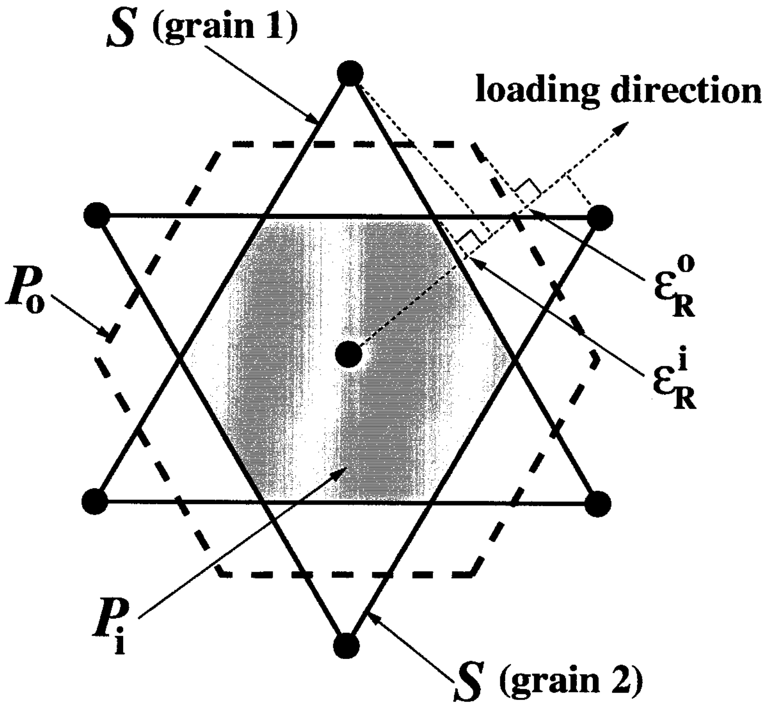

Figure 3.4: Recoverable strains in a polycrystal (made of two grains of equal volume fraction). Each grain has its own set of recoverable strains (the two triangles) obtained by a rotation of the basic set $\mathcal{S}$. The polycrystal can recover all strains inside the inner bound $\mathcal{P}_i$, but none outside the outer bound $\mathcal{P}_o$. For a specific loading, the maximum recoverable strain is between ϵ_R^i and ϵ_R^o which are the projections on the loading direction of $\mathcal{P}_i$ and $\mathcal{P}_o$, respectively. ϵ_R^o also has an alternative meaning: it is the average of the maximum recoverable strain of the individual grain. We believe that typically ϵ_R^i is a reasonable estimate while ϵ_R^o is a large overestimate.

with the point-wise constraint $\mathbf{e}[\mathbf{u}](\mathbf{x}) \in \mathcal{S}(\mathbf{x})$. We can then rewrite the set $\mathcal{P}$ as

$$\mathcal{P} = \left\{ \mathbf{e} : \mathbf{e} = \int\!\!\!\!-_{\Omega} \mathbf{e}[\mathbf{u}](\mathbf{x}) d\mathbf{x}, \;\; \mathbf{e}[\mathbf{u}](\mathbf{x}) \in \mathcal{S}(\mathbf{x}) \text{ for ``every'' } \mathbf{x} \in \Omega \right\}. \tag{3.5}$$

Finally note that $\mathcal{P}$ is not empty in a SMA, since it always contains $\mathbf{e}^{(0)}$ due to self-accommodation.

3.1.3 Bounds on Recoverable Strain in a Polycrystal

We now estimate the set $\mathcal{P}$ using bounds. The first, and what we will find to be the most useful, bound is the *inner bound* or Taylor bound. Consider an average strain $\mathbf{e}$. Suppose $\mathbf{e}$ is recoverable in each grain, i.e., $\mathbf{e} \in \mathcal{S}(\mathbf{x})$ for "every" $\mathbf{x} \in \Omega$. Then, clearly $\mathbf{e}$ is recoverable in the polycrystal or $\mathbf{e} \in \mathcal{P}$. Thus,

$$\mathcal{P} \supset \mathcal{P}_i = \left\{ \mathbf{e} : \mathbf{R}^T(\mathbf{x})\mathbf{e}\mathbf{R}(\mathbf{x}) \in \mathcal{S} \text{ for "every" } \mathbf{x} \in \Omega \right\}. \tag{3.6}$$

The set $\mathcal{P}_i$ is shown in the shaded region of Figure 3.4. Geometrically it is the intersection of the sets of recoverable strains of the different grains. The set $\mathcal{P}_i$ contains all strains that can be recovered without the cooperative effect of the different grains. Hence, it is a pessimistic or inner bound.

The other bound is the *outer bound* or the Sachs bound. This bound is obtained by allowing each grain to deform as it wishes and forgetting about the constraints they impose on each other. Thus,

$$\mathcal{P} \subset \mathcal{P}_o = \left\{ \mathbf{e} : \mathbf{e} = \fint_\Omega \mathbf{e}(\mathbf{x})\, d\mathbf{x} \text{ and } \mathbf{e}(\mathbf{x}) \in \mathcal{S}(\mathbf{x}),\ \mathbf{e}(\mathbf{x}) \text{ not necessarily compatible} \right\}. \tag{3.7}$$

The geometric meaning of this set is harder to visualize. Scale the sets $\mathcal{S}(\mathbf{x})$ for each grain by its own volume fraction. $\mathcal{P}_o$ is the set of all points that can be obtained by adding (vectorically) points in all of these scaled sets as shown in Figure 3.4. The set $\mathcal{P}_o$ does not account for the constraints between grains; hence, it is an optimistic or outer bound.

Finally, from (3.6) and (3.7), it is clear that the inner bound does not depend on the volume fractions of different orientations, but the outer bound does.

There is also an energetic argument for these two bounds. $\mathcal{P}_i$ is the zero set of the constant strain upper bound $\bar{\varphi}_u$ of $\bar{\varphi}$ while $\mathcal{P}_o$ is the zero set of the constant stress lower bound $\bar{\varphi}_l$ of $\bar{\varphi}$. To be precise, the constant-strain test field $\mathbf{u}(\mathbf{x}) = \mathbf{e} \cdot \mathbf{x}$ gives

$$\bar{\varphi}(\mathbf{e}) \leq \bar{\varphi}_u(\mathbf{e}) = \fint_\Omega \hat{\varphi}(\mathbf{R}^T(\mathbf{x})\mathbf{e}\mathbf{R}(\mathbf{x}))\, d\mathbf{x} \tag{3.8}$$

whereas relaxing the compatibility requirement gives

$$\bar{\varphi}(\mathbf{e}) \geq \bar{\varphi}_l(\mathbf{e}) = \min_{\fint \tilde{\mathbf{e}}(\mathbf{x})\, d\mathbf{x} = \mathbf{e}} \fint_{\Omega} \hat{\varphi}(\mathbf{R}^T(\mathbf{x})\tilde{\mathbf{e}}(\mathbf{x})\mathbf{R}(\mathbf{x}))\, d\mathbf{x}\,. \tag{3.9}$$

Let $\mathcal{P}_i = \{\mathbf{e} : \bar{\varphi}_u(\mathbf{e}) = 0\}$ and $\mathcal{P}_o = \{\mathbf{e} : \bar{\varphi}_l(\mathbf{e}) = 0\}$. Since $\bar{\varphi}_l \leq \bar{\varphi} \leq \bar{\varphi}_u$, it follows that

$$\mathcal{P}_i \subset \mathcal{P} \subset \mathcal{P}_o\,. \tag{3.10}$$

We use the names Taylor and Sachs in analogy to polycrystalline plasticity.

It may so happen that the inner and outer bounds are wide apart. This is dramatically illustrated in Figure 3.5. If $\mathcal{S}$ does not span all deviatoric strains, the inner bound reduces to a single point. We say that the inner bound $\mathcal{P}_i$ is trivial in this situation. Bhattacharya and Kohn [12] have argued that the actual set $\mathcal{P}$ is also trivial in such a situation, i.e., $\mathcal{P} = \mathcal{P}_i$. In contrast, if $\mathcal{S}$ spans deviatoric strains, the set $\mathcal{P}_i$ is not trivial. In this case, it is generally not true that $\mathcal{P} = \mathcal{P}_i$. However, we believe that even in this case, $\mathcal{P}_i$ is often a good estimate of $\mathcal{P}$, i.e., $\mathcal{P} \cong \mathcal{P}_i$. We will present examples in support of this claim in Section 3.2.2. Also see the recent work of Kohn and Niethammer [48].

We close this section by recalling the arguments of Bhattacharya and Kohn [11] on the effect of symmetry. If the change of symmetry is small, such as cubic-tetragonal or cubic-trigonal transformation, the set $\mathcal{S}$ has low dimension; hence $\mathcal{P}_i$ is trivial and the polycrystal has no recoverable strains except for exceptional textures. If, on the other hand, the change of symmetry is large, such as cubic-orthorhombic and cubic-monoclinic transformation, the set $\mathcal{S}$ has full dimension. Therefore, the polycrystal has some recoverable strains irrespective of texture.

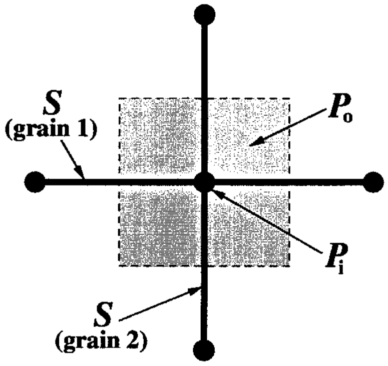

Figure 3.5: Inner and outer bounds of recoverable strain can be wide apart.

3.2 Maximum Recoverable Strain in Tension and Torsion

We now specialize our discussion to maximum recoverable strain under specific loading. We consider uniaxial extension or compression as an example of homogeneous loading and combined tension-torsion as an example of inhomogeneous loading.

3.2.1 Extension or Compression

Consider a polycrystalline SMA below the transformation temperature in the self-accommodated state. Apply a uniaxial stress σ to this specimen in the ξ direction. We will show that the *maximum recoverable strain* ϵ_R is given by

$$\epsilon_R = \begin{cases} \max\limits_{\mathbf{e}\in\mathcal{P}} \left(\xi \cdot \mathbf{e}\xi \right) & \text{if } \sigma > 0 \text{ (extension)}, \\ \min\limits_{\mathbf{e}\in\mathcal{P}} \left(\xi \cdot \mathbf{e}\xi \right) & \text{if } \sigma < 0 \text{ (compression)}. \end{cases} \tag{3.11}$$

The maximum recoverable strain in a single crystal is also given by (3.11) if $\mathcal{P}$ is replaced with $\mathcal{S}$. The formula (3.11) has an interesting geometrical interpretation. The maximum recoverable strain ϵ_R is the maximum projection of the set $\mathcal{P}$ (or $\mathcal{S}$) on the loading direction $\xi \otimes \xi$. In single crystals, it is clear from Figure 3.2 and Figure 3.3 that the maximum projection of the set $\mathcal{S}$ is always equal to the maximum projection of the transformation of strains $\mathbf{e}^{(1)}, \cdots, \mathbf{e}^{(k)}$. Therefore, it follows that variants coalesce under loading to produce the most favorable variant in a single crystal. Thus, our model coincides with that of Saburi and Nenno [86] except they use a geometrically nonlinear theory.

In polycrystals, we can not calculate ϵ_R since we do not know $\mathcal{P}$. However, we can bound it as before using inner and outer bounds. Indeed, let us consider only the tensile loading ($\sigma > 0$). It follows from (3.6), (3.7) and (3.11) that

$$\epsilon_R^i \leq \epsilon_R \leq \epsilon_R^o \tag{3.12}$$

where

$$\epsilon_R^i = \max_{\mathbf{e}\in\mathcal{P}_i} (\xi \cdot \mathbf{e}\,\xi) \qquad \text{and} \qquad \epsilon_R^o = \max_{\mathbf{e}\in\mathcal{P}_o} (\xi \cdot \mathbf{e}\,\xi). \tag{3.13}$$

The inner bound ϵ_R^i assumes that every grain undergoes the same strain and it does not take into account the cooperative response between grains. On the other hand, the outer bound ϵ_R^o assumes that each grain picks its most favorable variant and ignores the fact that the constraints from the neighboring grains can suppress the most favorable variant. We believe that the inner bound is a reasonable estimate of the actual recoverable strain (see Section 3.2.2).

Now consider a polycrystal made of N grains with orientations $\mathbf{R}_1, \mathbf{R}_2, \cdots, \mathbf{R}_N$ and volume fraction $\lambda_1, \lambda_2, \cdots, \lambda_N$. Then, we can further write ϵ_R^i and ϵ_R^o as

$$\epsilon_R^i = \max_{\mathbf{R}_j^T\mathbf{e}\mathbf{R}_j\in\mathcal{S}\ \forall j=1,\cdots,N} (\xi \cdot \mathbf{e}\xi), \tag{3.14}$$

$$\epsilon_R^o = \sum_{j=1}^{N} \max_{\mathbf{e}\in\mathcal{S}} (\lambda_j\, \mathbf{v}_j \cdot \mathbf{e}\, \mathbf{v}_j) \tag{3.15}$$

where $\mathbf{v}_j = \mathbf{R}_j^T \xi$. We can interpret (3.14) and (3.15) geometrically as shown in Figure 3.4: the inner bound is the maximum projection of the set $\mathcal{P}_i$ on the loading direction while the outer bound is the average of the maximum projection of each set $\mathbf{R}_j\, \mathcal{S}\, \mathbf{R}_j^T$ on the loading direction weighted by its volume fraction λ_j. Note also from Figure 3.4 that ϵ_R^i can be strictly smaller than the smallest recoverable strain amongst all grains.

We can also rewrite (3.14) and (3.15) as linear programming problems if $\mathcal{S}$ is the convex hull of stress-free variants. The inner bound,

$$\epsilon_R^i = \max_{\mu_i^j} \left(\sum_{i=1}^{k} \xi \cdot (\mu_i^1 \mathbf{R}_1 \mathbf{e}^{(i)} \mathbf{R}_1^T) \xi \right) \tag{3.16}$$

where the maximum is taken over the following constraints

$$\begin{aligned} \sum_{i=1}^{k} \mu_i^j \mathbf{R}_j \mathbf{e}^{(i)} \mathbf{R}_j^T &= \sum_{i=1}^{k} \mu_i^1 \mathbf{R}_1 \mathbf{e}^{(i)} \mathbf{R}_1^T \quad \text{for } \mathrm{j} = 2, \cdots, \mathrm{N}, \\ \sum_{i=1}^{k} \mu_i^j &= 1, \quad \mu_i^j \geq 0 \quad \text{for } \mathrm{j} = 1, \cdots, \mathrm{N}, \end{aligned} \tag{3.17}$$

and the outer bound

$$\epsilon_R^o = \sum_{j=1}^{N} \lambda_j \left(\max_{\substack{\mu_i \geq 0 \\ \sum_{i=1}^{k} \mu_i = 1}} \xi \cdot \Big(\sum_{i=1}^{k} \mu_i \mathbf{R}_j \mathbf{e}^{(i)} \mathbf{R}_j^T\Big) \xi \right). \tag{3.18}$$

Recall that in the cubic-monoclinic transformation $\mathcal{S}_{\text{mono}}$ is unknown. Therefore, we can not evaluate (3.14). Instead, we use

$$\epsilon_R^i = \max_{\mathbf{R}_j^T \mathbf{e} \mathbf{R}_j \in \mathcal{S}_{\text{orth}}\ \forall j=1,\cdots,N} (\xi \cdot \mathbf{e}\, \xi) \tag{3.19}$$

$$\epsilon_R^e = \max_{\mathbf{R}_j^T \mathbf{e} \mathbf{R}_j \in \mathcal{S}^c_{\text{mono}}\ \forall j=1,\cdots,N} (\xi \cdot \mathbf{e}\, \xi) \tag{3.20}$$

$$\epsilon_R^o = \sum_{j=1}^{N} \max_{\mathbf{e} \in \mathcal{S}^c_{\text{mono}}} (\lambda_j \mathbf{v}_j \cdot \mathbf{e}\, \mathbf{v}_j) \tag{3.21}$$

as the inner bound, inner estimate and outer bound, respectively. We can rewrite equations (3.19) - (3.21) as linear programming problems as before.

Finally, we prove (3.11). Consider a polycrystal subjected to an applied traction $\mathbf{t}$ on the boundary such that $\mathbf{t} = \sigma \mathbf{T} \mathbf{n}$ for some fixed matrix $\mathbf{T}$ where $\mathbf{n}$ is the outward

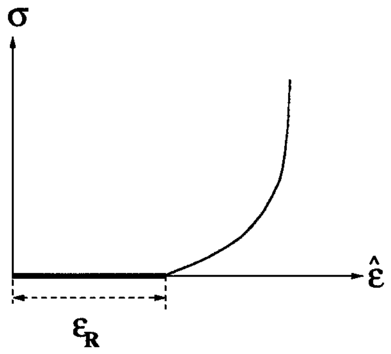

Figure 3.6: The stress-strain curve under the tensile loading.

normal. In the case of the uniaxial loading in the ξ direction, $\mathbf{T}$ has the form of

$$\mathbf{T} = \xi \otimes \xi = \begin{pmatrix} 1 & 0 & 0 \\ 0 & 0 & 0 \\ 0 & 0 & 0 \end{pmatrix} \tag{3.22}$$

in an orthonormal basis $\{\xi, \xi_1^\perp, \xi_2^\perp\}$. The strain field $\hat{\mathbf{e}}_\sigma$ in the specimen minimizes the energy

$$\int_\Omega (\bar{\varphi}(\mathbf{e}[\mathbf{u}]) - \sigma\, \mathbf{e}[\mathbf{u}] \cdot \mathbf{T})\, d\mathbf{x} \tag{3.23}$$

over all compatible strain fields $\mathbf{e}[\mathbf{u}]$. Since $\bar{\varphi}$ is independent of x, there is a solution $\hat{\mathbf{e}}_\sigma$ which is also independent of $\mathbf{x}$. Set $\hat{\epsilon}_\sigma = \hat{\mathbf{e}}_\sigma \cdot \mathbf{T}$. For $\bar{\varphi}$ as shown in Figure 3.1 ($\bar{\varphi} = 0$ on $\mathcal{P}$, $\bar{\varphi} > 0$ outside $\mathcal{P}$, $\bar{\varphi}$ is convex), $\hat{\epsilon}_\sigma$ is of the form shown schematically in Figure 3.6. The maximum recoverable strain ϵ_R is

$$\epsilon_R = \lim_{\sigma \to 0} \hat{\epsilon}_\sigma = (\lim_{\sigma \to 0} \hat{\mathbf{e}}_\sigma) \cdot \mathbf{T}\,. \tag{3.24}$$

From the properties of $\bar{\varphi}$ stated above, it follows that $(\lim_{\sigma \to 0} \hat{\mathbf{e}}_\sigma) \in \mathcal{P}$ and this implies (3.11).

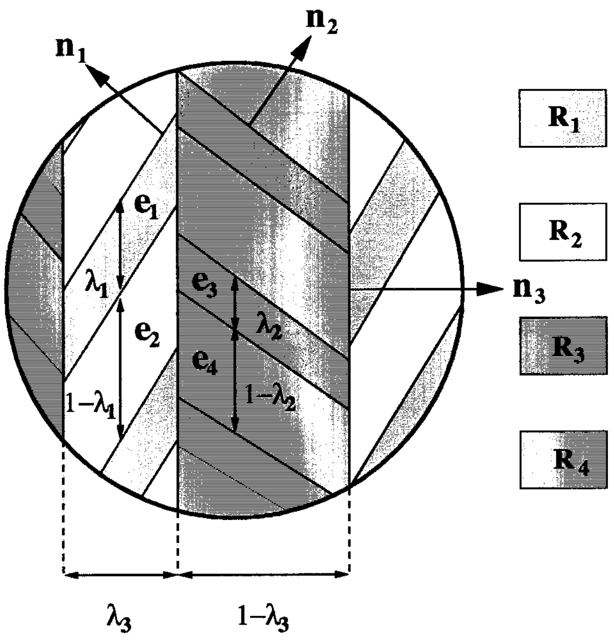

Figure 3.7: A rank-two laminate containing four orientations $\mathbf{R}_i$ and $i = 1, \cdots, 4$.

3.2.2 Maximum Recoverable Strain in a Laminated Polycrystal

We have claimed above that the inner bound provides a reasonable estimate to the actual recoverable strain. We justify that with an example - a polycrystal with a laminated texture. Laminated microstructures have been used extensively in the study of polycrystals and composite materials since the exact effective properties can be obtained by solving an algebraic problem (see for example [57]). We consider the tetragonal and orthorhombic martensites where we know the exact sets $\mathcal{S}_{\text{tetr}}$ and $\mathcal{S}_{\text{orth}}$. A rank-two laminate containing four orientations $\mathbf{R}_i$, $i = 1, \cdots, 4$, is shown in Figure 3.7. Here, $\mathbf{n}_1, \mathbf{n}_2$ and $\mathbf{n}_3$ are the normals of the laminates with the corresponding volume fraction λ_1, λ_2 and λ_3, respectively.

If we assume a wide separation of scales between the two levels of the laminate, it can be shown that the strain is piecewise constant with values $\mathbf{e}_1, \mathbf{e}_2, \mathbf{e}_3$ and $\mathbf{e}_4$ as also shown in Figure 3.7. Kinematic compatibility or coherence forces the following constraints

$$\begin{aligned}
\mathbf{e}_1 - \mathbf{e}_2 &= \frac{1}{2}(\mathbf{n}_1 \otimes \mathbf{m}_1 + \mathbf{m}_1 \otimes \mathbf{n}_1)\,, \\
\mathbf{e}_3 - \mathbf{e}_4 &= \frac{1}{2}(\mathbf{n}_2 \otimes \mathbf{m}_2 + \mathbf{m}_2 \otimes \mathbf{n}_2)\,, \\
(\lambda_1 \mathbf{e}_1 + (1-\lambda_1)\mathbf{e}_2) &- (\lambda_2 \mathbf{e}_3 + (1-\lambda_2)\mathbf{e}_4) = \frac{1}{2}(\mathbf{n}_3 \otimes \mathbf{m}_3 + \mathbf{m}_3 \otimes \mathbf{n}_3)
\end{aligned} \tag{3.25}$$

for some vectors $\mathbf{m}_1, \mathbf{m}_2$ and $\mathbf{m}_3$ and the average strain

$$\mathbf{e}_{\text{ave}} = \lambda_3(\lambda_1 \mathbf{e}_1 + (1-\lambda_1)\mathbf{e}_2) + (1-\lambda_3)(\lambda_2 \mathbf{e}_3 + (1-\lambda_2)\mathbf{e}_4)\,. \tag{3.26}$$

Moreover, to be recoverable, $\mathbf{e}_1$, $\mathbf{e}_2$, $\mathbf{e}_3$ and $\mathbf{e}_4$ must satisfy

$$\mathbf{R}_1^T \mathbf{e}_1 \mathbf{R}_1,\ \mathbf{R}_2^T \mathbf{e}_2 \mathbf{R}_2,\ \mathbf{R}_3^T \mathbf{e}_3 \mathbf{R}_3,\ \mathbf{R}_4^T \mathbf{e}_4 \mathbf{R}_4 \ \in \mathcal{S}\,. \tag{3.27}$$

Putting all these in (3.11), we can conclude that for tensile loading in the ξ direction, the maximum recoverable strain is given by

$$\epsilon_R = \max\ \xi \cdot \mathbf{e}_{\text{ave}}\, \xi \tag{3.28}$$

where the maximum is taken over $\mathbf{e}_1, \mathbf{e}_2, \mathbf{e}_3$ and $\mathbf{e}_4$ subjected to the constraints (3.25) and (3.27).

Tetragonal Martensite

For materials undergoing cubic-tetragonal transformation $\mathcal{S}_{\text{tetr}}$ is given by (A.2); Bhattacharya and Kohn [12] have used it to show that $\mathcal{P}_i$ is trivial unless the polycrystal has $\langle 001 \rangle$ texture. We conjecture following Bhattacharya and Kohn [12] that in a polycrystal with sufficient symmetry, the set $\mathcal{P}$ will be also trivial. We present the following example in support of this conjecture.

Consider a laminated polycrystal undergoing cubic-tetragonal transformation. Set $\mathbf{R}_1 = \mathbf{I}$, $\mathbf{R}_2 = \mathbf{R}_{\mathrm{i}_3}$, $\mathbf{R}_3 = \mathbf{R}_{\mathrm{i}_1}$ and $\mathbf{R}_4 = \mathbf{R}_{\mathrm{i}_1}\mathbf{R}_{\mathrm{i}_3}$ where $\mathbf{R}_{\mathrm{i}_3}$ is a rotation about the axis

$\mathbf{i}_3 = (0, 0, 1)^T$; etc. Further, $\mathbf{n}_1 = \mathbf{i}_3$, $\mathbf{n}_2 = \mathbf{R}_{\mathbf{i}_1}\mathbf{i}_3$ and $\mathbf{n}_3 = \mathbf{i}_1$. The set $\mathcal{P}_i$ is clearly trivial for this polycrystal. We show that the set $\mathcal{P}$ is also trivial; and consequently, the maximum recoverable strain is zero in every direction. Indeed, using $(3.25)_1$, (3.27) and (A.2) gives

$$\mathbf{R}_1^T \mathbf{e}_1 \mathbf{R}_1 = \mathbf{R}_2^T \mathbf{e}_2 \mathbf{R}_2 = \begin{pmatrix} a & 0 & 0 \\ 0 & a & 0 \\ 0 & 0 & -2a \end{pmatrix} \tag{3.29}$$

relative to the self-accommodating state. Similarly, using $(3.25)_2$, (3.27) and (A.2) gives

$$\mathbf{R}_3^T \mathbf{e}_3 \mathbf{R}_3 = \mathbf{R}_4^T \mathbf{e}_4 \mathbf{R}_4 = \begin{pmatrix} b & 0 & 0 \\ 0 & b & 0 \\ 0 & 0 & -2b \end{pmatrix} \tag{3.30}$$

relative to the self-accommodating state. The constraint $(3.25)_3$ forces $a = b = 0$ and this implies $\mathcal{P} = \{0\}$. Using the dual variational principle [12] (or see (4.111)), we can further show that there exists a constant $C > 0$ such that

$$\bar{\varphi}(\mathbf{e}) \geq C\,|\mathbf{e}|^2.$$

Thus, we have a quadratic lower bound and this polycrystal behaves like an elastic material without shape-memory effect. Finally, in this example, we show that $\mathcal{P}$ is trivial for the chosen orientations. If we simply count on the unknowns (degrees of freedom) and constraints in (3.27) and (3.25), there are eight (8) unknowns but nine (9) constraints. So we believe $\mathcal{P}$ is trivial for most orientations unless certain exceptional textures; for example, the texture where all orientations have a common axis perpendicular to $\mathbf{n}_3$ and dimension $\mathcal{P} = 2$ in this case.

SMA	Orientation		Normals			Volume Fraction		
	R_1	R_2	$\mathbf{n}_1$	$\mathbf{n}_2$	$\mathbf{n}_3$	λ_1	λ_2	λ_3
Ti-40Ni-10Cu	$\frac{1}{\sqrt{2}}\begin{pmatrix} 1 & -1 & 0 \\ 1 & 1 & 0 \\ 0 & 0 & \sqrt{2} \end{pmatrix}$	$\frac{1}{\sqrt{6}}\begin{pmatrix} \sqrt{3} & -\sqrt{3} & 0 \\ \sqrt{2} & \sqrt{2} & \sqrt{2} \\ -1 & -1 & 2 \end{pmatrix}$	$\begin{pmatrix} \frac{-1}{\sqrt{2}} \\ 0 \\ \frac{1}{\sqrt{2}} \end{pmatrix}$	$\begin{pmatrix} \frac{1}{\sqrt{2}} \\ \frac{1}{\sqrt{2}} \\ 0 \end{pmatrix}$	$\begin{pmatrix} 1 \\ 0 \\ 0 \end{pmatrix}$	0.5	0.5	0.5
Cu-14Al-4Ni	$\frac{1}{\sqrt{2}}\begin{pmatrix} 1 & -1 & 0 \\ 0 & 0 & \sqrt{2} \\ -1 & -1 & 0 \end{pmatrix}$	$\frac{1}{\sqrt{6}}\begin{pmatrix} \sqrt{3} & -\sqrt{3} & 0 \\ 1 & 1 & 2 \\ -\sqrt{2} & -\sqrt{2} & \sqrt{2} \end{pmatrix}$	$\begin{pmatrix} 0 \\ 0 \\ 1 \end{pmatrix}$	$\begin{pmatrix} \frac{1}{\sqrt{2}} \\ \frac{1}{\sqrt{2}} \\ 0 \end{pmatrix}$	$\begin{pmatrix} 1 \\ 0 \\ 0 \end{pmatrix}$	0.5	0.5	0.5

Table 3.1: Orientation, normals and volume fraction of the rank-two laminates used in the calculation for Ti-40Ni-10Cu (B19) and γ_1' Cu-14Al-4Ni (wt.%).

Orthorhombic Martensite

We consider two examples of materials undergoing cubic-orthorhombic transformation: Ti-40Ni-10Cu (B19) and γ_1' Cu-14Al-4Ni (wt.%). We assume $\mathbf{R}_1 = \mathbf{R}_3 = R_1$ and $\mathbf{R}_2 = \mathbf{R}_4 = R_2$. The texture, normals and volume fraction of the rank-two laminate are listed in Table 3.1 and the tensile loading direction for both cases is $\xi = (\cos(\theta), 0, \sin(\theta))^T$ for various θ. In fact, we will find later that this is exactly like the rolled sheet subjected to tensile loading along the rolling plane (see Section 3.3.1 and Figure 3.10). Figure 3.8 shows the inner bound, the outer bound and the exact value of the maximum recoverable strain calculated according to (3.14), (3.15) and (3.28), respectively. We have repeated the same calculations for different laminates, i.e., for different normals of $\mathbf{n}_1, \mathbf{n}_2$ and $\mathbf{n}_3$. The results are either the same or closer to the inner bound except in very few exceptional situations. We have also performed the calculations for a rank-three laminate. The results are even closer to the inner bound. It is clear that the constraints between the grains is overwhelming and hence $\epsilon_R \cong \epsilon_R^i$. Finally, the drawback of the outer bound can also be seen especially in the case of γ_1' Cu-14Al-4Ni (wt.%) at the loading direction $\theta = 0°$.

To understand the effect of the intergranular constraint, we show in Figure 3.9 the volume fractions of the different orthorhombic variants calculated according to the exact solution as well as the inner and outer bounds in the grains with orientation R_2 for the case $\theta = 60°$. Variant 6 is the most favorable variant in both Ti-Ni-Cu and Cu-Al-Ni for this orientation and hence the outer bound uses 100% variant 6. However, compatibility forces variants 1, 3, 4 and 5 to also form in Ti-Ni-Cu and variants 1 and 3 to also form in Cu-Al-Ni in the exact solution. The inner bound

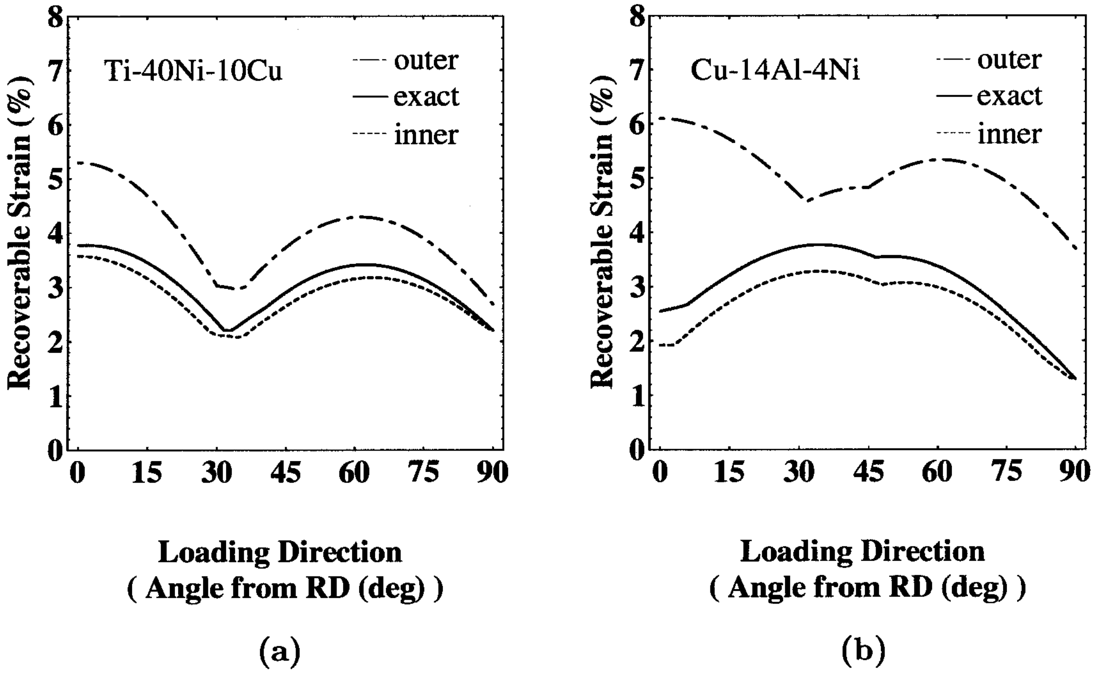

Figure 3.8: Maximum recoverable strain for the rank-two laminates subjected to uniaxial tension in different directions. (a) Ti-40Ni-10Cu (B19) (b) γ_1' Cu-14Al-4Ni (wt.%).

which respects compatibility does not get the volume fractions exactly correct, but is close.

In conclusion, these examples demonstrate that the inner bound is a reasonable estimate of the maximum recoverable strain while the outer bound is a poor estimate. This is consistent with the results of Bhattacharya and Kohn [12] and Kohn and Niethammer [48] who provide rigorous results in dimensionally reduced problems.

3.2.3 Combined Tension-Torsion

Consider a shape-memory wire or a circular tube below the transformation temperature in the self-accommodated state. Pull it uniaxially to the given strain ϵ_0 and apply a torque $\mathbf{M}$ to the ends. We wish to find w_R, the maximum recoverable twist - angle per unit length. Notice that w_R is not dimensionless; it depends on the outer radius r_0 of the specimen. However, $r_0 w_R$ is dimensionless and is independent of the dimensions of the specimen. Therefore, we estimate the maximum recoverable

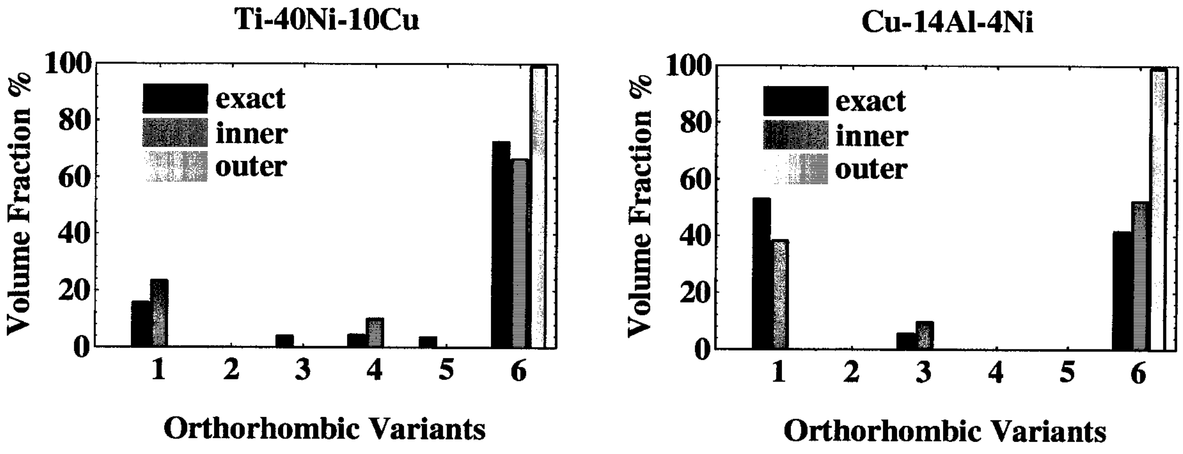

(a) (b)

Figure 3.9: Constraints from neighboring grains can suppress the most favorably oriented variant. Volume fractions of the different orthorhombic variants in the grains with orientation R_2 for the case $\theta = 60°$. (a) Ti-40Ni-10Cu (B19) (b) γ_1' Cu-14Al-4Ni (wt.%).

normalized twist $\gamma_R = r_0 w_R$. It will be clear that the normalized twist γ_R is also the shear strain in the outer-most part of the cross section.

Torsion is a very difficult problem in general anisotropic bodies. Therefore, we assume that the grains are very small and the specimen is macroscopically uniaxial in symmetry. Further, we assume that the applied traction on the boundary has the form $\mathbf{t} = (\tau(r)\mathbf{T}^t + \mathbf{T}^u)\mathbf{n}$ where $\mathbf{T}^t = \frac{1}{2}(\mathbf{i}_3 \otimes \mathbf{i}_\theta + \mathbf{i}_\theta \otimes \mathbf{i}_3)$, $\mathbf{T}^u = \sigma(\mathbf{i}_3 \otimes \mathbf{i}_3)$, and $\mathbf{n}$ is the outward normal. Here, $\{\mathbf{i}_r, \mathbf{i}_\theta, \mathbf{i}_3\}$ is the cylindrical basis with $\mathbf{i}_3$ parallel to the axis of the specimen. Clearly, the applied torque $M = \frac{1}{2}\int_{\partial\Omega_c} \tau(r) r dS$ where $\partial\Omega_c$ is the circular or annular cross section of the specimen. In this situation, it is reasonable to assume that the state of stress $\mathbf{T} = \tau(r)\mathbf{T}^t + \mathbf{T}^u$ throughout the specimen and the strain field has the form

$$\mathbf{e} = \begin{pmatrix} e_{11} & e_{12} & -\gamma\frac{x_2}{r_0} \\ e_{12} & e_{22} & \gamma\frac{x_1}{r_0} \\ -\gamma\frac{x_2}{r_0} & \gamma\frac{x_1}{r_0} & \epsilon_0 \end{pmatrix} \tag{3.31}$$

where e_{11}, e_{12}, e_{22} and γ are fixed constants, and ϵ_0 is the prescribed axial strain. The solution is then obtained by solving the following constrained minimization problem:

$$\min \int_{\Omega} \left(\bar{\varphi}(\mathbf{e}[\mathbf{u}]) - \tau(r)\, \mathbf{e}[\mathbf{u}] \cdot \mathbf{T}^t\right) d\mathbf{x} \tag{3.32}$$

over all $\mathbf{e}$ of the form (3.31) and all $\tau(r) \geq 0$ that satisfy $\frac{1}{2}\int_{\partial\Omega_c} \tau(r) r dS = M$. Let $\mathbf{e}_M$ and $\tau_M(r)$ minimize (3.32). Then, following an argument similar to that in the case of uniaxial loading, we obtain the maximum recoverable normalized twist as

$$\gamma_R = \lim_{M \to 0} (\mathbf{e}_M \cdot \mathbf{T}^t)\, |_{r=r_0} = \max_{\substack{e \in \mathcal{P} \\ \mathbf{e} \text{ as in } (3.31)}} (\mathbf{e} \cdot \mathbf{T}^t)\, |_{r=r_0} \tag{3.33}$$

Equation (3.33) can not be solved without knowing the set $\mathcal{P}$. However, we can bound it by replacing $\mathcal{P}$ with $\mathcal{P}_i$ and $\mathcal{P}_o$ to get the inner and outer bound, respectively. In particular, in the case of materials undergoing cubic-monoclinic transformation,

$$\gamma^i_R = \max_{\substack{\mathbf{e} \text{ as in } (3.31) \\ \mathbf{R}_j^T \mathbf{e} \mathbf{R}_j \in \mathcal{S}_{\text{orth}}\ \forall j=1,\cdots,N}} (\mathbf{e} \cdot \mathbf{T}^t)\, |_{r=r_0} \tag{3.34}$$

$$\gamma^e_R = \max_{\substack{\mathbf{e} \text{ as in } (3.31) \\ \mathbf{R}_j^T \mathbf{e} \mathbf{R}_j \in \mathcal{S}^c_{\text{mono}}\ \forall j=1,\cdots,N}} (\mathbf{e} \cdot \mathbf{T}^t)\, |_{r=r_0} \tag{3.35}$$

$$\gamma^o_R = \sum_{j=1}^{N} \max_{\substack{\mathbf{e}_j \text{ as in } (3.31) \\ \mathbf{R}_j^T \mathbf{e}_j \mathbf{R}_j \in \mathcal{S}^c_{\text{mono}}}} \left(\lambda_j \left(\mathbf{e}_j \cdot \mathbf{T}^t\right)\right) |_{r=r_0} \tag{3.36}$$

are the inner bound, inner estimate and outer bound, respectively.

We now explicitly evaluate the inner bound γ^i_R and estimate γ^e_R of the maximum recoverable normalized twist using (3.34) and (3.35) for Monoclinic-I wires or circular tubes with random texture.

Consider (3.34) first. In the case of random polycrystals, (3.34) can be rewritten as

$$\gamma^i_R = \max_{\substack{\mathbf{e} \text{ as in } (3.31) \\ \mathbf{R}^T \mathbf{e} \mathbf{R} \in \mathcal{S}_{\text{orth}}\ \forall \mathbf{R} \in SO(3)}} (\mathbf{e} \cdot \mathbf{T}^t)\, |_{r=r_0}\, . \tag{3.37}$$

Without loss of generality, we may take $e_{12} = 0$ simply by rotating the x_1 and x_2 axis with respect to the wire axis. Notice that $e_{11} + e_{22} = (2\alpha + \beta) - \epsilon_0$ and therefore $e_{11} + e_{22}$ is a fixed constant for a given applied extension ϵ_0. Therefore, the constraint in (3.37) can then be rewritten as

$$\mathbf{R}^T \begin{pmatrix} \chi & 0 & -\gamma\frac{x_2}{r_0} \\ 0 & \chi & \gamma\frac{x_1}{r_0} \\ -\gamma\frac{x_2}{r_0} & \gamma\frac{x_1}{r_0} & \epsilon_0 \end{pmatrix} \mathbf{R} + \frac{(e_{11} - e_{22})}{2} \mathbf{R}^T \begin{pmatrix} 1 & 0 & 0 \\ 0 & -1 & 0 \\ 0 & 0 & 0 \end{pmatrix} \mathbf{R} \in \mathcal{S}_{\text{orth}} \quad (3.38)$$

$\forall \mathbf{R} \in \mathrm{SO}(3)$ where $\chi = \frac{1}{2}(2\alpha + \beta - \epsilon_0)$. Using (3.38), we can show that the maximum in (3.37) is achieved when $e_{11} = e_{22} = \chi$. Then, the eigenvalues λ_1, λ_2 and λ_3 of $\mathbf{e}$ are

$$\begin{aligned} \lambda_1 &= \frac{1}{2}(\chi + \epsilon_0 - \sqrt{(\chi - \epsilon_0)^2 + 4\bar{\gamma}^2}\,) \\ \lambda_2 &= \chi \\ \lambda_3 &= \frac{1}{2}(\chi + \epsilon_0 + \sqrt{(\chi - \epsilon_0)^2 + 4\bar{\gamma}^2}\,) \end{aligned} \quad (3.39)$$

where $\bar{\gamma} = \gamma\frac{r}{r_0}$, $r = \sqrt{x_1^2 + x_2^2} \le r_0$.

Now the constraint $\mathbf{R}^T\mathbf{e}\mathbf{R} \in \mathcal{S}_{\text{orth}}$ $\forall \mathbf{R} \in \mathrm{SO}(3)$ is equivalent to

$$\begin{aligned} \beta \le \lambda_1, \lambda_2, \lambda_3 &\le \alpha, \\ \left|\frac{\lambda_i - \lambda_j}{2}\right| &\le (\frac{\alpha - \lambda_k}{\alpha - \beta})\delta \quad \text{for each \{ijk\}=perm\{123\}} \end{aligned} \quad (3.40)$$

according to [11]. Combining (3.39) and (3.40), we obtain the relation between γ_R^i and ϵ_0

$$\gamma_R^i = \begin{cases} \frac{1}{4}\sqrt{p^2(\bar{\epsilon}_0 + \frac{2(\alpha-\beta)}{3})^2 - 9\,\bar{\epsilon}_0^2} & \text{if } p = \frac{2\delta}{\alpha-\beta} \le 1 \\ \frac{1}{4}\sqrt{\frac{1}{9(p+1)^2}(9\bar{\epsilon}_0 - 3p\bar{\epsilon}_0 + 4p(\alpha - \beta))^2 - 9\,\bar{\epsilon}_0^2} & \text{if } p = \frac{2\delta}{\alpha-\beta} > 1 \end{cases} \quad (3.41)$$

where $\bar{\epsilon}_0 = \epsilon_0 - \frac{1}{3}(2\alpha + \beta)$. The result for Ti-Ni wire or tube is shown in Figure 3.15(a).

Similarly, the constraint $\mathbf{R}^T\mathbf{e}\mathbf{R} \in \mathcal{S}^c_{\text{mono}}\ \forall \mathbf{R} \in SO(3)$ is equivalent to

$$\begin{aligned} \beta \leq \lambda_1, \lambda_2, \lambda_3 &\leq \alpha, \\ \left|\frac{\lambda_i - \lambda_j}{2}\right| &\leq (\frac{\alpha - \lambda_k}{\alpha - \beta})\delta + (\frac{\lambda_k - \beta}{\alpha - \beta})\epsilon \quad \text{for each } \{\text{ijk}\}=\text{perm}\{123\}. \end{aligned} \tag{3.42}$$

Using (3.39) and (3.42), one can find out the relation between γ^e_R and ϵ_0 explicitly. The result for Ti-Ni wire or tube is also shown in Figure 3.15(a). We can similarly evaluate γ^i_R and γ^e_R explicitly for Monoclinic-II wires or tubes with random texture.

3.3 Results for Uniaxial Loading

We now evaluate the theoretical bounds on recoverable strains under uniaxial loading for specific textures. We shall use experimentally observed textures for comparison, and idealized textures for prediction. We focus on Ti-Ni and Cu-Zn-Al alloys. The results for other Cu-based SMAs are very similar to those of Cu-Zn-Al.

3.3.1 Rolling Texture: Comparison with Experimental Observations

Zhao and Beyer [100, 101] have recently measured the texture and recoverable strain in rolled Ti-Ni-Cu sheets. After rolling, the specimens were heat-treated at a temperature below the recrystallization temperature of this alloy. The Cu composition was around 5% so that the martensite phase was monoclinic similar to Ti-Ni [69, 88]. The observed texture is shown in Figure 3.10: 60% of the grains had a $\{110\}\langle 110\rangle$ orientation in the parent phase while 40% of the grains had a $\{111\}\langle 110\rangle$ orientation. Here, $\{hkl\}\langle uvw\rangle$ means $\{hkl\}$ planes lie parallel to the rolling plane and $\langle uvw\rangle$ directions lie parallel to the rolling direction (RD). ND and TD denote the normal and transverse directions of the rolled sheet. Specimens were cut along different loading directions (LDs) along the plane of the sheet and the recoverable strains were measured by the thermal cycling tensile test. The experimental results are shown as dark

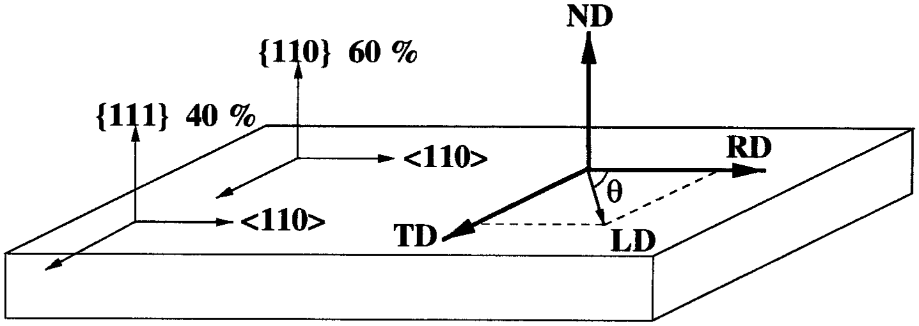

Figure 3.10: Directions in a rolled sheet and texture observed by Zhao and Beyer.

circles • in Figure 3.11.

Theoretical bounds computed using (3.19), (3.20) and (3.21) are shown in Figure 3.11(a). Here, the upper dashed line (OB) is the outer bound ϵ^o_R, the dashed line in the middle (IE) is the inner estimate ϵ^e_R, and the thin continuous line (IB) is the inner bound ϵ^i_R. As expected, the experimental observations of recoverable strains lie close to the inner estimate and inner bound while the outer bound is a serious over-estimate.

However, the experimental result near the RD violates the inner bound. There are a variety of reasons. Among them is the fact that the texture is not ideal; not all grains have the $\{111\}\langle 110\rangle$ or $\{110\}\langle 110\rangle$ orientation, but contains certain "wobble" about the ideal orientation. Therefore, we take 100 grains with the following orientation: 40 grains are oriented randomly within 5° of $\{111\}\langle 110\rangle$ while 60 grains are oriented randomly within 5° of $\{110\}\langle 110\rangle$. We call this a texture with 5° wobble. The results are shown in Figure 3.11(b). We have also repeated the calculation using 200 grains with the same distribution and find the results are essentially identical. However, if the wobble is taken as 10° instead of 5° [43, 19], the inner estimate (IE) and inner bound (IB) drop about 1% in the vicinity of RD and remain unchanged near the TD.

We also compare our results with similar experiments of Inoue *et al.* [43]. First consider their PL-CR specimens which have a strong $\{111\}$ fiber || ND. This means the rolling planes are $\{111\}$ in the parent phase while the RD is random. Our bounds calculated with 5° wobble and their experimental observations are shown

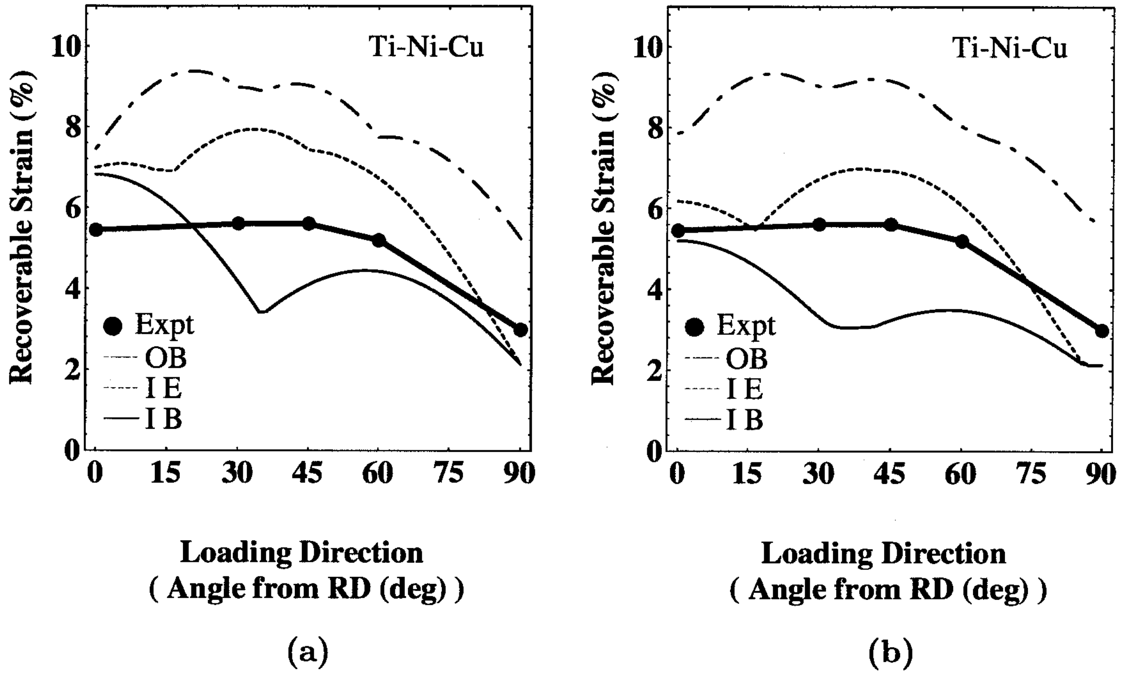

Figure 3.11: Comparison of theory and experiment for the Zhao-Beyer texture. Here, • Expt is the measured recoverable strain. OB, IE and IB mean outer bound ϵ^o_R, inner estimate ϵ^e_R, and inner bound ϵ^i_R, respectively. (a) ideal texture (b) texture with 5° wobble.

in Figure 3.12(a). As expected, the results are almost isotropic in the plane and the experimental results are close to the inner bound and the inner estimate. Next, consider their PL-RX specimens which contains $\langle 110 \rangle$ partial fiber || RD with peaks at $\{332\}\langle 110 \rangle$ and $\{111\}\langle 110 \rangle$ accompanied with a spread towards $\{110\}\langle 110 \rangle$. This texture is similar to that observed by Zhao and Beyer [100, 101] except that the distribution of the rolling planes is different. Our bounds calculated with 5° wobble are compared with their experimental observations in Figure 3.12(b).

The inner bounds and estimates, which we emphasize do not use any adjustable parameters, are in general agreement with the observed recoverable strains: they pick out the level and the trend. However, they do differ in one crucial aspect. In particular, notice in Figure 3.11 and Figure 3.12 (b) that the inner bound contains a cusp-like dip around 35 degrees. The main reason, we believe, is the fact that for a monoclinic material we use the set $\mathcal{S}_{\text{orth}}$ instead of $\mathcal{S}_{\text{mono}}$ to calculate the inner bound. The difference between these sets is significant in some isolated directions; and one

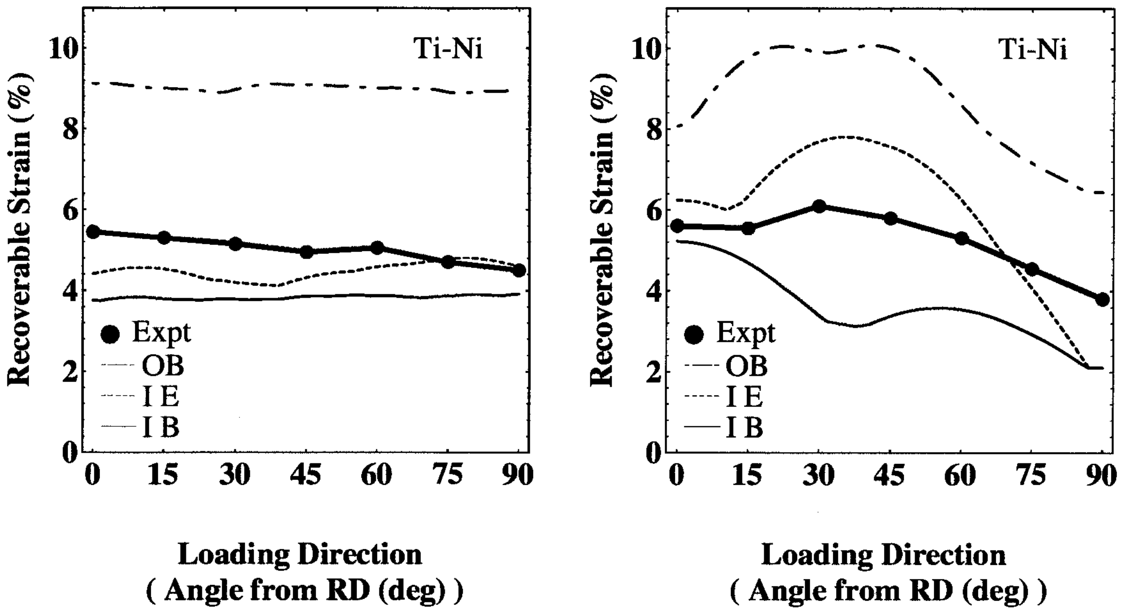

(a) (b)

Figure 3.12: Comparison of theory and experiment for the Inoue-Miwa-Inakazu textures. Here, • Expt is the measured recoverable strain. OB, IE and IB mean outer bound ϵ^o_R, inner estimate ϵ^e_R, and inner bound ϵ^i_R, respectively. (a) PL-CR specimens with $\{111\}\langle uvw\rangle$ texture (b) PL-RX specimens with $\langle 110\rangle$ partial fiber with components from $\{111\}\langle 110\rangle$ to $\{110\}\langle 110\rangle$.

such direction corresponds to the cusp-like dip for these textures. This is indeed a weakness of our inner bound which uses $\mathcal{S}_{\text{orth}}$, and calculation of the set $\mathcal{S}_{\text{mono}}$ still remains a major outstanding problem. It is to overcome this weakness that we also include the inner estimate. A significant difference between the inner bound and estimate in some loading direction provides a warning that the inner bound may be too conservative in this direction.[2] A second reason for the deviation is the fact that we use only the major fiber (with wobble) rather than the exact measured texture.

3.3.2 Rolling Texture: Prediction

Most SMAs have a body-centered-cubic (BCC) superlattice structure in the austenite phase [63]. This is certainly true for Ti-Ni and Cu-based SMAs. Common BCC textures are listed in Table 3.2 [85, 97, 30, 58]. We note that α-fiber II is not common

---

[2] At the same time, close agreement between the inner bound and estimate (as shown in Figure 3.12 (a)) indicates that these are reliable predictions.

Fiber	Fiber Axis	Relevant Components Associated with the Fiber
α-fiber I	$\langle 110 \rangle \parallel$ RD	$\{001\}\langle 110 \rangle - \{112\}\langle 110 \rangle - \{111\}\langle 110 \rangle$
α-fiber II	$\langle 110 \rangle \parallel$ RD	$\{111\}\langle 110 \rangle - \{110\}\langle 110 \rangle$
γ-fiber	$\{111\} \parallel$ ND	$\{111\}\langle 110 \rangle - \{111\}\langle 112 \rangle$
η-fiber	$\langle 100 \rangle \parallel$ RD	$\{001\}\langle 100 \rangle - \{011\}\langle 100 \rangle$

Table 3.2: Some common texture fibers observed in BCC metals and alloys. The α-fiber II is the characteristic texture of Ti-Ni with the B2-lattice.

in general BCC textures, but is observed in SMAs [43, 101].

Figure 3.13 and Figure 3.14 show the inner bound and estimate for Ti-Ni and Cu-Zn-Al for the different textures listed in Table 3.2. Comparing these, it is clear that the recoverable strains are much higher in Ti-Ni than in Cu-Zn-Al for typical BCC textures. The α-fiber I in Ti-Ni exhibits two peaks in RD and TD of the rolled sheet as shown in Figure 3.13(a). Therefore, this texture is desirable for uniaxial applications since it is easy to extract good specimens from a rolled sheet. On the other hand, the γ-fiber observed in [43] exhibits the least anisotropy as seen in Figure 3.13(c). This texture is preferred if the recoverable strain is required in every direction of the rolled sheet. In Cu-based SMAs, the shape-recovery strain while poor in general is expected to be relatively large for the η-fiber. Unfortunately, this fiber is usually less common. We also note that the behavior of α-fiber I can be improved by restricting the fiber components from $\{001\}\langle 110 \rangle$ to $\{112\}\langle 110 \rangle$: the result is similar to that of Figure 3.14(a) except the peak of the inner estimate rises to about 5% around 45°. Park and Bunge [79, 80, 81] have observed this texture in a hot-rolled Cu-Zn-Al sheet although no recoverable strain measurements are available.

3.3.3 Other Textures

Random Texture

The inner bound and inner estimate on the maximum recoverable extension for a polycrystal with randomly oriented grains are shown in Table 3.3 for Ti-Ni and Cu-Zn-Al. The behavior of these alloys is quite similar, and rather poor with random texture.

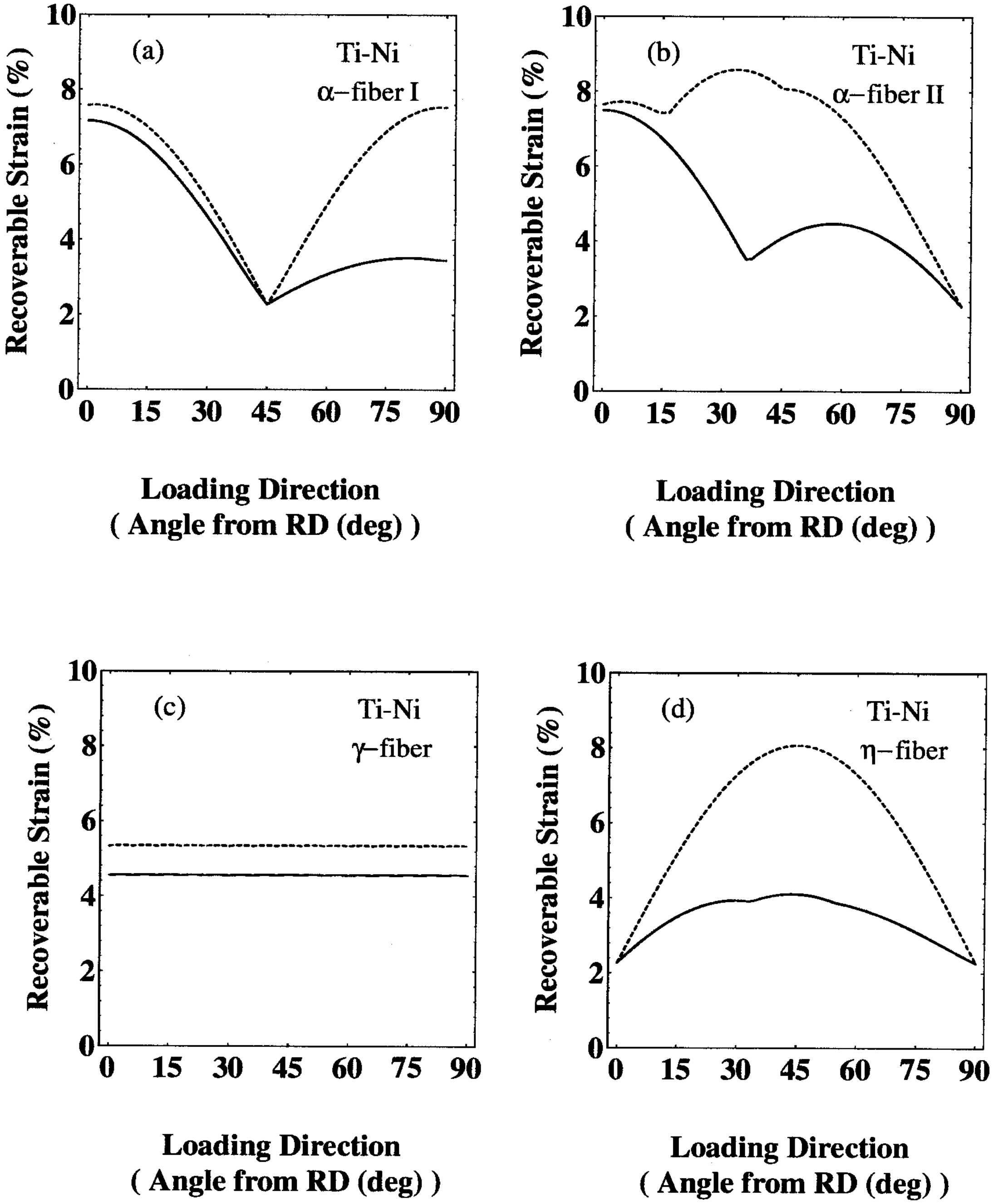

Figure 3.13: The predicted uniaxial recoverable extension in Ti-Ni for various rolling textures. The upper dashed line is the inner estimate ϵ_R^e while the lower continuous line is the inner bound ϵ_R^i.

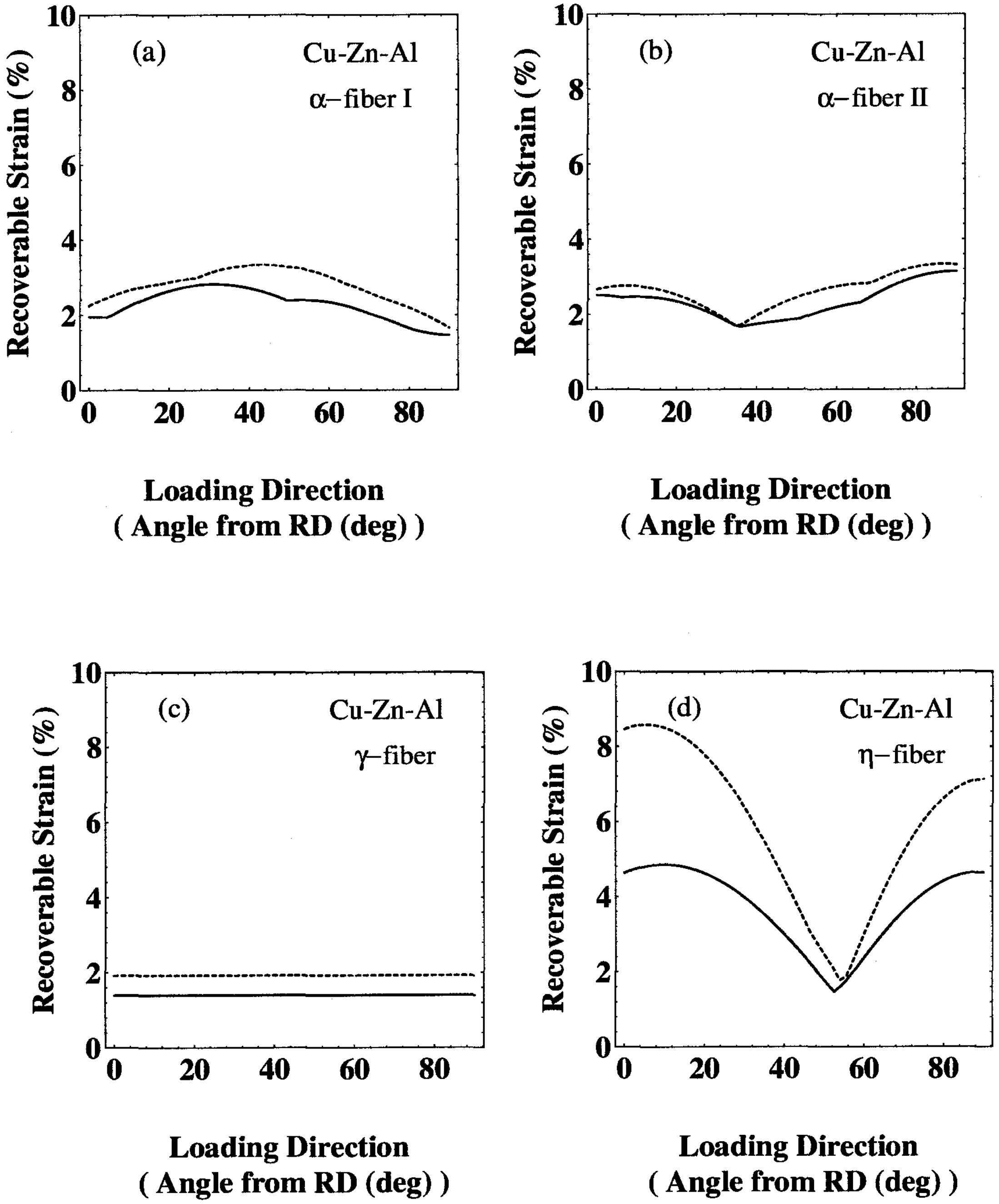

Figure 3.14: The predicted uniaxial recoverable extension in Cu-Zn-Al for various rolling textures. The upper dashed line is the inner estimate ϵ_R^e while the lower continuous line is the inner bound ϵ_R^i.

Texture	Recoverable Strains (%)			
	Ti-Ni		Cu-Zn-Al	
	ϵ_R^i	ϵ_R^e	ϵ_R^i	ϵ_R^e
random	2.3	2.3	1.3	1.7
⟨110⟩ wire/rod	6.0	7.5	1.3	1.7
⟨111⟩ wire/rod	3.9	9.6	1.7	1.7
{100} ribbon	2.3	2.3	4.6	7.1

Table 3.3: The predicted uniaxial recoverable extension for various textures in bulk polycrystals.

Wire Drawing Texture

BCC metals and alloys have been shown to develop strong ⟨110⟩ fiber texture after drawing or extrusion [41]. Assuming equal volume fraction in all of the fiber components, the inner bound and estimate of tensile recoverable strain in Ti-Ni and Cu-Zn-Al are listed in Table 3.3. Clearly, Ti-Ni is expected to have much better shape-memory behavior than Cu-Zn-Al for this fiber. Park *et al.* [82] have observed a strong ⟨110⟩ fiber texture in the parent phase in cold drawn Cu-Zn-Al wires although no recoverable strain measurements are available.

Yamauchi *et al.* [99] observed a ⟨111⟩ recrystallization fiber texture in cold-drawn and subsequently annealed Ti-Ni rods. Similar observation was reported in [98] for Ti-Ni-Cu wire. Our bounds for this ⟨111⟩ texture is also listed in Table 3.3. Again, this texture is more favorable in Ti-Ni than in Cu-Zn-Al.

Finally, Miyazaki *et al.* [64] have reported that drawn wires of Ti-50.6Ni alloy can recover around 6% tensile strain although there is no additional information to show those wires have such ⟨110⟩ or ⟨111⟩ fiber texture.

Solidification Texture

Eucken *et al.* [34, 35, 33] have obtained a columnar grain structure with a strong {100} texture in meltspun ribbons of both Ti-Ni alloy and Cu-based SMAs. Their experimental results show that Ti-Ni ribbon can recover less than 4% tensile strain, but Cu-Al-Ni ribbon can recover as large as 6.5% strain. Indeed, this difference can be predicted using the inner bound [11]. One can prove the exact inner bound is

$(\alpha - \frac{2\alpha+\beta}{3})$ in Monoclinic-I martensites. On the other hand, Monoclinic-II martensites can recover $((\alpha+\delta) - \frac{2\alpha+\beta}{3})$ tensile strain if $\epsilon \geq \delta$ or $((\alpha+\epsilon) - \frac{2\alpha+\beta}{3})$ tensile strain if $\epsilon \leq \delta$. As a result, the exact inner bounds on recoverable extension are 2.3% and 5.8% for Ti-Ni and Cu-Al-Ni, respectively. Clearly, $\{100\}$ texture favors larger recoverable strain in Cu-based SMAs than in Ti-Ni alloys.

3.4 Results for Combined Tension-Torsion

We now report the results for combined tension-torsion: first pull the self-accommodated wire (or circular tube) specimen to the desired strain ϵ_0 below the transformation temperature, and measure the twist angle using the thermal cycling test under the constant torque. Figure 3.15 shows the results for a random polycrystal and for a wire or tube with $\langle 110 \rangle$ or $\langle 100 \rangle$ textures. The calculation for $\langle 110 \rangle$ and $\langle 100 \rangle$ textures is similar to that for random texture at the end of Section 3.2.3. Notice that the maximum recoverable normalized twists are relatively small. Further, the recoverable twist decreases with increasing imposed recoverable extension in random and $\langle 110 \rangle$ texture while $\langle 100 \rangle$ texture shows the opposite behavior. Sittner *et al.* [94] have used force control to study stress-induced pseudoelasticity in Cu-Zn-Al-Mn under the combined tension-torsion. The maximum recoverable normalized twist is around 1% in their experiment, and it increases with applied tensile loading. Unfortunately, they do not provide any information about the texture.

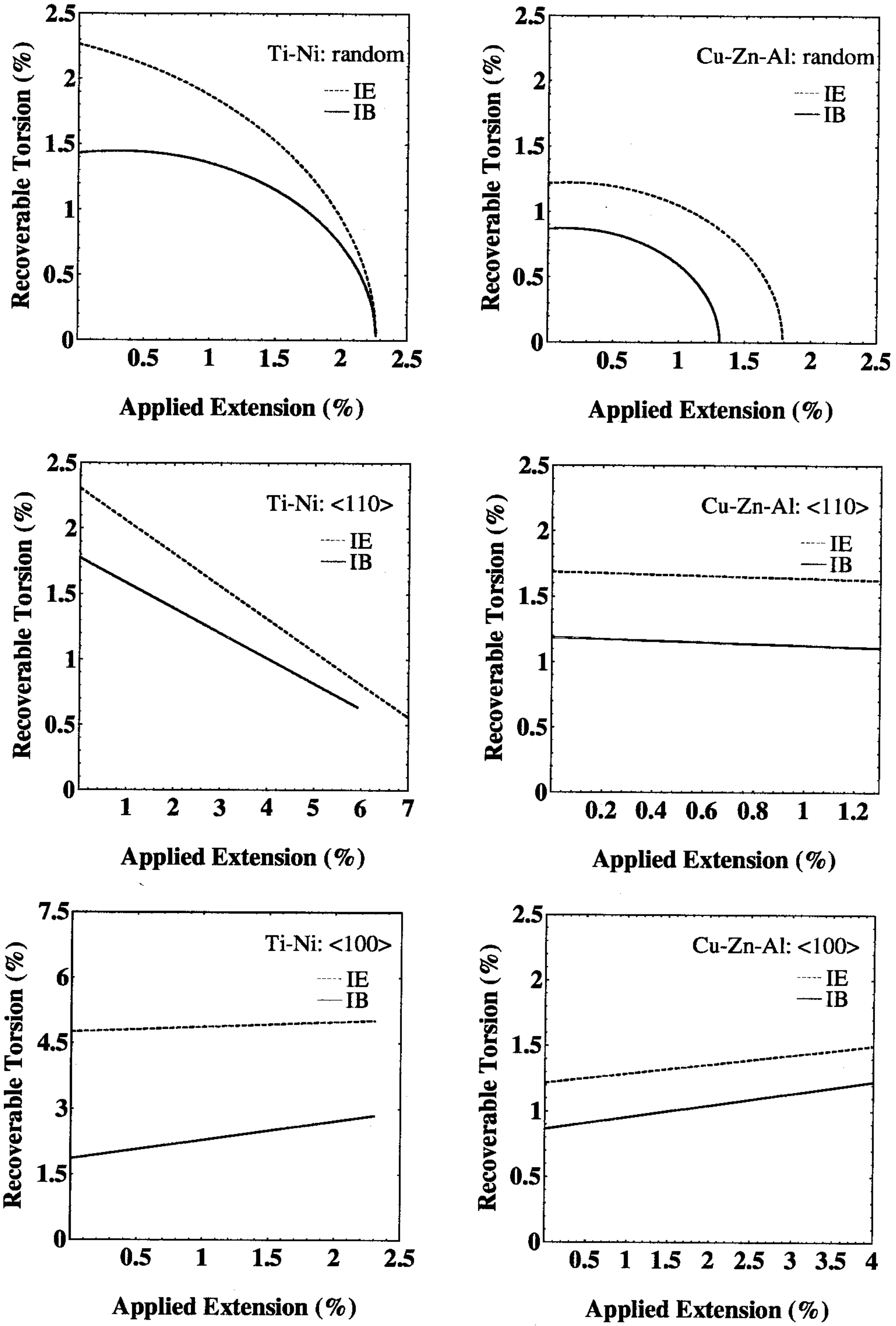

Figure 3.15: The predicted recoverable torsion (normalized twist) for different applied extension in Ti-Ni and Cu-Zn-Al polycrystals with random texture, ⟨110⟩ and ⟨100⟩ fiber textures, respectively. Notice that torsion (normalized twist) means outer radius times angle of twist. Here, IE and IB mean inner estimate γ_R^e and inner bound γ_R^i.

Chapter 4 Shape-Memory Effect in Thin Films

4.1 Effective Energy of a Thin Film

Our first task is to develop a framework analogous to that described in Section 3.1 to discuss the effective behavior of heterogeneous thin films as shown in Figure 1.2. Let the film occupy a reference domain

$$\Omega^h = \{\mathbf{x} \in I\!R^3 : (x_1, x_2) \in S, 0 < x_3 < h\} \tag{4.1}$$

where S is a bounded Lipschitz domain, $\{x_1, x_2, x_3\}$ are relative to an orthonormal film basis $\{\mathbf{e_1}, \mathbf{e_2}, \mathbf{e_3}\}$, and h is the film thickness. Let $\tilde{\mathbf{y}} : \Omega^h \to I\!R^3$ be the deformation of the film. The total energy of the heterogeneous thin film is

$$\tilde{e}^{(h)}[\tilde{\mathbf{y}}] = \int_{\Omega^h} \left\{ \kappa^2 |\nabla^2 \tilde{\mathbf{y}}|^2 + \varphi(\nabla \tilde{\mathbf{y}}, \frac{x_1}{d}, \frac{x_2}{d}, \frac{x_3}{h}) \right\} d\mathbf{x} \tag{4.2}$$

where $\varphi : I\!M^{3\times3} \times I\!R^2 \times (0,1) \to I\!R$ is the elastic free energy density of the film. We assume that $\varphi(\cdot, \xi_1, \xi_2, \cdot)$ is periodic in the in-plane variables ξ_1 and ξ_2 with period $Z = [0,1]^2$. So d scales like the typical grain size. Further, since we wish to model martensites, $\varphi(\mathbf{F}, \cdot, \cdot, \cdot)$ may have a multi-well structure and consequently nonconvex. Note that we have included the interfacial energy of the type $\kappa^2 |\nabla^2 \tilde{\mathbf{y}}|^2$. Minimizers of the energy (4.2) have oscillations on a length scale that scale with κ and hence we call κ the length-scale of the microstructure. We are interested in finding the limiting behavior of the film when all length scales κ, d and h tend to zero. Therefore, we take

$$\kappa = \kappa(h) > 0, \quad d = d(h) > 0, \quad \lim_{h\to0} \kappa(h) = 0, \quad \lim_{h\to0} d(h) = 0, \tag{4.3}$$

and assume that they have fixed limiting ratios:

$$\alpha = \lim_{h \to 0} \frac{\kappa}{d}, \quad \beta = \lim_{h \to 0} \frac{h}{d}, \quad \alpha' = \lim_{h \to 0} \frac{\kappa}{h}. \tag{4.4}$$

In bulk materials, the homogenization of cellular elastic materials with nonconvex energy density φ has been studied by Braides [15] and Müller [67]. The same problem including the interfacial energy has been studied by Francfort and Müller [37]. However, microstructure can be significantly different in thin films as compared to bulk materials, endowing materials with dramatically distinct properties (for example, see [3]). Recently, Bhattacharya and James [10] have developed a theory of single crystal martensitic thin films which captures this effect. Related work on the modeling of thin structure with convex (quadratic) energy density includes, for example, Kohn and Vogelius [49, 50], Damlamian and Vogelius [26] and Caillerie [20]; and related problems with nonconvex energy density include, for example, Acerbi *et al.* [1], Le Dret and Raoult [29], Fonseca and Francfort [36]. We wish to combine homogenization with the thin-film analysis for nonconvex energies and apply it to heterogeneous martensitic films. Braides *et al.* [17] and Braides and Fonseca [14] have studied a similar problem with $\kappa = 0$.

Our approach is variational. We study the "variational limit" of (4.2) as h tends to zero. Since the energy defined in (4.2) will scale like h as h tends to zero, we shall be interested in the limiting energy per unit thickness; i.e.,

$$\tilde{e}_1^{(h)} = \frac{1}{h} \tilde{e}^{(h)}.$$

The equilibrium configuration for each finite thickness corresponds to the minimizer (minimizing sequences) of the functional $\tilde{e}_1^{(h)}$. We expect the minimum values and the minimizers of the functional $\tilde{e}_1^{(h)}$ to converge to those of the "limiting energy" $\tilde{e}_1^{(0)}$. In this context, the natural tool which captures such properties is Γ-convergence as proposed by De Giorgi [38] and De Giorgi and Franzoni [39]. The notion of Γ-convergence, under a suitable technical hypothesis, is nearly identical to that of

	h<<d	**h ~ d**	**h >>d**
κ >>d	**Theorem 1** **A T**	**Theorem 1** **A T**	**Theorem 1** **A T** $\kappa \overset{>>}{\underset{<<}{\sim}} \mathbf{h}$
κ ~ d	**Theorem 2** $\mathbf{T}^{\mathbf{A}}_{\mathbf{H}}$	**Theorem 3** **A** **H** **T**	$\overset{\mathbf{A}}{\mathbf{H}}{}^{\mathbf{T}}$ (?)
κ<<d	**Theorem 2** **T H** $\kappa \overset{>>}{\underset{<<}{\sim}} \mathbf{h}$ **Theorem 4**	**Theorem 3** **H** **T**	**H T**

Table 4.1: Summary of the effective behavior of a heterogeneous thin film. **A** means averaging, **H** means homogenizing and **T** means thin-film limit. "**TH**" denotes that the effective energy density $\bar{\varphi}$ is obtained by taking thin-film limit first, and then homogenizing in the plane of the film. On the other hand, "**HT**" denotes homogenization first followed by thin-film limit. Finally, a stacked symbol $\overset{\mathbf{H}}{\mathbf{T}}$ denotes performing these operations simultaneously.

convergence of minimizers (see also Remark 1). Using this notion, we show that the limiting energy is always given by

$$\tilde{e}_1^{(0)}[\mathbf{y}] = \int_S \bar{\varphi}\left(\frac{\partial \mathbf{y}}{\partial x_1}, \frac{\partial \mathbf{y}}{\partial x_2}\right) dx_1 dx_2$$

where $\bar{\varphi}$ is the effective energy density and only depends on the in-plane gradient of deformation $\mathbf{y}$ and not explicitly on the position.

In the following, we give a non-technical description of our main results which is summarized in Table 4.1. The most important finding is that the effective energy density $\bar{\varphi}$ crucially depends on the limiting ratios of these three length scales.

1. *Strong interfacial energy* ($\kappa >> d$). Assume $\varphi = \varphi(\mathbf{F}, \frac{x_1}{d}, \frac{x_2}{d})$. Our Theorem 1 shows that the effective energy density $\bar{\varphi}$ is obtained by averaging the microscopic energy φ over the period, then passing to the thin-film limit. It costs materials more energy to form microstructures within each grain as a result of strong interfacial energy. Material is internally stressed. The result is also true

if $\varphi = \varphi(\mathbf{F}, \frac{x_1}{d}, \frac{x_2}{d}, \frac{x_3}{h})$ and if $\kappa >> d$ and $\kappa >> h$.

2. *Flat grains* ($d >> h$). Assume $\varphi = \varphi(\mathbf{F}, \frac{x_1}{d}, \frac{x_2}{d})$. If the length scale of microstructure is much smaller than that of grains (i.e., if $\kappa << d$), then Theorem 2 shows that the elastic energy dominates the interfacial energy and materials can form microstructures freely. As a result, the macroscopic energy density $\bar{\varphi}$ is impervious to the presence of interfacial energy. Further, $\bar{\varphi}$ can be identified to be obtained by taking the thin-film limit and then homogenizing in the plane of the film. The thin-film limit says that only the in-plane compatibility is important and this allows a wider class of microstructure formed in thin films than in bulk materials. On the other hand, if the length scales of grains and microstructure are in the same order of magnitude (i.e., if $\kappa \approx d$), Theorem 2 shows that the interfacial energy explicitly contributes to the effective energy density $\bar{\varphi}$. Materials can form only a limited amount of microstructure because of competing energies between elastic energy and interfacial energy.

3. *Comparable grains* ($d \approx h$). Assume $\varphi = \varphi(\mathbf{F}, \frac{x_1}{d}, \frac{x_2}{d}, \frac{x_3}{h})$. Our Theorem 3 gives the expression of effective energy density $\bar{\varphi}$ when all length scales are comparable. This case apparently has no simple explanation since the averaging, homogenizing and thin-film limit are taken into account together.

4. *Long grains* ($d << h$). Assume $\varphi = \varphi(\mathbf{F}, \frac{x_1}{d}, \frac{x_2}{d})$. First if $d << \kappa, h$, our Theorem 1 includes this case. Next if $\kappa = 0$ and $d << h$, this case has been recently proved by Braides and Fonseca [14]. It says that the effective energy density is obtained by homogenizing the bulk material, then passing to the thin-film limit. We expect the result is also true even if the interfacial energy is included and if $\kappa << d$. Finally, if $\kappa \approx d << h$, we conjecture the effective energy density is obtained by taking averaging and bulk homogenization first, and then passing to the thin-film limit.

5. *Multilayers* (κ versus h). Assume $\varphi = \varphi(\mathbf{F}, \frac{x_3}{h})$. In such a situation, only two physical parameters κ and h are relevant. Our Theorem 4 gives the expression

of $\bar{\varphi}$ containing through-the-thickness variations.

4.2 Mathematical Preliminaries

It is often convenient to work on a fixed domain instead of a varying domain Ω^h, so we introduce the following change of variables:

$$\mathbf{z}_p = (z_1, z_2) = \mathbf{x}_p = (x_1, x_2), \quad z_3 = \frac{1}{h} x_3, \quad \mathbf{x} \in \Omega^h, \tag{4.5}$$

and set

$$\Omega^1 = S \times (0, 1). \tag{4.6}$$

To each deformation $\tilde{\mathbf{y}} : \Omega^h \to I\!R^3$ we associate a deformation $\mathbf{y} : \Omega^1 \to I\!R^3$ via

$$\mathbf{y}(\mathbf{z}(\mathbf{x})) = \tilde{\mathbf{y}}(\mathbf{x}), \quad \mathbf{x} \in \Omega^h.$$

We use the notation ∇_p for the gradient in the plane of the film; i.e.,

$$\nabla_p \mathbf{y} = \mathbf{y}_{,1} \otimes \mathbf{e}_1 + \mathbf{y}_{,2} \otimes \mathbf{e}_2,$$

and $\mathbf{y}_{,1} = \frac{\partial \mathbf{y}}{\partial z_1} = (\frac{\partial y_1}{\partial z_1}, \frac{\partial y_2}{\partial z_1}, \frac{\partial y_3}{\partial z_1})^T$; etc. We now change variables in $\frac{1}{h}\tilde{e}^{(h)}$ using (4.2), and (4.5) and get

$$\begin{aligned} \tilde{e}_1^{(h)}[\mathbf{y}] &:= \frac{1}{h}\tilde{e}^{(h)}[\tilde{\mathbf{y}}] \\ &= \int\limits_{\Omega^1} \left\{ \kappa^2 \left(|\nabla_p^2 \mathbf{y}|^2 + \frac{2}{h^2} |\nabla_p \mathbf{y}_{,3}|^2 + \frac{1}{h^4} |\mathbf{y}_{,33}|^2 \right) \right. \\ &\quad \left. + \; \varphi(\mathbf{y}_{,1} | \mathbf{y}_{,2} | \frac{1}{h} \mathbf{y}_{,3}, \frac{\mathbf{z}_p}{d}, z_3) \right\} d\mathbf{z}. \end{aligned} \tag{4.7}$$

We have used the notation

$$\mathbf{F} = (\mathbf{f}_1|\mathbf{f}_2|\mathbf{f}_3) = \mathbf{f}_1 \otimes \mathbf{e}_1 + \mathbf{f}_2 \otimes \mathbf{e}_2 + \mathbf{f}_3 \otimes \mathbf{e}_3$$

for $\mathbf{F} \in I\!M^{3\times 3}$.

We assume the energy density φ satisfies the following conditions:

1. $\varphi(\mathbf{F}, \mathbf{z})$ is Carathéodory and nonnegative.
2. Periodicity in the plane of the film: $\varphi(\mathbf{F}, \mathbf{z}_p, z_3)$ is periodic in the in-plane variable $\mathbf{z}_p = (z_1, z_2)$ with period $Z = [0,1]^2$ for all $\mathbf{F} \in I\!M^{3\times 3}$ and $z_3 \in (0,1)$.
3. Growth and coercivity conditions:

$$c_1(|\mathbf{F}|^p - 1) \leq \varphi(\mathbf{F}, \mathbf{z}) \leq c_2(|\mathbf{F}|^p + 1) \tag{4.8}$$

   for all $\mathbf{F} \in I\!M^{3\times 3}$ and for a.e. $\mathbf{z} = (\mathbf{z}_p, z_3) \in I\!R^2 \times (0,1)$.

4. Lipschitz condition:

$$|\varphi(\mathbf{F}, \mathbf{z}) - \varphi(\mathbf{G}, \mathbf{z})| \leq c_2(1 + |\mathbf{F}|^{p-1} + |\mathbf{G}|^{p-1})|\mathbf{F} - \mathbf{G}| \tag{4.9}$$

   for all $(\mathbf{F}, \mathbf{G}) \in I\!M^{3\times 3} \times I\!M^{3\times 3}$ and for a.e. $\mathbf{z} = (\mathbf{z}_p, z_3) \in I\!R^2 \times (0,1)$.

Notice that in (4.8) and (4.9), $0 < c_1 \leq c_2$ and p satisfies

$$1 < p < \infty.$$

We seek to minimize $\tilde{e}_1^{(h)}[\mathbf{y}]$ over the space V where

$$V = \{\mathbf{y} : \mathbf{y} \in W^{1,p}(\Omega^1, I\!R^3) \cap W^{2,2}(\Omega^1, I\!R^3)\}. \tag{4.10}$$

Therefore, we introduce

$$e_1^{(h)}[\mathbf{y}] = \begin{cases} \tilde{e}_1^{(h)}[\mathbf{y}] & \text{if} \quad \mathbf{y} \in V, \\ +\infty & \text{otherwise.} \end{cases} \tag{4.11}$$

So the new formulation of the variational problem is minimized over a fixed space. Clearly, the minimum values and minimizers of both formulations coincide if $\tilde{e}_1^{(h)}[\mathbf{y}] < \infty$.

Now our goal is to compute the Γ-limit of $e_1^{(h)}$ as h, d and κ tend to zero with fixed limiting ratios (4.4). To this purpose, we recall that

Definition 1 *A family* $e_1^{(h)}$ *of functionals on* $W^{1,p}(\Omega^1, I\!R^3)$ $(1 < p < \infty)$ *is said to* Γ*-converge (in the weak* $W^{1,p}(\Omega^1, I\!R^3)$*-topology) to* $e_1^{(0)}$ *if and only if*

(I) *every sequence* $\mathbf{y}^{(h)}$ *with*

$$\mathbf{y}^{(h)} \rightharpoonup \mathbf{y} \quad in \quad W^{1,p}(\Omega^1, I\!R^3) \quad as\ h \to 0, \tag{4.12}$$

satisfies the "lower bound"

$$\liminf_{h \to 0} e_1^{(h)}[\mathbf{y}^{(h)}] \geq e_1^{(0)}[\mathbf{y}]; \tag{4.13}$$

(II) *for every* $\mathbf{y} \in W^{1,p}(\Omega^1, I\!R^3)$*, there exists a sequence* $\mathbf{y}^{(h)}$ *called the "recovery sequence" such that*

$$\mathbf{y}^{(h)} \rightharpoonup \mathbf{y} \quad in \quad W^{1,p}(\Omega^1, I\!R^3) \quad as\ h \to 0 \tag{4.14}$$

and

$$\lim_{h \to 0} e_1^{(h)}[\mathbf{y}^{(h)}] = e_1^{(0)}[\mathbf{y}]. \tag{4.15}$$

Remark 1 The limiting functional $e_1^{(0)}$, by construction, is lower semicontinuous with respect to weak convergence in $W^{1,p}(\Omega^1, I\!R^3)$ [16] and, therefore, attains its minimum value due to the coercivity condition (4.8). Further, using the fact that the L^2-norm is sequentially lower semicontinuous and Rellich's compactness theorem, one can show that $e_1^{(h)}$ admits a minimum for any fixed $h > 0$ (cf. Francfort and Müller [37]). Therefore, minimizers of $e_1^{(h)}$ converges to those of $e_1^{(0)}$ by the fundamental theorem of Γ-convergence (see, for example, Braides and Defranceschi [16]). □

In the following, we will show that in all cases $e_1^{(h)}$ Γ-converges to a functional $e_1^{(0)}$ of the form

$$e_1^{(0)}[\mathbf{y}] = \begin{cases} \displaystyle\int_S \bar{\varphi}(\nabla_p \mathbf{y})\, d\mathbf{z}_p & \text{if} \quad \mathbf{y} \in V_S, \\ +\infty & \text{otherwise,} \end{cases} \tag{4.16}$$

where $\bar{\varphi}$ may be described as an effective energy density and V_S is defined by

$$V_S = \{\mathbf{y} : \mathbf{y} \in W^{1,p}(\Omega^1, I\!R^3) \ \text{ and } \ \mathbf{y}_{,3} = 0 \ \text{ for a.e. } \mathbf{z} \text{ in } \ \Omega^1\} \tag{4.17}$$

which is canonically isomorphic to $W^{1,p}(S, I\!R^3)$. The following lemma is the first step towards proving (4.16); with it we only need to compute the Γ-limit of $e_1^{(h)}$ for $\mathbf{y} \in V_S$.

Lemma 1 *If* $\mathbf{y} \notin V_S$, *then* $e_1^{(0)}[\mathbf{y}] = +\infty$.

Proof. Assume $\mathbf{y} \notin V_S$. It suffices to show that for any sequence $\mathbf{y}^{(h)} \in V$ such that $\mathbf{y}^{(h)} \rightharpoonup \mathbf{y}$ in $W^{1,p}(\Omega^1, I\!R^3)$ as $h \to 0$,

$$\liminf_{h \to 0} e_1^{(h)}[\mathbf{y}^{(h)}] = +\infty. \tag{4.18}$$

Suppose (4.18) were not true. It means that there exists a sequence $\mathbf{y}^{(h)}$ converges weakly to $\mathbf{y}$ in $W^{1,p}(\Omega^1, I\!R^3)$, but $\liminf_{h\to 0} e_1^{(h)}[\mathbf{y}^{(h)}]$ is finite, say this number M. Therefore, there exists a subsequence $\mathbf{y}^{(h)}$ (not relabeled) such that

$$\liminf_{h \to 0} e_1^{(h)}[\mathbf{y}^{(h)}] = M < +\infty.$$

By coercivity, $\frac{1}{h}\mathbf{y}_{,3}^{(h)}$ is bounded in $L^p(\Omega^1, I\!R^3)$ and this implies

$$\mathbf{y}_{,3}^{(h)} \to 0 \quad \text{strongly in } L^p(\Omega^1, I\!R^3) \tag{4.19}$$

as $h \to 0$. Since $\mathbf{y}^{(h)}$ converges weakly to $\mathbf{y}$ in $W^{1,p}(\Omega^1, I\!R^3)$ as h tends to zero, this gives

$$\mathbf{y}_{,3}^{(h)} \overset{h}{\rightharpoonup} \mathbf{y}_{,3} \quad \text{in } L^p(\Omega^1, I\!R^3). \tag{4.20}$$

Combining (4.19) and (4.20), we have $\mathbf{y}_{,3} = 0$ a.e. by the uniqueness of the weak limit. Thus, $\mathbf{y} \in V_S$ which contradicts the assumption and this completes the proof. □

4.3 Strong Interfacial Energy

Theorem 1 *Let $e_1^{(h)}$ and $e_1^{(0)}$ be defined by (4.11) and (4.16). Then, $e_1^{(h)}$ Γ-converges to the functional $e_1^{(0)}$ if*

(i) *$\varphi = \varphi(\mathbf{F}, \frac{\mathbf{z}_p}{d})$ and $\frac{\kappa}{d} \to \infty$ as $h \to 0$; further,*

$$\begin{aligned} \bar{\varphi}(\bar{\mathbf{F}}) &= Q\tilde{\varphi}_0(\bar{\mathbf{F}}), \\ \tilde{\varphi}_0(\bar{\mathbf{F}}) &= \inf_{\mathbf{b}\in I\!R^3} \tilde{\varphi}(\bar{\mathbf{F}}|\mathbf{b}), \\ \tilde{\varphi}(\mathbf{F}) &= \int_Z \varphi(\mathbf{F}, \mathbf{z}_p) d\mathbf{z}_p \end{aligned} \tag{4.21}$$

where $Q\tilde{\varphi}_0$ is the lower quasi-convex envelope of $\tilde{\varphi}_0$, $\bar{\mathbf{F}} \in I\!M^{3\times 2}$ and $Z = [0,1]^2$;

(ii) *$\varphi = \varphi(\mathbf{F}, \frac{\mathbf{z}_p}{d}, z_3)$ and $\frac{\kappa}{d} \to \infty, \frac{\kappa}{h} \to \infty$ as $h \to 0$; further, $\bar{\varphi}$ is given by $(4.21)_1$,*

$(4.21)_2$ *with* $(4.21)_3$ *replaced by*

$$\tilde{\varphi}(\mathbf{F}) = \int\limits_{Z\times(0,1)} \varphi(\mathbf{F},\mathbf{z})d\mathbf{z}; \tag{4.22}$$

(iii) $\varphi = \varphi(\mathbf{F}, z_3)$ *and* $\frac{\kappa}{h} \to \infty$ *as* $h \to 0$*; further,* $\bar{\varphi}$ *is given by* $(4.21)_1$, $(4.21)_2$ *with* $(4.21)_3$ *replaced by*

$$\tilde{\varphi}(\mathbf{F}) = \int\limits_0^1 \varphi(\mathbf{F}, z_3)dz_3. \tag{4.23}$$

Remark 2 It is clear that $\tilde{\varphi}(\mathbf{F})$ enjoys the same growth and coercivity conditions (4.8) and is continuous by virtue of the Lipschitz condition (4.9) on φ. It follows that $\tilde{\varphi}_0$ given by $(4.21)_2$ is well defined and the infimum is achieved. Further, Proposition 1 of Le Dret and Raoult [29] shows that $\tilde{\varphi}_0(\bar{\mathbf{F}})$ satisfies the growth and coercivity estimates (4.8) and is continuous. □

Proof of Theorem 1. We begin with the case (i): $\varphi = \varphi(\mathbf{F}, \frac{\mathbf{z}_p}{d})$ and $\frac{\kappa}{d} \to \infty$ as $h \to 0$. We first construct a recovery sequence for any $\mathbf{y} \in V_S$. Recalling Remark 2 and invoking the relaxation theorem due to Dacorogna [25] yields the existence of a sequence $\mathbf{y}^{(\delta)}$ which converges weakly to $\mathbf{y}$ in $W^{1,p}(S, I\!R^3)$ such that

$$\int\limits_S \tilde{\varphi}_0(\nabla_p \mathbf{y}^{(\delta)})d\mathbf{z}_p \to \int\limits_S Q\tilde{\varphi}_0(\nabla_p \mathbf{y})d\mathbf{z}_p \qquad \text{as } \delta \to 0. \tag{4.24}$$

Since the infimum of $\tilde{\varphi}_0$ is achieved (see Remark 2), an argument like that used by Le Dret and Raoult [29] shows that for each element of the sequence $\mathbf{y}^{(\delta)}$, there exists a measurable $\mathbf{b}^{(\delta)} \in L^p(S, I\!R^3)$ such that

$$\tilde{\varphi}_0(\nabla_p \mathbf{y}^{(\delta)}) = \tilde{\varphi}(\nabla_p \mathbf{y}^{(\delta)} | \mathbf{b}^{(\delta)}). \tag{4.25}$$

Further, we may also assume at this moment that both $\mathbf{y}^{(\delta)}(\mathbf{z}_p)$ and $\mathbf{b}^{(\delta)}(\mathbf{z}_p)$ are smooth functions because of the Lipschitz character of ∂S (see Remark 3). Define

$$\mathbf{y}^{(\delta,h)} = \mathbf{y}^{(\delta)}(\mathbf{z}_p) + h\mathbf{b}^{(\delta)}(\mathbf{z}_p)z_3 \tag{4.26}$$

and substitute it into $e_1^{(h)}$, we have

$$\begin{aligned} e_1^{(h)}[\mathbf{y}^{(\delta,h)}] &= \int\limits_{\Omega_1} \left\{\kappa^2\left(|\nabla_p^2\mathbf{y}^{(\delta)} + h\nabla_p^2\mathbf{b}^{(\delta)}z_3|^2 + 2|\nabla_p\mathbf{b}^{(\delta)}|^2\right) + \right. \\ &\qquad\qquad \left. \varphi(\nabla_p\mathbf{y}^{(\delta)} + h\nabla_p(\mathbf{b}^{(\delta)}z_3)\,|\,\mathbf{b}^{(\delta)}, \frac{\mathbf{z}_p}{d})\right\} dz. \end{aligned} \tag{4.27}$$

The first term of the integrand, $\kappa^2\left(|\nabla_p^2\mathbf{y}^{(\delta)} + h\nabla_p^2\mathbf{b}^{(\delta)}z_3|^2 + 2|\nabla_p\mathbf{b}^{(\delta)}|^2\right)$, vanishes for any fixed δ since $\kappa(h) \to 0$ as $h \to 0$. Therefore, using the Lipschitz condition (4.9) on φ yields

$$\begin{aligned} e_1^{(h)}[\mathbf{y}^{(\delta,h)}] &\xrightarrow{h} \int\limits_S\int\limits_Z \varphi(\nabla_p\mathbf{y}^{(\delta)}(\mathbf{z}_p)|\mathbf{b}^{(\delta)}(\mathbf{z}_p), \hat{\mathbf{z}}_p)d\hat{\mathbf{z}}_p d\mathbf{z}_p \\ &= \int\limits_S \tilde{\varphi}(\nabla_p\mathbf{y}^{(\delta)}(\mathbf{z}_p)|\mathbf{b}^{(\delta)}(\mathbf{z}_p))d\mathbf{z}_p \\ &= \int\limits_S \tilde{\varphi}_0(\nabla_p\mathbf{y}^{(\delta)}(\mathbf{z}_p))d\mathbf{z}_p. \end{aligned} \tag{4.28}$$

Above in (4.27), we have approximated $(\nabla_p\mathbf{y}^{(\delta)}\,|\,\mathbf{b}^{(\delta)})$ by a piecewise constant element in $L^p(S, I\!R^9)$, passed to the limit as in (4.28) using the Lemma A.1 by Ball and Murat [7],[1] and then use the estimate (4.9) on φ again to complete the whole argument.

Recalling (4.24) gives

$$\limsup_{\delta\to 0}\limsup_{h\to 0} e_1^{(h)}[\mathbf{y}^{(\delta,h)}] = e_1^{(0)}[\mathbf{y}]. \tag{4.29}$$

Now appealing to the standard diagonalization argument of Attouch (Corollary 1.16) [4] yields a sequence $\mathbf{y}^{(\delta(h))}$ that converges weakly to $\mathbf{y}$ in $W^{1,p}(\Omega^1, I\!R^3)$ as $h \to 0$ and

---

[1] Let $1 \le p \le \infty$ and let $g(\mathbf{x}) \in L^p_{\text{loc}}(I\!R^m)$ be $[0,1]^m$−periodic. Then $g(\frac{\mathbf{x}}{\varepsilon})$ converges weakly in $L^p(\Omega)$ to its mean value as $\varepsilon \to 0$ for any bounded open subset Ω.

satisfies

$$\lim_{h\to 0} e_1^{(h)}[\mathbf{y}^{(\delta(h))}] = e_1^{(0)}[\mathbf{y}]. \tag{4.30}$$

To complete the proof, we need to establish the lower bound. Let $\mathbf{y}^{(h)} \xrightarrow{h} \mathbf{y} \in V_S$ in $W^{1,p}(\Omega^1, \mathbb{R}^3)$. We may assume that $\liminf_{h\to 0} e_1^{(h)}[\mathbf{y}^{(h)}]$ is finite; else the result follows. We may also restrict ourselves to a subsequence $\mathbf{y}^{(h)}$ (not relabeled) which achieves the lim inf. Note that taking further subsequences does not change the lim inf. For any $\delta > 0$ let $S' \subset\subset S$ with $|S \backslash S'| < \delta$. Define

$$\begin{aligned} P^d &= \{\mathbf{z}_p \in d\mathbb{Z}^2 : \mathbf{z}_p + dZ \subset S'\}, \\ S^d &= \bigcup_{\mathbf{z}_p \in P^d} (\mathbf{z}_p + dZ), \\ \Omega^{1,d} &= S^d \times (0,1) \quad \text{and} \quad \Omega' = S' \times (0,1). \end{aligned}$$

Clearly $S^d \subset S'$. For each $\hat{\mathbf{z}}$ in $\Omega^{1,d}$ define

$$\mathbf{Y}^{(h)}(\hat{\mathbf{z}}_p, \hat{z}_3) = \frac{1}{d^2} \int_{\mathbf{z}_p+dZ} (\nabla_p \mathbf{y}^{(h)} | \frac{1}{h} \mathbf{y}^{(h)}_{,3}) d\tilde{\mathbf{z}}_p, \quad \hat{\mathbf{z}}_p \in \mathbf{z}_p + dZ, \quad \mathbf{z}_p \in P^d. \tag{4.31}$$

One can check easily that

$$||\mathbf{Y}^{(h)}||_{L^p(\Omega^{1,d})} \leq ||(\nabla_p \mathbf{y}^{(h)} | \frac{1}{h} \mathbf{y}^{(h)}_{,3})||_{L^p(\Omega^{1,d})}. \tag{4.32}$$

Using the Poincaré inequality for each small square in S^d at fixed z_3, summing all such squares, and integrating over z_3 from 0 to 1, one can deduce that

$$||\mathbf{Y}^{(h)} - (\nabla_p \mathbf{y}^{(h)} | \frac{1}{h} \mathbf{y}^{(h)}_{,3})||^2_{L^2(\Omega^{1,d})} \leq C \, (\frac{d}{\kappa})^2 \int_{\Omega^{1,d}} \kappa^2 \left(|\nabla_p^2 \mathbf{y}^{(h)}|^2 + \frac{1}{h^2} |\nabla_p \mathbf{y}^{(h)}_{,3}|^2 \right) d\mathbf{z} \tag{4.33}$$

where C is some constant that does not depend on h. Using the fact that $\frac{d}{\kappa} \to 0$ as

$h \to 0$ and the finiteness of $\liminf_{h \to 0} e_1^{(h)}[\mathbf{y}^{(h)}]$, we have

$$||\mathbf{Y}^{(h)} - (\nabla_p \mathbf{y}^{(h)}|\frac{1}{h}\mathbf{y}_{,3}^{(h)})||_{L^2(\Omega^{1,d})} \to 0 \qquad \text{as } h \to 0. \tag{4.34}$$

Thus, we can apply Egoroff's theorem to assert the existence of a measurable set A of Ω' such that, for sufficiently small h, $A \subset \Omega^{1,d}$, $|\Omega' \backslash A| < \delta$ and

$$\mathbf{Y}^{(h)} - (\nabla_p \mathbf{y}^{(h)}|\frac{1}{h}\mathbf{y}_{,3}^{(h)}) \to 0 \quad \text{uniformly on } A \tag{4.35}$$

as $h \to 0$ for some subsequence $\left(\mathbf{Y}^{(h)} - (\nabla_p \mathbf{y}^{(h)}|\frac{1}{h}\mathbf{y}_{,3}^{(h)})\right)$ (not relabeled). Using the Lipschitz condition (4.9), (4.32), (4.35) and the uniform boundedness of $||(\nabla_p \mathbf{y}^{(h)}|\frac{1}{h}\mathbf{y}_{,3}^{(h)})||_{L^p(\Omega^1)}$, we have

$$\left(\int_A \varphi(\mathbf{Y}^{(h)}, \frac{\mathbf{z}_p}{d})d\mathbf{z} - \int_A \varphi(\nabla_p \mathbf{y}^{(h)}|\frac{1}{h}\mathbf{y}_{,3}^{(h)}, \frac{\mathbf{z}_p}{d})d\mathbf{z}\right) \to 0 \qquad \text{as } h \to 0. \tag{4.36}$$

Let A_{z_3} be the projection of the slice of A at the constant z_3; i.e.,

$$A_{z_3} = \{(z_1, z_2) : (z_1, z_2, z_3) \in A\}. \tag{4.37}$$

Also, pick any $\hat{\mathbf{z}}_p \in P^d$ and let

$$Q_S = \hat{\mathbf{z}}_p + dZ, \quad \text{and} \quad Q = \{(\mathbf{z}_p, z_3) : \mathbf{z}_p \in Q_S,\ z_3 \in (0,1)\}, \tag{4.38}$$

and notice that $\mathbf{Y}^{(h)}$ is constant over Q_S for any fixed $z_3 \in (0,1)$. Thus, using Fubini's theorem, we have

$$\int_{A \cap Q} \varphi(\mathbf{Y}^{(h)}, \frac{\mathbf{z}_p}{d})d\mathbf{z} = \int_0^1 \int_{Q_S \cap A_{z_3}} \varphi(\mathbf{Y}^{(h)}, \frac{\mathbf{z}_p}{d})d\mathbf{z}_p dz_3$$

and

$$\begin{aligned}\int\limits_{Q_S \cap A_{z_3}} \varphi(\mathbf{Y}^{(h)}, \frac{\mathbf{z}_p}{d}) d\mathbf{z}_p &= \int\limits_{Q_S} \varphi(\mathbf{Y}^{(h)}, \frac{\mathbf{z}_p}{d}) d\mathbf{z}_p - \int\limits_{Q_S \backslash A_{z_3}} \varphi(\mathbf{Y}^{(h)}, \frac{\mathbf{z}_p}{d}) d\mathbf{z}_p \\ &\geq \int\limits_{Q_S} \tilde{\varphi}(\mathbf{Y}^{(h)}) d\mathbf{z}_p - c_2(1 + |\mathbf{Y}^{(h)}|^p)\, |Q_S \backslash A_{z_3}| \qquad (4.39)\end{aligned}$$

where we have used the second inequality in (4.8). Using the other inequality in (4.8), we have

$$\int\limits_{Q_S \cap A_{z_3}} \varphi(\mathbf{Y}^{(h)}, \frac{\mathbf{z}_p}{d}) d\mathbf{z}_p \geq c_1 \left(|\mathbf{Y}^{(h)}|^p - 1 \right) |Q_S \cap A_{z_3}|. \qquad (4.40)$$

Combining (4.39) and (4.40), we obtain

$$\int\limits_{Q_S \cap A_{z_3}} \varphi(\mathbf{Y}^{(h)}, \frac{\mathbf{z}_p}{d}) d\mathbf{z}_p \geq \int\limits_{Q_S} \mu^{(d)}(\mathbf{z}) \tilde{\varphi}(\mathbf{Y}^{(h)}) d\mathbf{z}_p - 2\, c_2 \int\limits_{Q_S \backslash A_{z_3}} \mu^{(d)}(\mathbf{z}) d\mathbf{z}_p \qquad (4.41)$$

where

$$\begin{aligned}\mu^{(d)}(\mathbf{z}) &= \frac{c_1 |Q_S \cap A_{z_3}|}{c_1 |Q_S \cap A_{z_3}| + c_2 |Q_S \backslash A_{z_3}|} \\ &= \frac{c_1 \fint_{\hat{\mathbf{z}}_p + dZ} \chi_{A_{z_3}}(\tilde{\mathbf{z}}_p) d\tilde{\mathbf{z}}_p}{(c_1 - c_2) \fint_{\hat{\mathbf{z}}_p + dZ} \chi_{A_{z_3}}(\tilde{\mathbf{z}}_p) d\tilde{\mathbf{z}}_p + c_2} \quad \text{for} \quad \mathbf{z} \in Q \qquad (4.42)\end{aligned}$$

and $\chi_{A_{z_3}}$ is the characteristic function of the set A_{z_3}. Integrating (4.41) over z_3 from 0 to 1 and summing the same equation over all $\hat{\mathbf{z}}_p$ in P^d, this gives

$$\int\limits_{A} \varphi(\mathbf{Y}^{(h)}, \frac{\mathbf{z}_p}{d}) d\mathbf{z} \geq \int\limits_{\Omega^{1,d}} \mu^{(d)}(\mathbf{z}) \tilde{\varphi}(\mathbf{Y}^{(h)}) d\mathbf{z} - 2\, c_2 \int\limits_{\Omega^{1,d} \backslash A} \mu^{(d)}(\mathbf{z}) d\mathbf{z}. \qquad (4.43)$$

Invoking the Lebesgue point theorem on (4.42) as $d \to 0$ as $h \to 0$ for each fixed z_3, we have

$$\mu^{(d)}(\mathbf{z}_p, z_3) \to \frac{c_1 \chi_{A_{z_3}}(\mathbf{z}_p)}{c_1 \chi_{A_{z_3}}(\mathbf{z}_p) + c_2(1 - \chi_{A_{z_3}}(\mathbf{z}_p))} = \chi_{A_{z_3}}(\mathbf{z}_p), \quad \text{a.e.} \quad \text{on} \quad \Omega', \qquad (4.44)$$

and (4.43) becomes

$$\liminf_{h\to 0}\int_A \varphi(\mathbf{Y}^{(h)},\frac{\mathbf{z}_p}{d})d\mathbf{z} \geq \liminf_{h\to 0}\int_A \mu^{(d)}(\mathbf{z})\tilde{\varphi}(\mathbf{Y}^{(h)})d\mathbf{z}. \tag{4.45}$$

Recalling (4.36), (4.45), (4.35), and the fact that φ is nonnegative, we obtain

$$\begin{aligned}
\liminf_{h\to 0}\int_\Omega \varphi(\nabla_p\mathbf{y}^{(h)}|\frac{1}{h}\mathbf{y}^{(h)}_{,3},\frac{\mathbf{z}_p}{d})d\mathbf{z} &\geq \liminf_{h\to 0}\int_A \varphi(\nabla_p\mathbf{y}^{(h)}|\frac{1}{h}\mathbf{y}^{(h)}_{,3},\frac{\mathbf{z}_p}{d})d\mathbf{z}\\
&= \liminf_{h\to 0}\int_A \varphi(\mathbf{Y}^{(h)},\frac{\mathbf{z}_p}{d})d\mathbf{z}\\
&\geq \liminf_{h\to 0}\int_A \mu^{(d)}(\mathbf{z})\tilde{\varphi}(\mathbf{Y}^{(h)})d\mathbf{z}\\
&= \liminf_{h\to 0}\int_A \mu^{(d)}(\mathbf{z})\tilde{\varphi}(\nabla_p\mathbf{y}^{(h)}|\frac{1}{h}\mathbf{y}^{(h)}_{,3})d\mathbf{z}\\
&\geq \liminf_{h\to 0}\int_A \mu^{(d)}(\mathbf{z})\tilde{\varphi}_0(\nabla_p\mathbf{y}^{(h)})d\mathbf{z}. \qquad (4.46)
\end{aligned}$$

Now, invoking the Egoroff's theorem yields the existence of a measurable subset $A' \subset A$ with $|A\backslash A'| < \delta'$ such that for some subsequence (not relabeled)

$$\mu^{(d)} \to \chi_{A_{z_3}} \equiv 1 \quad \text{uniformly on} \quad A'$$

as $d \to 0$ as $h \to 0$. Therefore, for any $\eta > 0$, we have

$$\begin{aligned}
\liminf_{h\to 0}\int_A \mu^{(d)}(\mathbf{z})\tilde{\varphi}_0(\nabla_p\mathbf{y}^{(h)})d\mathbf{z} &\geq \liminf_{h\to 0}\int_{A'} \mu^{(d)}(\mathbf{z})\tilde{\varphi}_0(\nabla_p\mathbf{y}^{(h)})d\mathbf{z}\\
&\geq \liminf_{h\to 0}\int_{A'} (1-\eta)Q\tilde{\varphi}_0(\nabla_p\mathbf{y}^{(h)})d\mathbf{z}. \qquad (4.47)
\end{aligned}$$

If we define $G : W^{1,p}(\Omega^1, I\!R^3) \to I\!R$ by

$$G(\hat{\mathbf{y}}) = \int_{\Omega^1} Q\tilde{\varphi}_0(\nabla_p\hat{\mathbf{y}})d\mathbf{z}$$

and set $\Phi : I\!M^{3\times 3} \to I\!R$ to be $\Phi(\mathbf{f}_1|\mathbf{f}_2|\mathbf{f}_3) = Q\tilde{\varphi}_0(\mathbf{f}_1|\mathbf{f}_2)$. Since $Q\tilde{\varphi}_0$ is quasiconvex, it can be shown [29] that Φ is also quasiconvex, bounded below by $-c_1$ and satisfies the similar growth and coercivity conditions (4.8). Then G is sequentially lower semicontinuous on $W^{1,p}(\Omega^1, I\!R^3)$ (see Acerbi and Fusco [2]). Applying this result to $\int_{\Omega^1}(1-\eta)\chi_{A'}Q\tilde{\varphi}_0(\nabla_p\mathbf{y}^{(h)})d\mathbf{z}$, we have

$$\liminf_{h\to 0}\int_{A'}(1-\eta)Q\tilde{\varphi}_0(\nabla_p\mathbf{y}^{(h)})d\mathbf{z} \geq \int_{A'}(1-\eta)Q\tilde{\varphi}_0(\nabla_p\mathbf{y})d\mathbf{z}.$$

By letting δ' and η tend to zero, we have

$$\liminf_{h\to 0}\int_{A}\mu^{(d)}(\mathbf{z})\tilde{\varphi}_0(\nabla_p\mathbf{y}^{(h)})d\mathbf{z} \geq \int_{A}Q\tilde{\varphi}_0(\nabla_p\mathbf{y})d\mathbf{z}.$$

Combining with (4.46) yields

$$\liminf_{h\to 0}\int_{A}\varphi(\nabla_p\mathbf{y}^{(h)}|\frac{1}{h}\mathbf{y}^{(h)}_{,3},\frac{\mathbf{z}_p}{d})d\mathbf{z} \geq \int_{A}Q\tilde{\varphi}_0(\nabla_p\mathbf{y})d\mathbf{z}.$$

Using the fact that $Q\tilde{\varphi}_0(\nabla_p\mathbf{y})$ belongs to $L^1(\Omega^1)$ and $|\Omega^1\backslash A| < 2\delta$, we obtain the desired lower bound by letting $\delta \to 0$.

We now consider the case (ii); i.e., $\varphi = \varphi(\mathbf{F}, \frac{\mathbf{z}_p}{d}, z_3)$ and $\frac{\kappa}{d} \to \infty, \frac{\kappa}{h} \to \infty$ as $h \to 0$. We can construct the recovery sequence in a way similar to the previous case without any difficulty. Next, the proof of the lower bound is also similar, except we have to replace (4.31) by

$$\mathbf{Y}^{(h)}(\hat{\mathbf{z}}_p) = \frac{1}{d^2}\int_0^1\int_{\mathbf{z}_p+dZ}(\nabla_p\mathbf{y}^{(h)}|\frac{1}{h}\mathbf{y}^{(h)}_{,3})d\tilde{\mathbf{z}}_p d\tilde{z}_3, \quad \hat{\mathbf{z}}_p \in \mathbf{z}_p + dZ, \quad \mathbf{z}_p \in P^d.$$

Note that (4.32) remains valid, but (4.33) becomes

$$\begin{aligned} \|\mathbf{Y}^{(h)} - (\nabla_p \mathbf{y}^{(h)} | \frac{1}{h}\mathbf{y}_{,3}^{(h)})\|_{L^2(\Omega^{1,d})}^2 &\leq C(\frac{d}{\kappa})^2 \int\limits_{\Omega^{1,d}} \kappa^2 \left(|\nabla_p^2 \mathbf{y}^{(h)}|^2 + \frac{1}{h^2}|\nabla_p \mathbf{y}_{,3}^{(h)}|^2 \right) d\mathbf{z} \\ &+ C(\frac{h}{\kappa})^2 \int\limits_{\Omega^{1,d}} \kappa^2 \left(\frac{1}{h^2}|\nabla_p \mathbf{y}_{,3}^{(h)}|^2 + \frac{1}{h^4}|\mathbf{y}_{,33}^{(h)}|^2 \right) d\mathbf{z} \end{aligned}$$

where C is some constant that does not depend on h. Since both $\frac{\kappa}{d} \to \infty, \frac{\kappa}{h} \to \infty$ as $h \to 0$, we obtain (4.34). The rest of the proof is similar and we omit here.

Finally, the case (iii) ($\varphi = \varphi(\mathbf{F}, z_3)$ and $\frac{\kappa}{h} \to \infty$ as $h \to 0$) follows from the case (ii). $\square$

Remark 3 For each $\delta > 0$, $\mathbf{y}^{(\delta)} \in W^{1,p}(S, I\!R^3)$ and $\mathbf{b}^{(\delta)} \in L^p(S, I\!R^3)$, the bounded Lipschitz domain permits the existence of sequences $\mathbf{y}^{(\delta,\varepsilon)} \in C^\infty(\bar{S}, I\!R^3)$ and $\mathbf{b}^{(\delta,\varepsilon)} \in C_0^\infty(S, I\!R^3)$ such that

$$\begin{aligned} \mathbf{y}^{(\delta,\varepsilon)} \to \mathbf{y}^{(\delta)} \quad &\text{strongly in} \quad W^{1,p}(S, I\!R^3) \\ \mathbf{b}^{(\delta,\varepsilon)} \to \mathbf{b}^{(\delta)} \quad &\text{strongly in} \quad L^p(S, I\!R^3) \end{aligned}$$

as $\varepsilon \to 0$. Then, (4.26) is replaced by

$$\mathbf{y}^{(\delta,\varepsilon,h)} = \mathbf{y}^{(\delta,\varepsilon)} + h\mathbf{b}^{(\delta,\varepsilon)}(\mathbf{z}_p)z_3$$

and (4.29) now becomes

$$\limsup_{\delta \to 0} \limsup_{\varepsilon \to 0} \limsup_{h \to 0} e_1^{(h)}[\mathbf{y}^{(\delta,\varepsilon,h)}] = e_1^{(0)}[\mathbf{y}].$$

Appealing to the already quoted diagonalization argument yields the existence of a recovery sequence labeled only in terms of h and thus (4.30). $\square$

4.4 Film Thickness Much Smaller than Heterogeneity

Theorem 2 *Suppose* $\varphi = \varphi(\mathbf{F}, \frac{\mathbf{z}_p}{d})$ *and* $\frac{\kappa}{d} \to \alpha$ *and* $\frac{h}{d} \to 0$ *as* $h \to 0$. *Let* $\bar{\mathbf{F}} \in I\!M^{3\times 2}$, $Z = [0,1]^2$ *and* $e_1^{(h)}$ *be defined by (4.11). Then,* $e_1^{(h)}$ Γ*-converges to the functional* $e_1^{(0)}$ *defined by (4.16) if*

(i) $\alpha = 0$ *and*

$$\bar{\varphi}(\bar{\mathbf{F}}) = \inf_{k\in I\!N} \inf_{\omega\in W_0^{1,p}(kZ)} \fint_{kZ} \varphi_0(\bar{\mathbf{F}} + \nabla_p\omega, \mathbf{z}_p)d\mathbf{z}_p \tag{4.48}$$

$$\varphi_0(\bar{\mathbf{F}}^0, \mathbf{z}_p^0) = \inf_{\mathbf{b}\in I\!R^3} \varphi(\bar{\mathbf{F}}^0|\mathbf{b}, \mathbf{z}_p^0); \tag{4.49}$$

(ii) $\alpha > 0$ *and*

$$\bar{\varphi}(\bar{\mathbf{F}}) = \inf_{k\in I\!N} \inf_{\substack{\omega\in W_0^{1,p}(kZ)\cap W_0^{2,2}(kZ)\\ \mathbf{b}\in L^p(kZ)\cap W_0^{1,2}(kZ)}} \fint_{kZ} \left\{\alpha^2\left(|\nabla_p^2\omega|^2 + 2|\nabla_p\mathbf{b}|^2\right) + \varphi(\bar{\mathbf{F}} + \nabla_p\omega|\mathbf{b}, \mathbf{z}_p)\right\} d\mathbf{z}_p; \tag{4.50}$$

(iii) $\alpha = \infty$ *and*

$$\bar{\varphi}(\bar{\mathbf{F}}) = Q\tilde{\varphi}_0(\bar{\mathbf{F}}),$$

$$\tilde{\varphi}_0(\bar{\mathbf{F}}) = \inf_{\mathbf{b}\in I\!R^3} \tilde{\varphi}(\bar{\mathbf{F}}|\mathbf{b}), \qquad \tilde{\varphi}(\mathbf{F}) = \int_Z \varphi(\mathbf{F}, \mathbf{z}_p)d\mathbf{z}_p$$

where $Q\tilde{\varphi}_0$ *is the lower quasi-convex envelope of* $\tilde{\varphi}_0$.

Remark 4 It can be shown that the effective energy density satisfies the growth and Lipschitz condition for $0 \le \alpha \le \infty$; i.e.,

$$c_1(|\bar{\mathbf{F}}|^p - 1) \le \bar{\varphi}(\bar{\mathbf{F}}) \le c_2(|\bar{\mathbf{F}}|^p + 1) \tag{4.51}$$

$$|\bar{\varphi}(\bar{\mathbf{F}}) - \bar{\varphi}(\bar{\mathbf{G}})| \le c_2'(1 + |\bar{\mathbf{F}}|^{p-1} + |\bar{\mathbf{G}}|^{p-1})|\bar{\mathbf{F}} - \bar{\mathbf{G}}| \tag{4.52}$$

for all $(\bar{\mathbf{F}}, \bar{\mathbf{G}}) \in I\!M^{3\times 2} \times I\!M^{3\times 2}$. Suppose $0 < \alpha < \infty$. The upper bound is obtained by setting $\omega = \mathbf{b} = 0$ in (4.50) and using (4.8) on φ. To show the lower bound, note that for every $\varepsilon > 0$, there exists $k \in I\!N, \omega \in W_0^{1,p}(kZ, I\!R^3) \cap W_0^{2,2}(kZ, I\!R^3)$ and $\mathbf{b} \in L^p(kZ, I\!R^3) \cap W_0^{1,2}(kZ, I\!R^3)$ such that

$$\bar{\varphi}(\bar{\mathbf{F}}) \leq \fint_{kZ} \left\{\alpha^2 \left(|\nabla_p^2 \omega|^2 + 2|\nabla_p \mathbf{b}|^2\right) + \varphi(\bar{\mathbf{F}} + \nabla_p \omega|\mathbf{b}, \mathbf{z}_p)\right\} d\mathbf{z}_p \leq \bar{\varphi}(\bar{\mathbf{F}}) + \varepsilon. \quad (4.53)$$

Using (4.8) on φ yields

$$\begin{aligned} \bar{\varphi}(\bar{\mathbf{F}}) + \varepsilon &\geq c_1 \left(\fint_{kZ} |\bar{\mathbf{F}} + \nabla_p \omega|\mathbf{b}|^p d\mathbf{z}_p - 1 \right) \\ &\geq c_1 \left(\fint_{kZ} |\bar{\mathbf{F}} + \nabla_p \omega|^p d\mathbf{z}_p - 1 \right) \\ &\geq c_1 \left(\left| \fint_{kZ} (\bar{\mathbf{F}} + \nabla_p \omega) d\mathbf{z}_p \right|^p - 1 \right) \geq c_1 \left(|\bar{\mathbf{F}}|^p - 1\right) \end{aligned}$$

since $|\cdot|^p$ is convex and $|\bar{\mathbf{F}}|\mathbf{b}|_{3\times3} \geq |\bar{\mathbf{F}}|_{3\times2}$ for all $\mathbf{b} \in I\!R^3$. To prove the Lipschitz condition for $\alpha > 0$, choosing the same ω and $\mathbf{b}$ as the test functions for $\bar{\varphi}(\bar{\mathbf{G}})$, we have

$$\begin{aligned} \bar{\varphi}(\bar{\mathbf{G}}) - \bar{\varphi}(\bar{\mathbf{F}}) &\leq \fint_{kZ} \left| \varphi(\bar{\mathbf{G}} + \nabla_p \omega|\mathbf{b}, \mathbf{z}_p) - \varphi(\bar{\mathbf{F}} + \nabla_p \omega|\mathbf{b}, \mathbf{z}_p) \right| d\mathbf{z}_p + \varepsilon \\ &\leq C \left(1 + \frac{1}{k^2} \left\|\bar{\mathbf{G}} + \nabla_p \omega|\mathbf{b}\right\|_{L^p}^p \right. \\ &\qquad \left. + \frac{1}{k^2} \left\|\bar{\mathbf{F}} + \nabla_p \omega|\mathbf{b}\right\|_{L^p}^p \right)^{\frac{p-1}{p}} \left|\bar{\mathbf{G}} - \bar{\mathbf{F}}\right| + \varepsilon. \end{aligned} \quad (4.54)$$

Now invoking the growth conditions on φ, $\bar{\varphi}$ and (4.53) gives

$$\begin{aligned} C\left(\frac{1}{k^2} \left\|\bar{\mathbf{F}} + \nabla_p \omega|\mathbf{b}\right\|_{L^p}^p - 1\right) &\leq \fint \varphi(\bar{\mathbf{F}} + \nabla_p \omega|\mathbf{b}, \mathbf{z}_p) d\mathbf{z}_p \\ &\leq \bar{\varphi}(\bar{\mathbf{F}}) + \varepsilon \leq c_2(|\bar{\mathbf{F}}|^p + 1) + \varepsilon \end{aligned} \quad (4.55)$$

and

$$\frac{1}{k^2}\left\|\bar{\mathbf{G}}+\nabla_p\omega|\mathbf{b}\right\|^p_{L^p} \leq C(|\bar{\mathbf{G}}-\bar{\mathbf{F}}|^p + \frac{1}{k^2}\left\|\bar{\mathbf{F}}+\nabla_p\omega|\mathbf{b}\right\|^p_{L^p}). \tag{4.56}$$

Collecting (4.54)-(4.56) gives

$$\bar{\varphi}(\bar{\mathbf{G}}) - \bar{\varphi}(\bar{\mathbf{F}}) \leq c_2'(1+|\bar{\mathbf{F}}|^{p-1}+|\bar{\mathbf{G}}|^{p-1})|\bar{\mathbf{F}}-\bar{\mathbf{G}}| + \varepsilon. \tag{4.57}$$

We have the desired inequality as $\varepsilon \to 0$. The opposite inequality can be obtained by interchanging $\bar{\mathbf{F}}$ and $\bar{\mathbf{G}}$. The case $\alpha = 0$ and $\alpha = \infty$ can also be treated similarly. $\square$

Proof of Theorem 2. The case $\alpha = \infty$ is a corollary of Theorem 1. The proof for finite $\alpha \geq 0$ consists of two parts. First, we prove the Γ-limit in the case where the limit function is affine (Part A). We then prove the general case by approximating an arbitrary function by piecewise affine functions (Part B). We will give a detailed argument in Part A. After that, we simply sketch the steps for general $\mathbf{y} \in V_S$ in Part B.

Part A. Suppose $\mathbf{y} = \bar{\mathbf{F}}\mathbf{z}_p$ with $\bar{\mathbf{F}} \in I\!M^{3\times 2}$. We begin by constructing a recovery sequence for the case where $\alpha > 0$. It follows from the definition of $\bar{\varphi}$ that there exists sequences $k^{(\varepsilon)} \in I\!N$, $\omega^{(\varepsilon)} \in W_0^{1,p}(k^{(\varepsilon)}Z, I\!R^3) \cap W_0^{2,2}(k^{(\varepsilon)}Z, I\!R^3)$, and $\mathbf{b}^{(\varepsilon)} \in L^p(k^{(\varepsilon)}Z, I\!R^3) \cap W_0^{1,2}(k^{(\varepsilon)}Z, I\!R^3)$ such that

$$\frac{1}{k^{(\varepsilon)2}} \int\limits_{k^{(\varepsilon)}Z} \left\{\alpha^2\left(|\nabla_p^2\omega^{(\varepsilon)}|^2 + 2|\nabla_p\mathbf{b}^{(\varepsilon)}|^2\right) + \varphi(\bar{\mathbf{F}}+\nabla_p\omega^{(\varepsilon)}\,|\,\mathbf{b}^{(\varepsilon)}, \mathbf{z}_p)\right\} d\mathbf{z}_p \to \bar{\varphi}(\bar{\mathbf{F}}) \tag{4.58}$$

as $\varepsilon \to 0$. We use $\omega^{(\varepsilon)}$ and $\mathbf{b}^{(\varepsilon)}$ to construct our recovery sequence. Unfortunately, $\mathbf{b}^{(\varepsilon)}$ may not be smooth enough to allow second differentiation. However, using the approximation argument similar to Remark 3 shows that we may assume that $\mathbf{b}^{(\varepsilon)} \in C_0^\infty(k^{(\varepsilon)}Z, I\!R^3)$. Define

$$\mathbf{y}^{(h,\varepsilon)} = \bar{\mathbf{F}}\mathbf{z}_p + d\,\omega^{(\varepsilon)}(\frac{\mathbf{z}_p}{d}) + h\mathbf{b}^{(\varepsilon)}(\frac{\mathbf{z}_p}{d})z_3 \tag{4.59}$$

where $\omega^{(\varepsilon)}$ and $\mathbf{b}^{(\varepsilon)}$ are extended periodically in the plane of the film since $\omega^{(\varepsilon)} = \frac{\partial \omega^{(\varepsilon)}}{\partial n} = \mathbf{b}^{(\varepsilon)} = \frac{\partial \mathbf{b}^{(\varepsilon)}}{\partial n} = 0$ on $\partial k^{(\varepsilon)} Z$ in the sense of trace. Clearly, $\mathbf{y}^{(h,\varepsilon)} \xrightarrow{h} \bar{\mathbf{F}} \mathbf{z}_p$ for each $\varepsilon > 0$. Substituting (4.59) into $e_1^{(h)}$ defined by (4.11), we have

$$\begin{aligned} e_1^{(h)}[\mathbf{y}^{(h,\varepsilon)}] &= \int\limits_{\Omega^1} \left\{ \left(\left| \frac{\kappa}{d} \nabla_p^2 \omega^{(\varepsilon)} + \frac{h}{d} \cdot \frac{\kappa}{d} \nabla_p^2 \mathbf{b}^{(\varepsilon)} z_3 \right|^2 + 2 \left| \frac{\kappa}{d} \nabla_p \mathbf{b}^{(\varepsilon)} \right|^2 \right) \right. \\ &+ \left. \varphi(\bar{\mathbf{F}} + \nabla_p \omega^{(\varepsilon)} + \frac{h}{d} \nabla_p \mathbf{b} z_3 \,|\, \mathbf{b}^{(\varepsilon)}, \frac{\mathbf{z}_p}{d}) \right\} d\mathbf{z}. \end{aligned} \tag{4.60}$$

By assumption that $\frac{h}{d} \to 0$ and $\frac{\kappa}{d} \to \alpha$ as $h \to 0$, invoking the Lipschitz condition (4.9) on φ yields

$$e_1^{(h)}[\mathbf{y}^{(h,\varepsilon)}] \to \frac{|\Omega^1|}{k^{(\varepsilon)2}} \int\limits_{k^{(\varepsilon)}Z} \left\{ \alpha^2 \left(|\nabla_p^2 \omega^{(\varepsilon)}|^2 + 2 |\nabla_p \mathbf{b}^{(\varepsilon)}|^2 \right) + \varphi(\bar{\mathbf{F}} + \nabla_p \omega^{(\varepsilon)} \,|\, \mathbf{b}^{(\varepsilon)}, \mathbf{z}_p) \right\} d\mathbf{z}_p \tag{4.61}$$

as $h \to 0$. Above, we have applied the property of mean value[2] to (4.60) in deriving (4.61). Then, using (4.58) gives

$$\limsup_{\varepsilon \to 0} \limsup_{h \to 0} e_1^{(h)}[\mathbf{y}^{(h,\varepsilon)}] = |\Omega^1| \, \bar{\varphi}(\bar{\mathbf{F}}) = |S| \, \bar{\varphi}(\bar{\mathbf{F}}) = e_1^{(0)}[\mathbf{y}]. \tag{4.62}$$

Recalling (4.59) and (4.62) and appealing to the standard diagonalization argument yields the existence of a sequence $\hat{\mathbf{y}}^{(h)} = \mathbf{y}^{(h,\varepsilon(h))}$ that converges weakly to $\mathbf{y} = \bar{\mathbf{F}} \mathbf{z}_p$ in $W^{1,p}(\Omega^1, I\!R^3)$ and satisfies

$$\lim_{h \to 0} e_1^{(h)}[\hat{\mathbf{y}}^{(h)}] = e_1^{(0)}[\mathbf{y}].$$

The case of $\alpha = 0$ is similar. Indeed, using an argument similar to Remark 2 shows that (4.49) is well defined and the infimum is also achieved. From the definition of $\bar{\varphi}$, there exists sequences $k^{(\varepsilon)} \in I\!N$, $\omega^{(\varepsilon)} \in W_0^{1,p}(k^{(\varepsilon)} Z, I\!R^3)$ such that

$$\frac{1}{k^{(\varepsilon)2}} \int\limits_{k^{(\varepsilon)}Z} \varphi_0(\bar{\mathbf{F}} + \nabla_p \omega^{(\varepsilon)}, \mathbf{z}_p) d\mathbf{z}_p \to \bar{\varphi}(\bar{\mathbf{F}})$$

---

[2] ibid 1.

as $\varepsilon \to 0$. Following an argument like that used in (4.25) gives measurable functions $\mathbf{b}^{(\varepsilon)} \in L^p(k^{(\varepsilon)}Z, I\!R^3)$ such that

$$\varphi_0(\bar{\mathbf{F}} + \nabla_p \omega^{(\varepsilon)}, \mathbf{z}_p) = \varphi(\bar{\mathbf{F}} + \nabla_p \omega^{(\varepsilon)} \,|\, \mathbf{b}^{(\varepsilon)}, \mathbf{z}_p) \tag{4.63}$$

for almost all $\mathbf{z}_p \in k^{(\varepsilon)}Z$. The rest of the proof follows similarly.

A slight refinement (see Lemma 2.1 in Müller [67]) shows that the recovery sequence $\mathbf{y}^{(h)}$ can in fact be constructed such that

$$\omega^{(h)} = \mathbf{y}^{(h)} - \bar{\mathbf{F}}\mathbf{z}_p \in V, \qquad \omega^{(h)} = \frac{\partial \omega^{(h)}}{\partial n} = 0 \tag{4.64}$$

on $\Sigma = \partial S \times (0,1)$ in the sense of trace.

We now turn to the lower bound when $\mathbf{y}$ is an affine function and $\alpha > 0$. We assume that S is a square domain with side length s. Set $\omega^{(h)} = \mathbf{y}^{(h)} - \bar{\mathbf{F}}\mathbf{z}_p$ and assume also that (4.64) holds; we have

$$\omega^{(h)} \in V \xrightarrow{h} 0 \;\text{ in }\; W^{1,p}(\Omega^1, I\!R^3) \quad \text{and} \quad \omega^{(h)} = \frac{\partial \omega^{(h)}}{\partial n} = 0 \tag{4.65}$$

on $\Sigma = \partial S \times (0,1)$ in the sense of trace. We may also assume that $\liminf_{h\to 0} e_1^{(h)}[\mathbf{y}^{(h)}]$ is finite; otherwise the proof is trivial. Choose $k \in I\!N$ to be smallest integer such that $k\,d \geq s + d$. We can find a square $\tilde{S}^{(d)}$ with the side length kd such that $S \subset \tilde{S}^{(d)}$ and the corners of $\tilde{S}^{(d)}$ are in $d\mathbb{Z}^2$; i.e., $\tilde{S}^{(d)} = d(\mathbf{z}_p^0 + kZ)$ for some $\mathbf{z}_p^0 \in \mathbb{Z}^2$. Now extending $\omega^{(h)}$ to $\tilde{S}^{(d)}$ by

$$\tilde{\omega}^{(h)} = \begin{cases} \omega^{(h)}, & \text{for } \;\mathbf{z} \in S \times (0,1), \\ 0, & \text{for } \;\mathbf{z} \in (\tilde{S}^{(d)} \backslash S) \times (0,1), \end{cases}$$

we have

$$
\begin{aligned}
e_1^{(h)}[\mathbf{y}^{(h)}] &= \int\limits_{\tilde{S}^{(d)}\times(0,1)} \left\{\kappa^2\left(|\nabla_p^2\tilde{\omega}^{(h)}|^2+\frac{2}{h^2}|\nabla_p\tilde{\omega}_{,3}^{(h)}|^2+\frac{1}{h^4}|\tilde{\omega}_{,33}^{(h)}|^2\right)\right.\\
&\qquad\left.+\ \varphi(\bar{\mathbf{F}}+\nabla_p\tilde{\omega}^{(h)}\,|\,\frac{1}{h}\tilde{\omega}_{,3},\frac{\mathbf{z}_p}{d})\right\}\,d\mathbf{z}-\int\limits_{(\tilde{S}^{(d)}\backslash S)\times(0,1)}\varphi(\bar{\mathbf{F}}|0,\frac{\mathbf{z}_p}{d}))d\mathbf{z}\\
&= I_1-I_2.
\end{aligned}
$$

The second integral $-I_2 \geq -c_2(1+|\bar{\mathbf{F}}|^p)|\tilde{S}^{(d)}\backslash S|$ converges to zero since $|\tilde{S}^{(d)}\backslash S| \leq (s+2d)^2-s^2 \to 0$ as d tends to zero as h tends to zero. Changing variables $\mathbf{z}_p \mapsto d(\mathbf{z}_p^0+\hat{\mathbf{z}}_p)$ and $z_3 \mapsto \frac{d}{h}\hat{z}_3$, using the periodicity of φ and Fubini's theorem, we have

$$
I_1 \geq d^2\cdot\frac{d}{h}\cdot\int_0^{\frac{h}{d}}\int_{kZ}\left\{\alpha^2\left(|\nabla_p^2\hat{\omega}^{(h)}|^2+2\,|\nabla_p\hat{\omega}_{,3}^{(h)}|^2\right)+\varphi(\bar{\mathbf{F}}+\nabla_p\hat{\omega}^{(h)}\,|\,\hat{\omega}_{,3}^{(h)},\hat{\mathbf{z}}_p)\right\}\,d\hat{\mathbf{z}}_p d\hat{z}_3
$$

where

$$
\hat{\omega}^{(h)}(\hat{\mathbf{z}}_p,\hat{z}_3)=\frac{1}{d}\tilde{\omega}^{(h)}(d\hat{\mathbf{z}}_p,\frac{d}{h}\hat{z}_3). \tag{4.66}
$$

Notice that for almost every $\hat{z}_3 \in (0,\frac{h}{d})$, the function $\hat{\omega}_{\hat{z}_3}^{(h)}(\hat{\mathbf{z}}_p)=\hat{\omega}^{(h)}(\hat{\mathbf{z}}_p,\hat{z}_3)$ belongs to $W_0^{1,p}(kZ,I\!R^3)\cap W_0^{2,2}(kZ,I\!R^3)$. Similarly, for almost every $\hat{z}_3 \in (0,\frac{h}{d})$, $\hat{\omega}_{,3}^{(h)}$ belongs to $L^p(kZ,I\!R^3)\cap W_0^{1,2}(kZ,I\!R^3)$. It follows that

$$
I_1 \ \geq\ d^2\cdot\frac{d}{h}\cdot\int_0^{\frac{h}{d}} k^2\,\bar{\varphi}(\bar{\mathbf{F}})dz_3 \geq (dk)^2\bar{\varphi}(\bar{\mathbf{F}}) \geq s^2\bar{\varphi}(\bar{\mathbf{F}}).
$$

Thus, we have shown that $\liminf_{h\to 0} e_1^{(h)}[\mathbf{y}^{(h)}] \geq s^2\bar{\varphi}(\bar{\mathbf{F}}) = e_1^{(0)}[\mathbf{y}]$ which is the desired lower bound.

For the general domain S, assume the sequence $\mathbf{y}^{(h)}$ satisfy (4.65). Consider a square Q which contains S. Using the fact the recovery sequence can be obtained such that (4.64) is satisfied for the domain $(Q\backslash S)\times(0,1)$, we can also obtain the lower bound.

Now let S be any open bounded Lipschitz domain and let $\mathbf{y}^{(h)} \overset{h}{\rightharpoonup} \mathbf{y} = \bar{\mathbf{F}}\mathbf{z}_p$ in $W^{1,p}(\Omega^1, \mathbb{R}^3)$. No further assumption such as (4.65) is imposed on $\mathbf{y}^{(h)}$. We use the argument of De Giorgi [38] (see also Francfort and Müller [37]) to obtain the lower bound. Fix S_0 open and compactly contained in S. Let

$$R = \frac{1}{2}\mathrm{dist}(S_0, \partial S).$$

For any strictly positive integer ν, define

$$S_i = \left\{ \mathbf{z}_p \in S : \mathrm{dist}(\mathbf{z}_p, S_0) < \frac{i}{\nu}R \right\}, \quad 1 \le i \le \nu,$$

and scalar functions $\eta_i(\mathbf{z}_p) \in C_0^\infty(S)$ such that

$$\begin{cases} 0 \le \eta_i \le 1, \\ \eta_i = 1 \quad \text{in} \quad S_{i-1} \quad \text{and} \quad \eta_i = 0 \quad \text{in} \quad S \backslash S_i, \\ |\nabla_p \eta_i| \le \frac{\nu+1}{R} \quad \text{and} \quad |\nabla_p^2 \eta_i| \le (\frac{\nu+1}{R})^2. \end{cases} \tag{4.67}$$

Moreover, let $\Omega_i^1 = S_i \times (0,1)$ for $i = 0, \cdots, \nu$ and set

$$\mathbf{y}_i^{(h)} = \bar{\mathbf{F}}\mathbf{z}_p + \eta_i \, (\mathbf{y}^{(h)} - \bar{\mathbf{F}}\mathbf{z}_p).$$

Then, for each i, $\mathbf{y}_i^{(h)}$ converges weakly to $\mathbf{y} = \bar{\mathbf{F}}\mathbf{z}_p$ in $W^{1,p}(\Omega^1, \mathbb{R}^3)$ as h tends to zero and $(\mathbf{y}_i^{(h)} - \bar{\mathbf{F}}\mathbf{z}_p)$ satisfies (4.65). Therefore, it follows from the previous result that

$$\liminf_{h \to 0} e_1^{(h)}[\mathbf{y}_i^{(h)}; \Omega^1] \ge e_1^{(0)}[\mathbf{y}; \Omega^1]. \tag{4.68}$$

Now

$$\begin{aligned} e_1^{(h)}[\mathbf{y}_i^{(h)}; \Omega^1] &= e_1^{(h)}[\mathbf{y}^{(h)}; \Omega_{i-1}^1] + e_1^{(h)}[\mathbf{y}_i^{(h)}; \Omega_i^1 \backslash \Omega_{i-1}^1] + e_1^{(h)}[\mathbf{y}; \Omega^1 \backslash \Omega_i^1] \\ &\le e_1^{(h)}[\mathbf{y}^{(h)}; \Omega^1] + e_1^{(h)}[\mathbf{y}_i^{(h)}; \Omega_i^1 \backslash \Omega_{i-1}^1] + c_2(1 + |\bar{\mathbf{F}}|^p) \, |\Omega^1 \backslash \Omega_0^1|. \end{aligned} \tag{4.69}$$

Using the growth condition (4.8) on φ and the definition of $\eta_i(\mathbf{z}_p)$,

$$\begin{aligned} & e_1^{(h)}[\mathbf{y}_i^{(h)};\Omega_i^1\backslash\Omega_{i-1}^1] \\ \leq C & \int\limits_{\Omega_i^1\backslash\Omega_{i-1}^1} \Big\{\kappa^2\Big(|\nabla_p^2\mathbf{y}^{(h)}|^2+\frac{2}{h^2}|\nabla_p\mathbf{y}_{,3}^{(h)}|^2+\frac{1}{h^4}|\mathbf{y}_{,33}^{(h)}|^2 \\ & +(\frac{\nu+1}{R})^4\,|\mathbf{y}^{(h)}-\bar{\mathbf{F}}\mathbf{z}_p|^2+4(\frac{\nu+1}{R})^2\,|\nabla_p\mathbf{y}^{(h)}-\bar{\mathbf{F}}|^2+\frac{2}{h^2}(\frac{\nu+1}{R})^2|\mathbf{y}_{,3}^{(h)}|^2\Big) \qquad (4.70) \\ & +\Big(1+|\bar{\mathbf{F}}|^p+|\nabla_p\mathbf{y}^{(h)}-\bar{\mathbf{F}}|^p+(\frac{\nu+1}{R})^p|\mathbf{y}^{(h)}-\bar{\mathbf{F}}\mathbf{z}_p|^p+|\frac{1}{h}\mathbf{y}_{,3}^{(h)}|^p\Big)\Big\}\,d\mathbf{z}. \end{aligned}$$

Notice that we have used the inequality $\left(\sum\limits_{i=1}^{N}|a_i|\right)^2 \leq N\sum\limits_{i=1}^{N}|a_i|^2$ in deriving (4.70). Since $\mathbf{y}^{(h)} \overset{h}{\rightharpoonup} \bar{\mathbf{F}}\mathbf{z}_p$ in $W^{1,p}(\Omega^1,I\!R^3)$, this implies $\mathbf{y}^{(h)} \overset{h}{\rightarrow} \bar{\mathbf{F}}\mathbf{z}_p$ in $L^p(\Omega^1;I\!R^3)$ by Rellich's compactness theorem and

$$\int\limits_{\Omega_i^1\backslash\Omega_{i-1}^1} (\frac{\nu+1}{R})^p|\mathbf{y}^{(h)}-\bar{\mathbf{F}}\mathbf{z}_p|^p d\mathbf{z} \to 0 \qquad \text{as } h\to 0. \tag{4.71}$$

By the assumptions of finiteness of $\liminf_{h\to 0} e_1^{(h)}[\mathbf{y}^{(h)}]$ and non-negativity of φ, it is concluded that $\left\|\frac{\kappa}{h}\nabla\mathbf{y}_{,3}^{(h)}\right\|_{L^2(\Omega^1)}$ is uniformly bounded in h. Further since

$$\left|\int\limits_{\Omega^1}\frac{\kappa}{h}\mathbf{y}_{,3}^{(h)}d\mathbf{z}\right| \leq C\kappa\|\frac{1}{h}\mathbf{y}_{,3}^{(h)}\|_{L^p(\Omega^1)}^p,$$

and $\frac{1}{h}\mathbf{y}_{,3}^{(h)}$ is uniformly bounded in $L^p(\Omega^1;I\!R^3)$ due to coercivity of φ, Poincaré inequality implies

$$\frac{\kappa}{h}\mathbf{y}_{,3}^{(h)} \rightharpoonup 0 \quad \text{in } W^{1,2}(\Omega^1;I\!R^3) \qquad \text{as } h\to 0.$$

Similarly, $\|\kappa\nabla^2\mathbf{y}^{(h)}\|_{L^2(\Omega^1)}$ is uniformly bounded in h. Using the Poincaré inequality twice implies that

$$\kappa\mathbf{y}^{(h)} \rightharpoonup 0 \quad \text{in } W^{2,2}(\Omega^1;I\!R^3) \qquad \text{as } h\to 0,$$

from which it is deduced that

$$\int_{\Omega_i^1\backslash\Omega_{i-1}^1} \kappa^2 \left\{ |\mathbf{y}^{(h)} - \bar{\mathbf{F}}\mathbf{z}_p|^2 + |\nabla_p \mathbf{y}^{(h)} - \bar{\mathbf{F}}|^2 + |\frac{1}{h}\mathbf{y}_{,3}^{(h)}|^2 \right\} d\mathbf{z} \to 0, \tag{4.72}$$

as $h \to 0$. Notice that (4.72) is obvious if $p \geq 2$ since $\mathbf{y}^{(h)}$, $\nabla_p \mathbf{y}^{(h)}$ and $\frac{1}{h}\mathbf{y}_{,3}^{(h)}$ is also uniformly bounded in $L^2(\Omega^1)$. Collecting (4.68) to (4.72) gives

$$\begin{aligned} e_1^{(0)}[\mathbf{y}] \leq\ & \liminf_{h\to 0} e_1^{(h)}[\mathbf{y}^{(h)}] + c_2(1 + |\bar{\mathbf{F}}|^p)|\Omega^1\backslash\Omega_0^1| \\ & + C \cdot \int_{\Omega_i^1\backslash\Omega_{i-1}^1} \left\{ \kappa^2 \left(|\nabla_p^2 \mathbf{y}^{(h)}|^2 + \frac{2}{h^2}|\nabla_p \mathbf{y}_{,3}^{(h)}|^2 + \frac{1}{h^4}|\mathbf{y}_{,33}^{(h)}|^2 \right) \right. \\ & \left. + \left(1 + |\bar{\mathbf{F}}|^p + |\nabla_p \mathbf{y}^{(h)} - \bar{\mathbf{F}}|^p + |\frac{1}{h}\mathbf{y}_{,3}^{(h)}|^p \right) \right\} d\mathbf{z}. \end{aligned} \tag{4.73}$$

Summing (4.73) over $i = 1, \cdots, \nu$ and dividing by ν gives

$$\begin{aligned} e_1^{(0)}[\mathbf{y}] \leq\ & \liminf_{h\to 0} e_1^{(h)}[\mathbf{y}^{(h)}] + c_2(1 + |\bar{\mathbf{F}}|^p)|\Omega^1\backslash\Omega_0^1| \\ & + \frac{C}{\nu} \cdot \int_{\Omega^1} \left\{ \kappa^2 \left(|\nabla_p^2 \mathbf{y}^{(h)}|^2 + \frac{2}{h^2}|\nabla_p \mathbf{y}_{,3}^{(h)}|^2 + \frac{1}{h^4}|\mathbf{y}_{,33}^{(h)}|^2 \right) \right. \\ & \left. + \left(1 + |\bar{\mathbf{F}}|^p + |\nabla_p \mathbf{y}^{(h)} - \bar{\mathbf{F}}|^p + |\frac{1}{h}\mathbf{y}_{,3}^{(h)}|^p \right) \right\} d\mathbf{z}. \end{aligned} \tag{4.74}$$

Recalling the assumption of finiteness of $\liminf_{h\to 0} e_1^{(h)}[\mathbf{y}^{(h)}]$ and note that $||\nabla_p \mathbf{y}^{(h)} - \bar{\mathbf{F}}||_{L^p(\Omega^1)}$ and $||\frac{1}{h}\mathbf{y}_{,3}^{(h)}||_{L^p(\Omega^1)}$ are uniformly bounded in h since $\mathbf{y}^{(h)} \rightharpoonup \bar{\mathbf{F}}\mathbf{z}_p$ in $W^{1,p}(\Omega^1, I\!R^3)$ and φ enjoys the coercivity (4.8). This concludes the proof by letting $\nu \to +\infty$ and $\Omega_0^1 \to \Omega^1$.

The proof for the case where $\alpha = 0$ is almost exactly the same except we use

$$\varphi(\bar{\mathbf{F}} + \nabla_p \tilde{\omega}^{(h)} \mid \frac{1}{h}\tilde{\omega}_{,3}, \frac{\mathbf{z}_p}{d}) \geq \varphi_0(\bar{\mathbf{F}} + \nabla_p \tilde{\omega}^{(h)}, \frac{\mathbf{z}_p}{d})$$

after (4.66).

Part B. In the case where $\mathbf{y}$ is the piecewise affine function, the proof for the lower bound is obvious. The recovery sequence can also be constructed by virtue of (4.64).

For general $\mathbf{y} \in V_S$, the existence of recovery sequence can be deduced as follows. The Lipschitz boundary ∂S of the film guarantees the existence of a sequence of piecewise affine functions $\mathbf{y}^{(\delta)}$ such that

$$\mathbf{y}^{(\delta)} \to \mathbf{y} \quad \text{in } W^{1,p}(S, I\!R^3) \qquad \text{as } \delta \to 0. \tag{4.75}$$

For each piecewise affine function $\mathbf{y}^{(\delta)}$, there exists a recovery sequence $\mathbf{y}^{(h,\delta)}$ such that

$$\mathbf{y}^{(h,\delta)} \rightharpoonup \mathbf{y}^{(\delta)} \ \text{ in } W^{1,p}(\Omega^1, I\!R^3) \quad \text{and} \quad e_1^{(h)}[\mathbf{y}^{(h,\delta)}] \to e_1^{(0)}[\mathbf{y}^{(\delta)}] \tag{4.76}$$

as $h \to 0$. Define

$$\begin{aligned} f(h,\delta) &= \left| e_1^{(h)}[\mathbf{y}^{(h,\delta)}] - e_1^{(0)}[\mathbf{y}] \right| + \left\| \mathbf{y}^{(h,\delta)} - \mathbf{y} \right\|_{L^p(\Omega^1)} \\ &\le \left| e_1^{(h)}[\mathbf{y}^{(h,\delta)}] - e_1^{(0)}[\mathbf{y}^{(\delta)}] \right| + \left| e_1^{(0)}[\mathbf{y}^{(\delta)}] - e_1^{(0)}[\mathbf{y}] \right| + \\ &\quad \left\| \mathbf{y}^{(h,\delta)} - \mathbf{y}^{(\delta)} \right\|_{L^p(\Omega^1)} + \left\| \mathbf{y}^{(\delta)} - \mathbf{y} \right\|_{L^p(\Omega^1)}. \end{aligned} \tag{4.77}$$

The Lipschitz condition of (4.52) for the homogenized energy density $\bar{\varphi}$ implies that

$$\left| e_1^{(0)}[\mathbf{y}^{(\delta)}] - e_1^{(0)}[\mathbf{y}] \right| \to 0 \qquad \text{as } \delta \to 0.$$

It follows $\limsup_{\delta \to 0} \limsup_{h \to 0} f(h,\delta) = 0$. A standard diagonalization argument establishes the existence of a recovery sequence.

It remains to prove the lower bound for general $\mathbf{y} \in V_S$. Let $\mathbf{y}^{(h)} \rightharpoonup \mathbf{y}$ in $W^{1,p}(\Omega^1, I\!R^3)$ as $h \to 0$. Without loss of generality, we may assume that $\liminf_{h \to 0} e_1^{(h)}[\mathbf{y}^{(h)}]$ is finite. First, the regularity of ∂S permits the existence of a sequence $\omega^{(h)} \in C^\infty(\bar{S})$ such that

$$\begin{aligned} \omega^{(h)} &\to \mathbf{y} \quad \text{in } W^{1,p}(S, I\!R^3), \\ \kappa \nabla_p^2 \omega^{(h)} &\to 0 \quad \text{in } L^2(S, I\!R^{12}) \end{aligned} \tag{4.78}$$

as $h \to 0$. For any $\delta > 0$, there exists a partition $\{S_i\}$ of S into open sets such that

$$\sum_i \int_{S_i} |\nabla_p \mathbf{y} - \bar{\mathbf{F}}_i|^p d\mathbf{z}_p < \delta \quad \text{with} \quad \bar{\mathbf{F}}_i = \fint_{S_i} \nabla_p \mathbf{y}\, d\mathbf{z}_p. \tag{4.79}$$

Let $\tilde{\mathbf{y}}^{(h)} = \bar{\mathbf{F}}_i \mathbf{z}_p + \mathbf{y}^{(h)} - \omega^{(h)}$ for $\mathbf{z} \in \Omega^1_i = S_i \times (0,1)$. Clearly $\tilde{\mathbf{y}}^{(h)} \rightharpoonup \bar{\mathbf{F}}_i \mathbf{z}_p$ in $W^{1,p}(\Omega^1_i, I\!\!R^3)$ as $h \to 0$. Using the previous result for piecewise affine functions, we have after summation,

$$\liminf_{h\to 0} \sum_i e^{(h)}_1[\tilde{\mathbf{y}}^{(h)}; \Omega^1_i] \geq \sum_i e^{(0)}_1[\bar{\mathbf{F}}_i \mathbf{z}_p; S_i]. \tag{4.80}$$

Notice that from (4.78), we have

$$\begin{gathered} \Big|\, ||\kappa \nabla^2_p \tilde{\mathbf{y}}^{(h)}||_{L^2(\Omega^1_i)} - ||\kappa \nabla^2_p \mathbf{y}^{(h)}||_{L^2(\Omega^1_i)} \,\Big| \leq \\ ||\kappa(\nabla^2_p \tilde{\mathbf{y}}^{(h)} - \nabla^2_p \mathbf{y}^{(h)})||_{L^2(\Omega^1_i)} = ||\kappa \nabla^2_p \omega^{(h)}||_{L^2(\Omega^1_i)} \to 0 \end{gathered} \tag{4.81}$$

as $h \to 0$. Using (4.79), (4.81) and the Lipschitz conditions on φ and $\bar{\varphi}$, we obtain

$$\left| e^{(h)}_1[\mathbf{y}^{(h)}; \Omega^1] - \sum_i e^{(h)}_1[\tilde{\mathbf{y}}^{(h)}; \Omega^1_i] \right| \leq C \cdot \delta^{\frac{1}{p}} \tag{4.82}$$

$$\left| e^{(0)}_1[\mathbf{y}] - \sum_i e^{(0)}_1[\bar{\mathbf{F}}_i \mathbf{z}_p; S_i] \right| \leq C \cdot \delta^{\frac{1}{p}} \tag{4.83}$$

for sufficiently small h. Collecting (4.80), (4.82) and (4.83) concludes the proof. □

4.5 Film Thickness Comparable to Heterogeneity

Theorem 3 *Suppose* $\varphi = \varphi(\mathbf{F}, \frac{\mathbf{z}_p}{d}, z_3)$ *and* $\frac{\kappa}{d} \to \alpha$ *and* $\frac{h}{d} \to \beta > 0$ *as* $h \to 0$. *Let* $\bar{\mathbf{F}} \in I\!\!M^{3\times 2}$ *and* $e^{(h)}_1$ *be defined by (4.11). Then* $e^{(h)}_1$ Γ*-converges to the functional* $e^{(0)}_1$ *defined by (4.16) if*

(i) $\alpha = 0$ *and*

$$\bar{\varphi}(\bar{\mathbf{F}}) = \inf_{k\in I\!N} \inf_{\omega\in\tilde{A}_k^\beta} \fint_{\Omega_k^\beta} \left\{ \varphi(\bar{\mathbf{F}} + \nabla_p\omega \,|\, \omega_{,3}, \mathbf{z}_p, \frac{z_3}{\beta}) \right\} d\mathbf{z}, \tag{4.84}$$

where

$$\Omega_k^\beta = kZ \times (0,\beta), \quad Z = [0,1]^2, \quad \Sigma^\beta = \partial kZ \times (0,\beta), \tag{4.85}$$

$$\tilde{A}_k^\beta = \{\omega : \omega \in W^{1,p}(\Omega_k^\beta, I\!R^3),\ \omega\,|_{\Sigma^\beta} = 0\}; \tag{4.86}$$

(ii) $\alpha > 0$ *and*

$$\bar{\varphi}(\bar{\mathbf{F}}) = \inf_{k\in I\!N} \inf_{\omega\in A_k^\beta} \fint_{\Omega_k^\beta} \left\{ \alpha^2|\nabla^2\omega|^2 + \varphi(\bar{\mathbf{F}} + \nabla_p\omega \,|\, \omega_{,3}, \mathbf{z}_p, \frac{z_3}{\beta}) \right\} d\mathbf{z} \tag{4.87}$$

where

$$A_k^\beta = \{\omega : \omega \in W^{1,p}(\Omega_k^\beta, I\!R^3) \cap W^{2,2}(\Omega_k^\beta, I\!R^3),\ \omega\,|_{\Sigma^\beta} = \frac{\partial\omega}{\partial n}\,|_{\Sigma^\beta} = 0\}; \tag{4.88}$$

(iii) $\alpha = \infty$ *and*

$$\bar{\varphi}(\bar{\mathbf{F}}) = Q\tilde{\varphi}_0(\bar{\mathbf{F}}),$$

$$\tilde{\varphi}_0(\bar{\mathbf{F}}) = \inf_{\mathbf{b}\in I\!R^3} \tilde{\varphi}(\bar{\mathbf{F}}|\mathbf{b}), \qquad \tilde{\varphi}(\mathbf{F}) = \int_{Z\times(0,1)} \varphi(\mathbf{F},\mathbf{z})d\mathbf{z}$$

where $Q\tilde{\varphi}_0$ *is the lower quasi-convex envelope of* $\tilde{\varphi}_0$.

The proof of Theorem 3 for finite $\alpha \geq 0$ is very similar to that of Theorem 2. Indeed, if $\frac{h}{d} = \beta$, the idea to construct the recovery sequence for the affine function $\mathbf{y} = \bar{\mathbf{F}}\mathbf{z}_p$ is to use the following scaling

$$\mathbf{y}^{(h)} = \bar{\mathbf{F}}\mathbf{z}_p + d\omega(\frac{\mathbf{z}_p}{d}, \frac{hz_3}{d}) \tag{4.89}$$

where $\omega(\mathbf{z}) \in A_k^\beta$. The proof of lower bound also follows exactly that of Theorem 2 step by step by using the same scaling (4.89) and we omit here. The case $\alpha = \infty$ is a corollary of Theorem 1.

Theorem 3 also implies the following theorem if the in-plane heterogeneity vanishes.

Theorem 4 *Suppose $\varphi = \varphi(\mathbf{F}, z_3)$ and $\frac{\kappa}{h} \to \alpha'$ as $h \to 0$. Let $\bar{\mathbf{F}} \in I\!M^{3\times 2}$ and $e_1^{(h)}$ be defined by (4.11). Then $e_1^{(h)}$ Γ-converges to the functional $e_1^{(0)}$ defined by (4.16) if*

(i) $\alpha' = 0$ *and*

$$\bar{\varphi}(\bar{\mathbf{F}}) = \inf_{k\in I\!N} \inf_{\omega\in\tilde{A}_k^1} \fint_{\Omega_k^1} \varphi(\bar{\mathbf{F}} + \nabla_p\omega \,|\, \omega_{,3}, z_3) d\mathbf{z} \tag{4.90}$$

where Ω_k^1 and $\tilde{A}_k^1$ are defined by (4.85) and (4.86);

(ii) $\alpha' > 0$ *and*

$$\bar{\varphi}(\bar{\mathbf{F}}) = \inf_{k\in I\!N} \inf_{\omega\in A_k^1} \fint_{\Omega_k^1} \left\{\alpha'^2 \left|\nabla^2\omega\right|^2 + \varphi(\bar{\mathbf{F}} + \nabla_p\omega \,|\, \omega_{,3}, z_3)\right\} d\mathbf{z} \tag{4.91}$$

where Ω_k^1 and A_k^1 are defined by (4.85) and (4.88);

(iii) $\alpha' = \infty$ *and*

$$\bar{\varphi}(\bar{\mathbf{F}}) \;=\; Q\tilde{\varphi}_0(\bar{\mathbf{F}})$$

$$\tilde{\varphi}_0(\bar{\mathbf{F}}) = \inf_{\mathbf{b}\in I\!R^3} \tilde{\varphi}(\bar{\mathbf{F}}|\mathbf{b}) \qquad \tilde{\varphi}(\mathbf{F}) = \int_0^1 \varphi(\mathbf{F}, z_3) dz_3$$

where $Q\tilde{\varphi}_0$ is the lower quasi-convex envelope of $\tilde{\varphi}_0$.

Indeed, for finite $\alpha' \geq 0$, the vanishness of in-plane heterogeneity allows us to set $\beta = 1$ in Theorem 3 and note that $\frac{\kappa}{h} = \frac{\kappa}{d}\frac{d}{h} \to \alpha = \alpha'$ as $h \to 0$. The case $\alpha' = \infty$ is a corollary of Theorem 1.

Remark 5 If our film is homogeneous and the interfacial energy is negligible ($\alpha = \alpha' = 0$), all our results coincide with that of Le Dret and Raoult [29]; i.e., $\bar{\varphi}(\bar{\mathbf{F}}) = Q\varphi_0(\bar{\mathbf{F}})$. This is obvious in Theorem 1 and Theorem 2, but not in Theorem 3 and Theorem 4. So we explain this in some detail. Consider a homogeneous film with energy density $\varphi = \varphi(\mathbf{F})$ and let

$$\varphi_0(\bar{\mathbf{F}}) = \inf_{\mathbf{b} \in I\!R^3} \varphi(\bar{\mathbf{F}}|\mathbf{b}).$$

Assume φ enjoys the growth and coercivity conditions (4.8). Clearly, φ_0 also has such a property. Hence, $W^{1,p}$ quasi-convexification is equal to $W^{1,\infty}$ quasi-convexification and $Q\varphi_0$ can be expressed as

$$Q\varphi_0(\bar{\mathbf{F}}) = \inf_{\hat{\omega} \in W_0^{1,p}(Z)} \fint_Z \varphi_0(\bar{\mathbf{F}} + \nabla_p \hat{\omega}) d\mathbf{z}_p. \tag{4.92}$$

On the other hand, for homogeneous film, $\bar{\varphi}$ defined in (4.84) becomes

$$\bar{\varphi}(\bar{\mathbf{F}}) \quad = \quad \inf_{k \in I\!N} \inf_{\omega \in \bar{A}_k^\beta} \fint_{\Omega_k^\beta} \varphi(\bar{\mathbf{F}} + \nabla_p \omega \,|\, \omega_{,3}) d\mathbf{z} \tag{4.93}$$

for any finite $\beta > 0$. We wish to show $\bar{\varphi} = Q\varphi_0$.

First, it is clear that

$$\bar{\varphi}(\bar{\mathbf{F}}) \geq Q\varphi_0(\bar{\mathbf{F}}).$$

To prove the reverse inequality, notice that there exists sequences of $\hat{\omega}^\delta \in W_0^{1,p}(Z, I\!R^3)$ and $\mathbf{b}^\delta \in L^p(Z, I\!R^3)$ such that

$$\fint_Z \varphi_0(\bar{\mathbf{F}} + \nabla_p \hat{\omega}^\delta) d\mathbf{z}_p \quad = \quad \fint_Z \varphi(\bar{\mathbf{F}} + \nabla_p \hat{\omega}^\delta | \mathbf{b}^\delta) d\mathbf{z}_p \to Q\varphi_0(\bar{\mathbf{F}}) \tag{4.94}$$

as $\delta \to 0$. Since $C_0^\infty(Z, I\!R^3)$ is dense in $L^p(Z, I\!R^3)$, we may assume $\mathbf{b}^\delta \in C_0^\infty(Z, I\!R^3)$

(see Remark 3). Let $k \in I\!N$ and $h = \frac{1}{k}$ and define

$$\mathbf{y}^{(h,\delta)} = \bar{\mathbf{F}}\mathbf{z}_p + \frac{1}{h}\hat{\omega}^\delta(h\mathbf{z}_p) + \mathbf{b}^\delta(h\mathbf{z}_p)z_3. \tag{4.95}$$

It is clear that $(\mathbf{y}^{(h,\delta)} - \bar{\mathbf{F}}\mathbf{z}_p) \in \tilde{A}_k^\beta$ defined by (4.86). Therefore,

$$\bar{\varphi}(\bar{\mathbf{F}}) \leq \fint_{\Omega_k^\beta} \varphi(\nabla \mathbf{y}^{(h,\delta)})d\mathbf{z} \tag{4.96}$$

for any $h = \frac{1}{k}, k \in I\!N$ and $\delta > 0$. Notice that by changing variable $\hat{\mathbf{z}}_p = h\mathbf{z}_p$ and $\hat{z}_3 = z_3$, (4.96) becomes

$$\bar{\varphi}(\bar{\mathbf{F}}) \leq \frac{1}{\beta}\int_0^\beta \int_Z \varphi(\bar{\mathbf{F}} + \nabla_p\hat{\omega}^\delta(\hat{\mathbf{z}}_p) + h\nabla_p\mathbf{b}^\delta(\hat{\mathbf{z}}_p)\hat{z}_3|\mathbf{b}^\delta(\hat{\mathbf{z}}_p))d\hat{\mathbf{z}}_p d\hat{z}_3. \tag{4.97}$$

Let $h \to 0$, and then $\delta \to 0$ in (4.97), we have

$$\bar{\varphi}(\bar{\mathbf{F}}) \leq Q\varphi_0(\bar{\mathbf{F}}).$$

□

Remark 6 If the film does not contain any out-of-plane heterogeneity; i.e., $\varphi = \varphi(\mathbf{F}, \frac{\mathbf{z}_p}{d})$, then Theorem 1(i) and Theorem 2(i) imply that the ratio $\frac{\kappa}{h}$ is irrelevant to the effective energy. In particular, the effective energy of a homogeneous film is independent of the ratio $\frac{\kappa}{h}$. This ratio $\frac{\kappa}{h}$ is important only if the film contains out-of-plane heterogeneity such as Theorem 4. We provide an example to explain this. Let $S = (0, L), \Omega^1 = S \times (0, 1)$, and $\mathbf{y} : \Omega^1 \to I\!R^2$ be the deformation. The energy per unit thickness for this homogeneous thin film is

$$e_1^{(h)}[\mathbf{y}] = \int_{\Omega^1} \left\{ \kappa^2 \left(|\mathbf{y}_{,11}|^2 + \frac{2}{h^2}|\mathbf{y}_{,12}|^2 + \frac{1}{h^4}|\mathbf{y}_{,22}|^2 \right) + \varphi(\mathbf{y}_{,1}|\frac{1}{h}\mathbf{y}_{,2}) \right\} d\mathbf{z} \tag{4.98}$$

and the effective energy as $h \to 0$ is

$$e_1^{(0)}[\mathbf{y}] = \int_S Q\varphi_0 \left(\frac{\partial \mathbf{y}}{\partial z_1}\right) dz_1.$$

Notice that the effective energy density $\bar{\varphi}$ is independent of the ratio $\frac{\kappa}{h}$. Let us now specialize to the material with local energy density $\varphi^{(1)}(\mathbf{F}) : I\!M^{2\times 2} \to I\!R$ of the form

$$\varphi^{(1)}(\mathbf{F}) \;=\; \frac{1}{2}\left\{(F_{11}-1)^2 + (F_{21}^2-1)^2 + F_{12}^2 + (F_{22}-1)^2\right\}.$$

The minimizers for $\varphi^{(1)}$ are

$$\mathbf{F}_1^{(1)} = \begin{pmatrix} 1 & 0 \\ 1 & 1 \end{pmatrix}, \; \mathbf{F}_2^{(1)} = \begin{pmatrix} 1 & 0 \\ -1 & 1 \end{pmatrix}. \tag{4.99}$$

Suppose the edge of this thin film is clamped and set $\bar{\mathbf{F}} = (1,0)^T$. We now show that $\bar{\varphi}(\bar{\mathbf{F}}) = 0$. First consider the case $\kappa = 0$. Then, at each $h > 0$, the sequence shown schematically in Figure 4.1(a) is clearly a minimizing sequence for $e_1^{(h)}[\mathbf{y}]$ and it follows that $\bar{\varphi}(\bar{\mathbf{F}}) = 0$. If $\kappa \neq 0$ but is small; i.e., $\alpha' = \frac{\kappa}{h} \xrightarrow{h} 0$, a slight refinement establishes the same result. On the other hand, if $\alpha' > 0$, it is not clear whether Figure 4.1(a) minimizes $e_1^{(h)}[\mathbf{y}]$ as it contains too much interfacial energy. We now show that the sequence in Figure 4.1(a) minimizes the energy even if $\alpha' > 0$. Indeed, set

$$f(z_1) = \begin{cases} z_1 & \text{for } 0 \le z_1 \le \frac{1}{2}, \\ -z_1 + \frac{1}{2} & \text{for } \frac{1}{2} \le z_1 \le 1. \end{cases}$$

Let $\chi^{(m)} \in C_0^\infty([0,1])$ converges strongly to f in $W_0^{1,4}([0,1])$ as $m \to \infty$. For each fixed m, extend $\chi^{(m)}$ periodically to $I\!R$ and consider

$$y_1^{(1,h,m)} = z_1, \quad y_2^{(1,h,m)} = d\,\chi^{(m)}(\frac{z_1}{d}) + h\,z_2, \tag{4.100}$$

where $\frac{1}{d(h)}$ is chosen to be the largest integer such that $\frac{1}{d(h)} \le \frac{1}{\sqrt{\kappa(h)}}$. Substituting

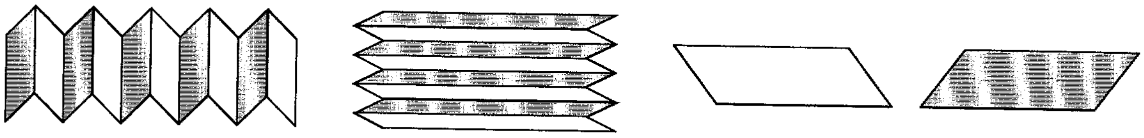

(a) **(b)** **(c)**

Figure 4.1: (a) The sequence that minimizes the energy with density $\varphi^{(1)}$ for $\alpha' \geq 0$. Here the darkly shaded and white regions represent $\mathbf{F}_1^{(1)}$ and $\mathbf{F}_2^{(1)}$ defined by (4.99), respectively. (b) The sequence that minimizes the energy with density $\varphi^{(2)}$ only for $\alpha' = 0$. Here the darkly shaded and white regions represent $\mathbf{F}_1^{(2)}$ and $\mathbf{F}_2^{(2)}$ defined by (4.101), respectively. (c) The sequence that minimizes the energy with density $\varphi^{(2)}$ for $\alpha' \geq 0$. Here the darkly shaded and white regions represent $\mathbf{F}_1^{(2)}$ and $\mathbf{F}_2^{(2)}$ defined by (4.101), respectively.

(4.100) into (4.98), we find the energy is driven to zero if $h \to 0$ first and $m \to \infty$ next. By standard diagonalization process, we obtain (4.100) is the minimizing sequence for (4.98).

Next consider another material with the local energy density $\varphi^{(2)}(\mathbf{F}) : I\!M^{2\times 2} \to I\!R$ of the form

$$\varphi^{(2)}(\mathbf{F}) \;=\; \frac{1}{2}\left\{(F_{11}-1)^2 + F_{21}^2 + (F_{12}^2-1)^2 + (F_{22}-1)^2\right\}.$$

The minimizers for $\varphi^{(2)}$ are

$$\mathbf{F}_1^{(2)} = \begin{pmatrix} 1 & 1 \\ 0 & 1 \end{pmatrix}, \quad \mathbf{F}_2^{(2)} = \begin{pmatrix} 1 & -1 \\ 0 & 1 \end{pmatrix}. \tag{4.101}$$

Now if the edge of the film is clamped and if $\kappa = 0$ or $\alpha' = 0$, Figure 4.1(b) is clearly one sequence minimizing the energy of this strip. On the other hand, if $\alpha' > 0$, it can be shown that the sequence in Figure 4.1(b) does not minimize the energy. Instead, the sequence that minimizes the energy in this case looks like that in Figure 4.1(c). Indeed, set $g(z_1) = 1$ and let $\eta^{(m)} \in C_0^\infty([0,1])$ converge strongly to g in $W_0^{1,4}([0,1])$. Consider

$$y_1^{(2,h,m)} = z_1 \pm h\eta^{(m)}(z_1)z_2, \quad y_2^{(2,h,m)} = h\, z_2. \tag{4.102}$$

Using an argument similar to the above, we can show that (4.102) is the minimizing sequence for (4.98).

In summary, material can form microstructure freely with interfaces which are perpendicular to the film (Figure 4.1(a)) and such interfaces cost vanishing energy as $h \to 0$ independent of $\frac{\kappa}{h}$. Further, material does not need to form the out-of-plane fine-scale microstructure to reduce the energy (Figure 4.1(c)) as long as there is no out-of-plane heterogeneity contained in the film.

4.6 Film Thickness Much Larger than Heterogeneity

Let us consider the case $\kappa = 0$, $\varphi = \varphi(\mathbf{F}, \frac{\mathbf{z}_p}{d})$ and the following change of variables

$$\begin{aligned} \hat{\mathbf{z}}_p = \frac{\mathbf{z}_p}{h}, &\qquad \hat{z}_3 = z_3, \\ h\hat{\mathbf{y}}(\hat{\mathbf{z}}_p, \hat{z}_3) &= \mathbf{y}(h\hat{\mathbf{z}}_p, \hat{z}_3). \end{aligned}$$

Then, $e_1^{(h)}$ becomes

$$h^2 \int_0^1 \int_{\frac{S}{h}} \varphi(\nabla\hat{\mathbf{y}}, \frac{\hat{\mathbf{z}}_p}{\frac{d}{h}}) d\hat{\mathbf{z}}_p d\hat{z}_3. \tag{4.103}$$

Since $\frac{h}{d} \to \infty$ as $h \to 0$, (4.103) suggests that $\bar{\varphi}$ is obtained by homogenizing in the plane of the film first and then passing to the thin-film limit, or

$$\begin{aligned} \bar{\varphi}(\bar{\mathbf{F}}) &= Q\varphi_0^H(\bar{\mathbf{F}}), \\ \varphi_0^H(\bar{\mathbf{F}}) &= \inf_{\mathbf{b}\in I\!R^3} \varphi^H(\bar{\mathbf{F}}|\mathbf{b}), \\ \varphi^H(\mathbf{F}) &= \inf_{k\in I\!N} \inf_{\omega\in W_0^{1,p}(k\hat{Z})} \fint_{k\hat{Z}} \varphi(\mathbf{F} + \nabla\omega, \mathbf{z}_p) d\mathbf{z} \end{aligned} \tag{4.104}$$

where $Q\varphi_0^H(\bar{\mathbf{F}})$ is the lower quasi-convex envelope of φ_0^H, $\hat{Z} = [0,1]^3$ and $\mathbf{F} = (\bar{\mathbf{F}}|\mathbf{b})$. Notice that φ^H is the homogenized energy density of bulk cellular elastic materials [67]. This conjecture has recently been proved by Braides and Fonseca [14] and involves difficulties similar to those associated with reiterated homogenization for nonconvex energies (see [16, 68]).

Next, consider the case $\varphi = \varphi(\mathbf{F}, \frac{\mathbf{z}_p}{d})$, $\kappa \neq 0$ and $\frac{\kappa}{d} \to \alpha < \infty$ as $h \to 0$. Using the same change of variables above gives

$$h^2 \int_0^1 \int_{\frac{S}{h}} \left\{ \alpha^2 (\frac{d}{h})^2 \,|\, \nabla^2 \hat{\mathbf{y}} \,|^2 + \varphi(\nabla \hat{\mathbf{y}}, \frac{\hat{\mathbf{z}}_p}{\frac{d}{h}}) \right\} d\hat{\mathbf{z}}_p d\hat{z}_3. \tag{4.105}$$

Comparing (4.105) with equation (2.4) and $\gamma = 1$ in [37] suggests that $\bar{\varphi}$ is obtained by averaging and homogenizing in the plane of the film first, and then passing to the thin-film limit, or

$$\begin{aligned} \bar{\varphi}(\bar{\mathbf{F}}) &= Q\varphi_0^{AH}(\bar{\mathbf{F}}), \\ \varphi_0^{AH}(\bar{\mathbf{F}}) &= \inf_{\mathbf{b} \in I\!R^3} \varphi^{AH}(\bar{\mathbf{F}}|\mathbf{b}), \\ \varphi^{AH}(\mathbf{F}) &= \inf_{k \in I\!N} \inf_{\omega \in W_0^{1,p}(k\hat{Z}) \cap W_0^{2,2}(k\hat{Z})} \int\!\!\!\!\!\!-_{k\hat{Z}} \left\{ \alpha^2 |\, \nabla^2 \omega \,|^2 + \varphi(\mathbf{F} + \nabla \omega, \mathbf{z}_p) \right\} dz. \end{aligned} \tag{4.106}$$

We conjecture that (4.106) can be confirmed by following the approach similar to that of Braides and Fonseca [14].

Finally, our Theorem 1(i) includes the case $\frac{\kappa}{d} \to \alpha = \infty$ as $h \to 0$.

4.7 Recoverable Strain in Polycrystalline Thin Films

4.7.1 Model Example

We consider a two-dimensional model problem where the deformation $\mathbf{y}$ is replaced by a scalar-valued function $\eta : I\!R^2 \to I\!R$. We assume that the film is polycrystalline with columnar grains. Let $\mathbf{R} : I\!R \to SO(2)$ describe the texture of our polycrystal film. We assume $\mathbf{R}(z_1)$ is periodic with period $[0, 1]$. The microscopic energy density has the form

$$\varphi(\mathbf{f}, \frac{z_1}{d}) = \varphi(\mathbf{R}^T(\frac{z_1}{d})\mathbf{f}).$$

The total energy of the film per unit thickness is

$$e_1^{(h)}[\eta] = \int_{\Omega^1} \left\{ \kappa^2 \left(\left| \frac{\partial^2 \eta}{\partial z_1^2} \right|^2 + \frac{2}{h^2} \left| \frac{\partial \eta}{\partial z_1} \frac{\partial \eta}{\partial z_2} \right|^2 + \frac{1}{h^4} \left| \frac{\partial^2 \eta}{\partial z_2^2} \right|^2 \right) + \varphi(\frac{\partial \eta}{\partial z_1} | \frac{1}{h} \frac{\partial \eta}{\partial z_2}, \frac{z_1}{d}) \right\} d\mathbf{z} \quad (4.107)$$

where $S = (0, L)$ is the one-dimensional film and $\Omega^1 = S \times (0, 1)$. The limiting energy per unit thickness is

$$e_1^{(0)}[\eta] = \int_S \bar{\varphi}(\frac{\partial \eta}{\partial z_1}) dz_1. \quad (4.108)$$

Assume the film thickness is comparable to the grain size and the interfacial energy is negligible; i.e., $\frac{h}{d} \to \beta > 0$ and $\frac{\kappa}{d} \to 0$ as $h \to 0$. It follows from (4.84) that $e_1^{(h)}$ Γ-converges to the functional $e_1^{(0)}$ if the effective energy density $\bar{\varphi}(\xi)$ of the film is given by

$$\bar{\varphi}(\xi) = \inf_{k \in \mathbb{N}} \inf_{\omega \in \hat{A}_k^\beta} \fint_{\Omega_k^\beta} \left\{ \varphi \left(\mathbf{R}^T(z_1)(\xi + \frac{\partial \omega}{\partial z_1} | \frac{\partial \omega}{\partial z_2}) \right) \right\} d\mathbf{z} \quad (4.109)$$

where

$$\begin{aligned} \Omega_k^\beta &= kZ \times (0, \beta), \quad Z = [0, 1], \\ \hat{A}_k^\beta &= \{\omega : \omega \in \hat{W}_{\text{per}}^{1,p}(\Omega_k^\beta, \mathbb{R})\} \end{aligned}$$

where elements of $\hat{W}_{\text{per}}^{1,p}(\Omega_k^\beta, \mathbb{R})$ are periodic only in z_1 with period kZ. Notice that we have replaced $\tilde{A}_k^\beta$ in (4.86) by $\hat{A}_k^\beta$; a slight refinement of the argument of Müller [67] shows we can minimize (4.109) over either of these two spaces.

Let $\hat{\varphi}$ be the *relaxation* of φ and consider the analogue of (4.109)

$$\inf_{k\in I\!N}\inf_{\omega\in\hat{A}_k^\beta}\fint_{\Omega_k^\beta}\left\{\hat{\varphi}\left(\mathbf{R}^T(z_1)(\xi+\frac{\partial\omega}{\partial z_1}|\frac{\partial\omega}{\partial z_2})\right)\right\}d\mathbf{z} \tag{4.110}$$

These two expressions (4.109) and (4.110) are in some sense equivalent since the minimizing sequences for the former converge weakly to the minimizers of the latter, and the minimizers of the latter give rise to minimizing sequences for the former [2]. Therefore, from now on, we won't distinguish between minimizing sequences and minimizers and use $\hat{\varphi}$ in (4.110) to replace φ in (4.109). Further, in our particular problem below, $\hat{\varphi}$ is convex and it suffices to take $k = 1$; however, we do not use it since we consider bounds.

We state a useful lower bound for $\bar{\varphi}$. Let

$$\psi^*(\mathbf{g}) = \max_{\mathbf{f}}\{\mathbf{f}\cdot\mathbf{g} - \psi(\mathbf{f})\}$$

be the Fenchel transformation of the function ψ. Let $\omega \in \hat{A}_k^\beta$ and consider any vector field $\mathbf{g} = (g_1, g_2)^T$ which is periodic in z_1 with period $Z = [0,1]$. If we assume $\nabla\cdot\mathbf{g} = 0$ in Ω_1^β and $\mathbf{g}\cdot\mathbf{n} = 0$ at $z_2 = 0$ and β where $\mathbf{n} = (0,1)^T$ is the outward normal, it follows that

$$\fint_{\Omega_k^\beta}\hat{\varphi}(\mathbf{R}^T(f_1+\omega_{,1}|\omega_{,2}))d\mathbf{z} \geq \fint_{\Omega_k^\beta}\{f_1g_1 - \hat{\varphi}^*(\mathbf{R}^T\mathbf{g})\}d\mathbf{z} = \fint_{\Omega_1^\beta}\{f_1g_1 - \hat{\varphi}^*(\mathbf{R}^T\mathbf{g})\}d\mathbf{z}.$$

Optimization over ω, k and $\mathbf{g}$ gives

$$\bar{\varphi}(f_1) \geq \max_{\substack{\nabla\cdot\mathbf{g}=0\\ \mathbf{g}\cdot\mathbf{n}=0\,\text{on}\,z_2=0,\,\beta}}\fint_{\Omega_1^\beta}\left\{f_1g_1 - \hat{\varphi}^*\left(\mathbf{R}^T(z_1)\mathbf{g}(\mathbf{z})\right)\right\}d\mathbf{z} \tag{4.111}$$

where $\mathbf{g}$ is periodic in z_1 with period $[0,1]$.

We now specialize to a two-variant material with microscopic elastic energy

$$\varphi(\mathbf{f}) = \min\left\{\frac{1}{2}\left((f_1-1)^2+f_2^2\right), \frac{1}{2}\left((f_1+1)^2+f_2^2\right)\right\} \tag{4.112}$$

where $\mathbf{f} = (f_1, f_2)^T$. It can be shown that, in this case,

$$\hat{\varphi}(\mathbf{f}) = \frac{1}{2}\left\{(|f_1|-1)_+^2 + f_2^2\right\} \tag{4.113}$$

with the convention that $a_+ = \max\{a, 0\}$ and

$$\hat{\varphi}^*(\mathbf{f}) = \frac{1}{2}|\mathbf{f}|^2 + |f_1|. \tag{4.114}$$

Our main interest is to study the shape-memory behavior or stress-free configuration of the film. In other words, we want to determine the "set of recoverable strains for the polycrystalline thin film" which we define as

$$\mathcal{P} = \{\xi : \bar{\varphi}(\xi) = 0\}.$$

A single crystal is the special case of the polycrystal. In that case, clearly, $\mathcal{P}$ contains a line segment $[-1, 1]$. But for films with general texture, $\mathcal{P}$ is expected to be smaller than this line segment. The extent of this reduction of recoverable strains in thin films also depends on the parameter β and our task is to determine it. We do so in detail for the special polycrystal as shown in Figure 4.2(a).

Proposition 1 *Consider the polycrystal with the texture*

$$\mathbf{R}(z_1) = \begin{cases} \mathbf{R}_1 & m \le z_1 < m + \frac{1}{2} \quad (\textit{“grain 1”}), \\ \mathbf{R}_2 & m - \frac{1}{2} \le z_1 < m \quad (\textit{“grain 2”}), \end{cases}$$

where $m \in \mathbb{Z}$ *and*

$$\mathbf{R}_1 = \begin{pmatrix} \cos\theta & -\sin\theta \\ \sin\theta & \cos\theta \end{pmatrix} \quad \textit{and} \quad \mathbf{R}_2 = \begin{pmatrix} \cos\theta & \sin\theta \\ -\sin\theta & \cos\theta \end{pmatrix}$$

in the "grey" and "white" rectangles of Figure 4.2(a) for $0 < \theta < \frac{\pi}{2}$. *If* $\beta \leq \frac{1}{2}\cot\theta$, *then*

$$\mathcal{P} = \{\xi : |\xi| \leq \cos\theta - 2\beta\sin\theta\}; \tag{4.115}$$

if $\beta = \frac{1}{2}\cot\theta$, *then there exist positive constants* c *and* C *such that*

$$c|\xi|^3 \leq \bar{\varphi}(\xi) \leq C|\xi|^3 \quad \text{for } \xi \text{ sufficiently small} \tag{4.116}$$

and clearly $\mathcal{P} = \{0\}$; *finally, if* $\beta > \frac{1}{2}\cot\theta$, *then there exists a constant* $C > 0$ *such that*

$$\bar{\varphi}(\xi) \geq C|\xi|^2 \tag{4.117}$$

and once again $\mathcal{P} = \{0\}$.

Proof. Consider the case $\beta \leq \frac{1}{2}\cot\theta$ first. The test field η can be constructed using the idea proposed by Bhattacharya and Kohn [12] for bulk polycrystals. Indeed, in order to get the zero energy, the test field must have the property that $\mathbf{R}^T\nabla\eta$ should be parallel to $\mathbf{e}_1$ a.e. and $|\nabla\eta| \leq 1$. This motivates the following construction:

$$\nabla\eta = \begin{cases} a(\cos\theta, \sin\theta)^T & \text{in the darkly shaded region of "grain 1,"} \\ a(\cos\theta, -\sin\theta)^T & \text{in the darkly shaded region of "grain 2,"} \\ 0 & \text{otherwise,} \end{cases} \tag{4.118}$$

as shown in Figure 4.2(b) for some $|a| \leq 1$. This test field is compatible since $\nabla\eta$ is piecewise constant, and on every interface $[[\nabla\eta]] \cdot \hat{\mathbf{t}} = 0$ where $[[\ ]]$ denotes the jump across the interface and $\hat{\mathbf{t}}$ is the tangent. Further the area of support of $\nabla\eta$ is greater than zero since $\beta \leq \frac{1}{2}\cot\theta$. The average $⨍\,\nabla\eta = a(\cos\theta - 2\beta\sin\theta)\mathbf{e}_1$ and hence we obtain a lower bound of

$$\mathcal{P} \supset \{\xi : |\xi| \leq \cos\theta - 2\beta\sin\theta\}.$$

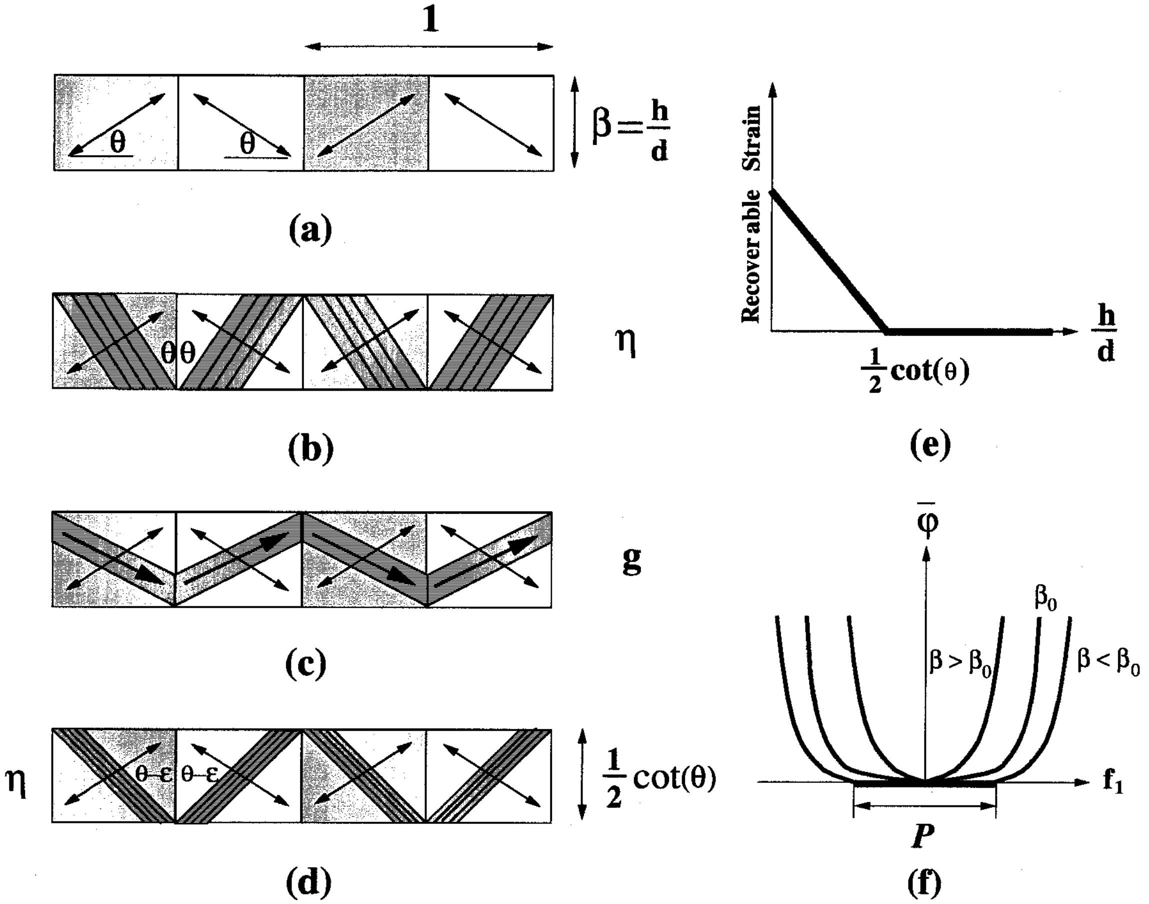

Figure 4.2: (a) A polycrystalline thin film with the texture containing two orientations. (b) The test field $\nabla\eta$. The darkly shaded regions form the support of $\nabla\eta$ and the straight lines within them are level sets of η. (c) The test divergence-free flow $\mathbf{g}$. The darkly shaded strips form the support of $\mathbf{g}$ and the arrows within them point out the direction of the flow. (d) The test field $\nabla\eta$ when $\beta = \beta_0 = \frac{1}{2}\cot\theta$. The darkly shaded regions form the support of $\nabla\eta$ and the straight lines within them are level sets of η. (e) The recoverable strain $(= \frac{1}{2}|\mathcal{P}|)$ versus different values β. (f) The behavior of $\bar{\varphi}(\xi)$ for ξ near zero with different values β. Notice that $\bar{\varphi}(\xi)$ grows quadratically if $\beta > \beta_0$, becomes flat (zero) if $\beta < \beta_0$, and has an exact cubic growth near the origin if $\beta = \beta_0$.

Next we show that $\mathcal{P}$ contains no other points. Indeed, this is equivalent to showing that $\bar{\varphi}(\xi) > 0$ if $|\xi| > \cos\theta - 2\beta\sin\theta$. We can accomplish this using the lower bound (4.111). Consider the dark strips shown in Figure 4.2(c). Taking the slopes of these strips as $\pm(\beta-\mu)/(\frac{1}{2}+\mu)$ where $\mu > 0$, set

$$\mathbf{g} = \begin{cases} (\frac{1}{2}+\mu, \mu-\beta)^T & \text{in the darkly shaded strip of ``grain 1,''} \\ (\frac{1}{2}+\mu, \beta-\mu)^T & \text{in the darkly shaded strip of ``grain 2,''} \\ 0 & \text{otherwise.} \end{cases} \tag{4.119}$$

It is easy to verify that $\nabla\cdot\mathbf{g} = 0$ and $\mathbf{g}\cdot\mathbf{n} = 0$ at $z_2 = 0$ and β. Substituting the test field $\tau\mathbf{g}$ into (4.111) and using the formula (4.114) for $\hat{\varphi}^*$, we obtain

$$\begin{aligned} \bar{\varphi}(f_1) &\geq \tau \int\!\!\!\!\!\!- f_1 g_1 - \frac{\tau^2}{2}\int\!\!\!\!\!\!- |\mathbf{g}|^2 - |\tau|\int\!\!\!\!\!\!- |\mathbf{e}_1\cdot\mathbf{R}^T(z_1)\mathbf{g}| \\ &= \frac{A}{2}\{-[(\frac{1}{2}+\mu)^2 + (\mu-\beta)^2]\tau^2 + (1+2\mu)f_1\tau \\ &\quad - [(\cos\theta - 2\beta\sin\theta) + 2\mu c_0]|\tau|\} \end{aligned} \tag{4.120}$$

where $A = \frac{\mu(1+2\beta)}{\beta(1+2\mu)}$ is the area fraction of the strips and $c_0 = \sin\theta + \cos\theta$. To get the optimal lower bound we maximize (4.120) over τ. Clearly, $\bar{\varphi}(f_1) > 0$ if

$$(1+2\mu)|f_1| - [(\cos\theta - 2\beta\sin\theta) + 2\mu c_0] > 0.$$

Notice that if $|f_1| > (\cos\theta - 2\beta\sin\theta)$, then the above inequality holds for sufficiently small μ; and hence $f_1 \notin \mathcal{P}$. This proves (4.115).

We now turn to the case $\beta > \frac{1}{2}\cot\theta$. We obtain the desire lower bound from (4.111) by using the same test field $\tau\mathbf{g}$ as above with

$$\mu = \frac{2\beta\sin\theta - \cos\theta}{2(\sin\theta + \cos\theta)} > 0. \tag{4.121}$$

Then (4.120) gives

$$\bar{\varphi}(f_1) \geq \frac{A}{2}\left\{-[(\frac{1}{2}+\mu)^2 + (\mu-\beta)^2]\tau^2 + (1+2\mu)f_1\tau\right\}. \tag{4.122}$$

Maximizing over τ, we conclude that for some $C > 0$ independent of f_1,

$$\bar{\varphi}(f_1) \geq C f_1^2.$$

Finally, we come to the case $\beta = \frac{1}{2}\cot\theta$. We start with the lower bound first. Using the divergence-free field $\tau\mathbf{g}$ in (4.119) and substituting it into (4.111), we have

$$\bar{\varphi}(f_1) \geq \frac{A}{2}\left\{-[(\frac{1}{2}+\mu)^2 + (\mu-\beta)^2]\tau^2 + (1+2\mu)f_1\tau - 2\mu c_0|\tau|\right\} \tag{4.123}$$

where $c_0 = \sin\theta + \cos\theta$. This bound is positive if $(1+2\mu)|f_1| > 2\mu c_0$ or

$$\mu < \frac{|f_1|}{2(c_0 - |f_1|)}$$

Now maximizing (4.123) with respect to τ and choosing $\mu = a|f_1|$ with $a < \frac{1}{2c_0}$, we have for some $c > 0$

$$\begin{aligned} \bar{\varphi}(f_1) &\geq \frac{\mu(1+2\beta)}{2\beta(1+2\mu)}\left(\frac{(|f_1| + 2\mu(|f_1| - c_0))^2}{4[(\frac{1}{2}+\mu)^2 + (\mu-\beta)^2]}\right) \\ &= c|f_1|^3 + O(f_1)^4 \quad \text{for } f_1 \text{ near } 0. \end{aligned}$$

Next we return to the upper bound. Pick $\varepsilon > 0$ such that $\theta - \varepsilon > 0$ and construct a field η as shown in Figure 4.2(d):

$$\nabla\eta = \begin{cases} \frac{1}{\cos\varepsilon}(\cos(\theta-\varepsilon), \sin(\theta-\varepsilon))^T & \text{in the darkly shaded region of “grain 1,”} \\ \frac{1}{\cos\varepsilon}(\cos(\theta-\varepsilon), -\sin(\theta-\varepsilon))^T & \text{in the darkly shaded region of “grain 2,”} \\ 0 & \text{otherwise.} \end{cases}$$

By geometry, the area fraction of these darkly shaded strips is

$$A = 1 - 2\beta\tan(\theta-\varepsilon) = \frac{\sin\varepsilon}{\sin\theta\cos(\theta-\varepsilon)}$$

since $\cos\theta = 2\beta\sin\theta$. It follows that

$$f_1 = \fint \nabla\eta = \frac{1}{\cos\varepsilon}\left(\cos(\theta-\varepsilon) - 2\beta\sin(\theta-\varepsilon)\right) = \frac{\tan\varepsilon}{\sin\theta}.$$

The local energy is

$$\hat{\varphi}(\mathbf{R}^T(z_1)\nabla\eta) = \frac{1}{2}\tan^2\varepsilon$$

whenever $\nabla\eta \neq 0$. Therefore, this test field gives an upper bound

$$\begin{aligned}
\bar{\varphi}(f_1) &\leq \frac{1}{2}\left(\frac{\sin\varepsilon}{\sin\theta\cos(\theta-\varepsilon)}\right)\tan^2\varepsilon \\
&\leq \frac{\sin^2\theta}{2\cos(\theta-\varepsilon)\sqrt{1+\sin^2\theta\, f_1^2}}\, f_1^3 \\
&\leq \frac{\sin^2\theta}{2\cos\theta}\, f_1^3.
\end{aligned}$$

□

This example shows the effect of β (film thickness over the size of heterogeneity) on the shape-memory behavior quite dramatically. The recoverable strain $\frac{1}{2}|\mathcal{P}|$ versus β is shown in Figure 4.2(e). Further, the growth of $\bar{\varphi}(\xi)$ as it departs from $\mathcal{P}$ also significantly depends on the ratio β. As shown in Figure 4.2(f), there exists a point $\beta_0 = \frac{1}{2}\cot\theta$ such that for $\beta > \beta_0$, $\bar{\varphi}(\xi)$ grows quadratically and for $\beta < \beta_0$, $\bar{\varphi}(\xi)$ is flat (zero) and for $\beta = \beta_0$, $\bar{\varphi}(\xi)$ has a cubic growth for ξ near the origin.

In this example we only deal with a simple texture with two orientations. But we can generalize our method to a texture with N orientations within the cell. The exact set of recoverable strains and the behavior of $\bar{\varphi}(\xi)$ for ξ near the origin can also be predicted similarly. However, our current analysis is texture-dependent and it would be very useful to develop texture-independent bounds to explore the full range of behavior of a film. Bhattacharya and Kohn [12] have used the translation method to predict the shape-memory behavior for bulk materials. Unfortunately, it does not work here. For example, consider the following identity which plays a central role in their analysis. If $\eta = \mathbf{f} \cdot \mathbf{z}$ and $\zeta = \mathbf{g} \cdot \mathbf{z}$ at $\partial \Omega_k^\beta$, then

$$\fint \det(\nabla \eta, \nabla \zeta) = \det(\mathbf{f}, \mathbf{g}). \tag{4.124}$$

Unfortunately (4.124) does not necessarily hold if we only knew η and ζ on part of the boundary $\partial kZ \times (0, \beta)$ rather than an entire boundary $\partial \Omega_k^\beta$. Notice that the test field ω in the definition of variational principle (4.109) is periodic only in z_1 and does not satisfy any boundary condition on the top and bottom parts of the film. This lack of information prevents an identity like (4.124) and we can not use their method. Similarly, in the lower bound (4.111), the divergence-free flow $\mathbf{g}$ must meet an additional requirement $\mathbf{g} \cdot \mathbf{n} = 0$ on the top and bottom parts of the film. This adds another difficulty in developing useful bounds.

4.7.2 Martensitic Thin Films

We now turn to the physically relevant problem using the geometrically linear theory of martensites; i.e., $\varphi(\mathbf{F}) = \varphi^{\text{lin}}(\mathbf{e}[\mathbf{F}])$ and $\mathbf{e}$ is the linear strain (see (2.2)). To describe a martensite, the energy density is endowed with a multi-well structure - one well for each phase or variant and has the form in (2.9); i.e.,

$$\varphi^{\text{lin}}(\mathbf{e}) = \min_{i=1,\cdots,k} \left\{ \frac{1}{2} |\mathbf{e} - \mathbf{e}^{(i)}|^2 \right\} \tag{4.125}$$

where $\mathbf{e}^{(i)}$ is the transformation strain for $i = 1, \cdots, k$. Notice that we have restricted our analysis to some fixed temperature below the transformation temperature, and have assumed elastic constants are equal to the identity since we are only interested in the stress-free configuration.

Shape-memory thin films are often made by sputtering [44, 59, 42, 52, 24, 23]. The grains in these films are typically columnar (e.g., see Figure 2 of [44]). So we assume

$$\varphi^{\text{lin}}(\mathbf{e}, \frac{\mathbf{z}_p}{d}) = \varphi^{\text{lin}} \left(\mathbf{R}^T(\frac{\mathbf{z}_p}{d})\, \mathbf{e}\, \mathbf{R}(\frac{\mathbf{z}_p}{d}) \right)$$

where $\mathbf{R} : I\!R^2 \to \mathrm{SO}(3)$ is a given function describing texture and is assumed to be periodic with period $Z = [0,1]^2$.

Let us consider the single crystal film first. Set Π be the matrix that projects any 3×3 matrix into 3×2 matrix

$$\Pi = \begin{pmatrix} 1 & 0 \\ 0 & 1 \\ 0 & 0 \end{pmatrix}.$$

Then,

$$\begin{aligned} \varphi_0(\bar{\mathbf{F}}) &= \inf_{\mathbf{b} \in I\!R^3} \varphi^{\text{lin}} \left(\begin{array}{c|c} \frac{1}{2}(\bar{\mathbf{F}}_p + \bar{\mathbf{F}}_p^T) - \Pi^T\Pi & \frac{1}{2}(\mathbf{b}_p + \mathbf{F}_{3p}) \\ \hline \frac{1}{2}(\mathbf{b}_p + \mathbf{F}_{3p})^T & b_3 - 1 \end{array} \right) \\ &= \inf_{\mathbf{a} \in I\!R^3} \varphi^{\text{lin}} \left(\begin{array}{c|c} \bar{\mathbf{e}} & \mathbf{a}_p \\ \hline \mathbf{a}_p^T & a_{33} \end{array} \right) = \varphi_0^{\text{lin}}(\bar{\mathbf{e}}) \end{aligned} \qquad (4.126)$$

where $\bar{\mathbf{F}}_p = \Pi^T \mathbf{F} \Pi$, $\bar{\mathbf{e}} = \Pi^T \mathbf{e} \Pi$; $\mathbf{F}_{3p} = (F_{31}, F_{32})^T$, $\mathbf{b}_p = (b_1, b_2)^T$ and $\mathbf{a}_p = (a_1, a_2)^T$. For the multi-well energy density defined by (4.125), φ_0^{lin} can be shown to be

$$\varphi_0^{\text{lin}}(\bar{\mathbf{e}}) = \min_{i=1,\cdots,k} \left\{ \frac{1}{2} |\bar{\mathbf{e}} - \bar{\mathbf{e}}^{(i)}|^2 \right\} \qquad (4.127)$$

$$\bar{\mathbf{e}}^{(i)} = \Pi^T \mathbf{e}^{(i)} \Pi. \qquad (4.128)$$

We define $\mathcal{S}_f$, *the set of recoverable strains in a single crystal film* with orientation $\mathbf{e}_3$, to be

$$\mathcal{S}_f = \{ \bar{\mathbf{e}} : Q\varphi_0^{\text{lin}}(\bar{\mathbf{e}}) = 0 \}.$$

This is exactly the set of strains that the material can accommodate by making a mixture of martensitic variants. In general, this set $\mathcal{S}_f$ is hard to determine. However, if all variants $\bar{\mathbf{e}}^{(i)}$ are pair-wise compatible; i.e., they satisfy (2.13) for all $i, j = 1, \cdots, k$, then the associated $\mathcal{S}_f$ is simply their convex hull [9] as we described in Chapter 3. One can show that this is true for materials undergoing cubic-tetragonal, cubic-trigonal and cubic-orthorhombic transformation irrespective of the orientation of the film. Unfortunately, cubic-to-monoclinic martensites have transformation strains that are not pair-wise compatible in general. But they can be compatible in certain orientations. Indeed, let $\mathbf{R}$ denote the crystal orientation, the orientation that takes the film basis $\{\mathbf{e}_1, \mathbf{e}_2, \mathbf{e}_3\}$ to the crystal basis $\{\mathbf{f}_1, \mathbf{f}_2, \mathbf{f}_3\}$, $\mathbf{f}_i = \mathbf{R}\mathbf{e}_i$ for $i = 1, 2, 3$, and notice that

$$\frac{1}{2}|\mathbf{R}^T\mathbf{e}\mathbf{R} - \mathbf{e}^{(i)}|^2 = \frac{1}{2}|\mathbf{e} - \mathbf{R}\mathbf{e}^{(i)}\mathbf{R}^T|^2 = \frac{1}{2}|\mathbf{e} - \mathbf{U}^{(i)}|^2 \tag{4.129}$$

where $\mathbf{U}^{(i)} = \mathbf{R}\mathbf{e}^{(i)}\mathbf{R}^T$. It is well known that two 2×2 symmetric matrices $\mathbf{U}$ and $\mathbf{V}$ are compatible if and only if $\det(\mathbf{U} - \mathbf{V}) \leq 0$ [47]. Set $\mathbf{f}_i^* = \mathbf{R}^T\mathbf{e}_i$ for $i = 1, 2, 3$ and $\mathbf{A} = (\mathbf{e}^{(i)} - \mathbf{e}^{(j)})$, we have

$$\begin{aligned} \det(\Pi^T\mathbf{R}\mathbf{A}\mathbf{R}^T\Pi) \leq 0 \quad &\Longleftrightarrow \quad \det\begin{pmatrix} \mathbf{f}_1^* \cdot \mathbf{A}\mathbf{f}_1^* & \mathbf{f}_1^* \cdot \mathbf{A}\mathbf{f}_2^* \\ \mathbf{f}_2^* \cdot \mathbf{A}\mathbf{f}_1^* & \mathbf{f}_2^* \cdot \mathbf{A}\mathbf{f}_2^* \end{pmatrix} \leq 0 \\ &\Longleftrightarrow \quad \mathbf{f}_3^* \cdot \operatorname{adj}(\mathbf{e}^{(i)} - \mathbf{e}^{(j)})\, \mathbf{f}_3^* \leq 0. \end{aligned} \tag{4.130}$$

It follows that $\mathcal{S}_f$ is the convex hull of transformation strains $\Pi^T\mathbf{U}^{(i)}\Pi$ if (4.130) is satisfied for all $i, j = 1, \cdots, k$. The vector $\mathbf{f}_3^*$ is interpreted as follows. Let {hkl} denote the thin film normal in the cubic crystal basis; i.e.,

$$\mathbf{e}_3 \;\|\; h\,\mathbf{f}_1 + k\,\mathbf{f}_2 + l\,\mathbf{f}_3.$$

Using the definition of $\mathbf{f}_i$ and $\mathbf{f}_i^*$ yields

$$\mathbf{f}_3^* \;\|\; h\,\mathbf{e}_1 + k\,\mathbf{e}_2 + l\,\mathbf{e}_3.$$

It is also very important to know what crystal orientations lead to compatible wells and we can then determine $\mathcal{S}_f$. In fact, it can be shown that all pairs of monoclinic variants are pair-wise compatible for {100} and {110} films in Ti-Ni and {110} and {111} films in Cu-Zn-Al. In contrast, not all pairs are compatible for {111} films in

Ti-Ni and {100} films in Cu-Zn-Al. However, the following set of variants which are pair-wise thin-film compatible in {111} films in Ti-Ni:

$$\begin{array}{l}
\begin{pmatrix} \alpha & -\delta & -\epsilon \\ -\delta & \alpha & \epsilon \\ -\epsilon & \epsilon & \beta \end{pmatrix}, \begin{pmatrix} \alpha & -\delta & \epsilon \\ -\delta & \alpha & -\epsilon \\ \epsilon & -\epsilon & \beta \end{pmatrix}, \begin{pmatrix} \alpha & -\epsilon & -\delta \\ -\epsilon & \beta & \epsilon \\ -\delta & \epsilon & \alpha \end{pmatrix}, \\
\begin{pmatrix} \alpha & \epsilon & -\delta \\ \epsilon & \beta & -\epsilon \\ -\delta & -\epsilon & \alpha \end{pmatrix}, \begin{pmatrix} \beta & -\epsilon & \epsilon \\ -\epsilon & \alpha & -\delta \\ \epsilon & -\delta & \alpha \end{pmatrix}, \begin{pmatrix} \beta & \epsilon & -\epsilon \\ \epsilon & \alpha & -\delta \\ -\epsilon & -\delta & \alpha \end{pmatrix},
\end{array} \tag{4.131}$$

and in {100} films in Cu-Zn-Al:

$$\begin{array}{l}
\begin{pmatrix} \alpha+\epsilon & \delta & 0 \\ \delta & \alpha-\epsilon & 0 \\ 0 & 0 & \beta \end{pmatrix}, \begin{pmatrix} \alpha-\epsilon & \delta & 0 \\ \delta & \alpha+\epsilon & 0 \\ 0 & 0 & \beta \end{pmatrix}, \\
\begin{pmatrix} \alpha+\epsilon & -\delta & 0 \\ -\delta & \alpha-\epsilon & 0 \\ 0 & 0 & \beta \end{pmatrix}, \begin{pmatrix} \alpha-\epsilon & -\delta & 0 \\ -\delta & \alpha+\epsilon & 0 \\ 0 & 0 & \beta \end{pmatrix}.
\end{array} \tag{4.132}$$

Consequently, $\mathcal{S}_f$ contains their convex hulls. We will use (4.131) and (4.132) for calculating Table 4.2 later.

We now turn to polycrystalline thin films. We define the *set of recoverable strains of a polycrystalline thin film*

$$\mathcal{P}_f = \{\bar{\mathbf{e}} : \bar{\varphi}(\bar{\mathbf{e}}) = 0\}. \tag{4.133}$$

Our task is to determine the set $\mathcal{P}_f$. However, this is very difficult since it requires us to solve the nonlinear homogenization problem. One alternate, as we did in Chapter 3, is to estimate the set $\mathcal{P}_f$ using texture-independent bounds. The bound which we believe to be the most useful bound is the Taylor estimate based on the use of a constant-strain test field. So it is an upper bound for $\bar{\varphi}$ but is the inner bound for $\mathcal{P}_f$.

Indeed, in our model example above, one can show that the exact recoverable strain is the same as that predicted using Taylor estimate for $\beta = 0$ and ∞. Unfortunately, the Taylor estimate is only meaningful for homogenization; and consequently, there is no analogy for the case $0 < \beta < \infty$ since homogenization and thin-film limit are taken into account together.

We now give the expression of the Taylor estimate on two extreme cases: $\beta = 0$ and $\beta = \infty$ and assume $\alpha = \frac{\kappa}{d} \xrightarrow{h} 0$ in both cases. Consider $\beta = 0$ first. If all grains are columnar, then the Taylor estimate on the set $\mathcal{P}_f$ is

$$\mathcal{T}^0 = \bigcap_{\mathbf{z}_p \in Z} \mathcal{S}_f(\mathbf{z}_p) = \{\bar{\mathbf{e}} : Q\varphi_0^{\text{lin}}(\bar{\mathbf{e}}; \mathbf{R}(\mathbf{z}_p)) = 0, \quad \text{for a.e. } \mathbf{z}_p \in Z\} \tag{4.134}$$

where

$$\varphi_0^{\text{lin}}(\bar{\mathbf{e}}; \mathbf{R}(\mathbf{z}_p)) = \min_{i=1,\cdots,k} \frac{1}{2} \left| \bar{\mathbf{e}} - \Pi^T(\mathbf{R}(\mathbf{z}_p)\mathbf{e}^{(i)}\mathbf{R}^T(\mathbf{z}_p))\Pi \right|^2. \tag{4.135}$$

Clearly, the average strain $\bar{\mathbf{e}}$ is recoverable in a polycrystalline film if it is recoverable in each grain (or in a.e. $\mathbf{z}_p$). Further, in sputtered films, very often all grains have a common axis {hkl} (the film normal). Therefore, as we describe above, the set $\mathcal{S}_f(\mathbf{z}_p)$ can be determined exactly for all $\mathbf{z}_p$ in (4.134) for certain textured cubic-monoclinic films. Consequently, $\mathcal{T}^0$ is fully determined.

Consider $\beta = \infty$ and assume all grains are columnar. Let $\mathcal{P}$ be the set of recoverable strains in bulk or thick films: $\mathcal{P} = \{\mathbf{e} : \varphi^H(\mathbf{e}) = 0\}$ where φ^H is given by $(4.104)_3$ in terms of geometrically linear theory. Then, it can be shown easily that

$$\Pi^T \mathcal{P} \Pi = \{\bar{\mathbf{e}} : \varphi_0^H(\bar{\mathbf{e}}) = 0\}.$$

So if this function φ_0^H is convex, then it implies $\mathcal{P}_f = \{\bar{\mathbf{e}} : Q\varphi_0^H(\bar{\mathbf{e}}) = 0\} = \Pi^T \mathcal{P} \Pi$. But in general $\mathcal{P}_f \supset \Pi^T \mathcal{P} \Pi \supset \Pi^T \mathcal{T}^\infty \Pi$ where $\mathcal{T}^\infty$ is the Taylor estimate on $\mathcal{P}$ and is

Texture	Recoverable Strains (%)			
	Ti-Ni		Cu-Zn-Al	
	ϵ_R^∞	ϵ_R^0	ϵ_R^∞	ϵ_R^0
random	2.3	2.3	1.3	1.7
{111} film	5.3	8.1	1.9	5.9
{100} film	2.3	2.3	7.1	7.1
{110} sputtered film	2.3	2.3	1.7	1.7

Table 4.2: The predicted uniaxial recoverable extension for various textures. ϵ_R^∞ and ϵ_R^0 are the inner estimate and inner bound for films with $\beta = \infty$ and $\beta = 0$, respectively.

given by

$$\mathcal{T}^\infty = \bigcap_{\mathbf{z}_p \in Z} \mathcal{S}(\mathbf{z}_p) = \{\mathbf{e} : Q\varphi^{\mathrm{lin}}(\mathbf{R}(\mathbf{z}_p)^T \mathbf{e} \mathbf{R}(\mathbf{z}_p)) = 0 \;\text{ for a.e. } \mathbf{z}_p \in Z\}. \tag{4.136}$$

When subjected to uniaxial in-plane tension in the ξ direction, the Taylor bound of maximum recoverable extension is

$$\begin{aligned} e_R^0 &= \max_{\bar{\mathbf{e}} \in \mathcal{T}^0} (\xi \cdot \bar{\mathbf{e}}\, \xi) && \text{for } \beta = 0, \\ e_R^\infty &= \max_{\bar{\mathbf{e}} \in \Pi^T \mathcal{T}^\infty \Pi} (\xi \cdot \bar{\mathbf{e}}\, \xi) && \text{for } \beta = \infty. \end{aligned} \tag{4.137}$$

Table 4.2 contrasts the behavior of films with long or rod-like ($h >> d$) grains and films with flat or pancake shaped ($h << d$) grains [93]. It lists the predicted recoverable strains for films with different textures in Ti-Ni and Cu-Zn-Al. Note that they are larger for flat grains compared to long grains as we expected. We also note here that neither the random nor {110} sputtered texture which is common for BCC materials [40, 96] are ideal textures for large recoverable strain. The ideal textures appear to be {100} for Cu-Zn-Al (this texture can be produced by melt-spinning) and {111} for Ti-Ni. However, depending on the deposition technique, it is common that the film thickness and grain size are on the same order. This gives finite value $\beta > 0$. Unfortunately, we do not know any general method to estimate recoverable strains for this case since homogenization and thin-film limit are taken into account together and can not be treated separately. Further, we also do not know the critical point β, if any, such that above it one should use ϵ_R^∞ for thick films and far below it

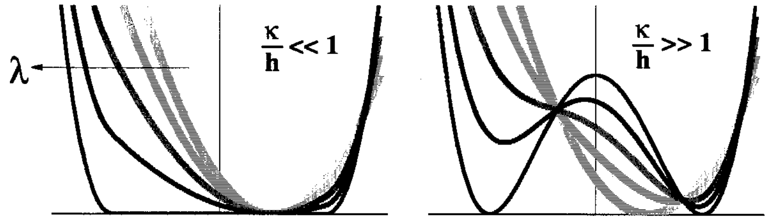

Figure 4.3: The effective behavior of a multilayer thin film is determined by the energies above for small and large values of $\frac{\kappa}{h}$.

one should use ϵ_R^0 for thin films.

Before closing this subsection, we should mention the effect of the ratio $\frac{\kappa}{d}$ of the size of the microstructure to that of the grain. Above, we took this ratio to be zero; however, this may not be true when the grain size becomes very small (on the order of tens of nanometer). From Theorem 1 ($\kappa >> d$), it costs materials more energy to form microstructure inside each grain and consequently strains can not be recovered unless the texture is exceptional. The analysis on the case of comparable κ and d is difficult, but it interpolates the two extreme cases.

4.8 Multilayers

Consider a multilayer film made up of a finite number of alternating layers of a martensitic material and a purely elastic material. Let λ be the volume fraction of the martensitic material and let ϵ_m be the mismatch strain of the elastic material relative to the austenite phase of the martensitic material. The effective behavior is some combination of the behavior of these two materials; however, the nature of the behavior depends on the ratio $\alpha' = \frac{\kappa}{h}$ of the microstructure size to the thickness. For example, assume the local energy density $\varphi : I\!R^2 \times (0,1) \to I\!R$ has the following form

$$\varphi(\mathbf{f}, z_3) = \begin{cases} \varphi_{\text{mart}}(\mathbf{f}) = \frac{1}{2}((f_1^2 - 1)^2 + f_2^2), & \text{for } \frac{m-1}{M} \leq z_3 < \frac{(m-1)+\lambda}{M}, \\ \varphi_{\text{elas}}(\mathbf{f}) = \frac{1}{2}((f_1 - \epsilon_m)^2 + f_2^2), & \text{for } \frac{(m-1)+\lambda}{M} \leq z_3 < \frac{m}{M} \end{cases} \tag{4.138}$$

for $m = 1, \cdots, M$. From Theorem 4, the effective energy densities for small and large values of α' are given by

$$\begin{aligned}\bar{\varphi}^0(\xi) &= \frac{\lambda}{2}\left\{(\xi^2-1)_+\right\}^2 + \frac{1-\lambda}{2}(\xi-\epsilon_m)^2 \qquad \text{for } \alpha' = 0,\\ \bar{\varphi}^\infty(\xi) &= Q\left\{\frac{\lambda}{2}(\xi^2-1)^2 + \frac{1-\lambda}{2}(\xi-\epsilon_m)^2\right\} \qquad \text{for } \alpha' = \infty.\end{aligned}$$

The result is also schematically shown in Figure 4.3. The effective energy for α' small is shown on the left while that for α' large is obtained by the quasi-convexification (or convexification in this case) of the multi-well energy shown on the right-hand side of Figure 4.3. The thin dark line is the energy of the martensitic material and the thick light line is the energy of the elastic material. The behavior of the multilayer is shown by lines of increasing greylevel for decreasing volume fraction λ (also see [10]). For small α', the martensitic material freely forms microstructure and the multilayer is like an elastic material with soft-modulus. For large α' on the other hand, the multilayer behaves like a phase transforming material: it has two variants with transformation strains which may be different from that of the original martensitic material, and one variant is preferred over the other. Hence, this multilayer film will display a two-way shape-memory effect. Further notice that the multilayer is internally stressed so that the minimum energy is not zero. Finally, the multilayer can form "macroscopic twins": these are not twins confined to the martensitic material but encompass both the elastic and the martensitic material. Thus, multilayers promise to be a means of making apparently new materials with interesting and novel properties.

Chapter 5 Discussion and Conclusion

We have investigated the effect of texture on SME in polycrystals. We start with bulk polycrystals - sheets, strips, wires and tubes. We use a theoretical framework to quantify recoverable strain and then use inner and outer bounds to estimate it. We demonstrate with examples that the inner bound accounts for the intergranular constraints and consequently provides a reasonable estimate for the actual recoverable strain while the outer bound ignores these constraints and is a large overestimate (also see [12]). In the case of a cubic to monoclinic transformation, our inner bound becomes conservative (because we replace the unknown set $\mathcal{S}_{\text{mono}}$ with the smaller set $\mathcal{S}_{\text{orth}}$); so we supplement the inner bound with an inner estimate. We compare the predictions of the inner bound and estimate with the experimental observations of Zhao and Beyer [100, 101] as well as Inoue *et al.* [43].

The inner bound and estimate are quite easy to calculate – they can be written as linear programming problems – and incorporate some easily measurable information about the texture. Therefore, these are ideal tools to study the effect of texture on SME. We demonstrate this with specific calculations focused on Ti-Ni and Cu-Zn-Al. Both these alloys undergo cubic to monoclinic transformation, recover similar strains as single crystals and are predicted to recover similar strains as random polycrystals. Yet, their observed behavior is widely varied. Figure 3.13, Figure 3.14 and Table 3.3 shed light on the striking contrast in SME between these two alloys. Figure 3.15 demonstrates that even the qualitative behavior of combined tension-torsion can critically depend on the texture.

We then trun to polycrystalline thin films. We derive a theory for the effective behavior of a heterogeneous thin film with three competing length scales: the film thickness (h), the length scales of heterogeneity (d) and material microstructure (κ). We start with three-dimensional nonhomogeneous nonlinear elasticity enhanced with an interfacial energy of the van der Waals type (4.2), and derive the effective energy density as all length scales tend to zero with given limiting ratios. We do not require any priori selection of asymptotic expansion or ansatz in deriving our results. We show that the macroscopic behavior of the film is determined by the effective energy density $\bar{\varphi}$. It describes the overall behavior of the film after taking into account the effect of martensitic microstructure, grains and multilayers. The most important result is that $\bar{\varphi}$ depends qualitatively on the relative magnitudes of length scales and we summarize our results in Table 4.1.

We demonstrate with an example that the recoverable strain can crucially depend on the ratio of the film thickness to the typical grain size. Table 4.2 contrasts the behavior of films with long or rod-like grains and films with flat or pancake shaped grains. It lists the predicted recoverable strains for films with different textures in Ti-Ni and Cu-Zn-Al. We also show that a multilayer thin film made of a shape-memory material and a purely elastic material can display very interesting behavior depending on the ratio $\frac{\kappa}{h}$.

The following is a list of our main conclusions and suggestions.

- In Ti-Ni, the texture that develops during rolling, extrusion and drawing is extremely favorable from the point of view of large recoverable strains. In contrast, in Cu-Zn-Al and other Cu-based SMAs the texture that develops during these processes is rather unfavorable for SME.

- In Ti-Ni, the α-fiber I rolling texture has the largest uniaxial recoverable strain in the RD and TD. Thus, this texture is ideal for applications which require SME in only one direction. On the other hand, the γ-fiber rolling texture has relatively large recoverable strains and has little in-plane anisotropy. Hence, this texture is ideal for applications which require SME in multiple directions.

- In Cu-Zn-Al and other Cu-based SMAs, the SME can be improved in rolled sheets if one can make either the η-fiber texture or the α-fiber restricted to $\{001\}\langle 110\rangle - \{112\}\langle 110\rangle$. In the later case, relatively large recoverable strain is predicted around 45° from the RD.

- {100} solidification texture shows large recoverable strain for Cu-based SMAs but not for Ti-Ni ribbons.

- Typically, the recoverable torsion is quite small. In wires, rods and tubes with random or $\langle 110 \rangle$ drawing texture, the recoverable angle of twist decreases with increasing applied uniaxial extension while the behavior is reversed for $\langle 100 \rangle$ texture.

- Both Ti-Ni-based and Cu-based SMAs recover comparatively small strains in thin films owing to the unfavorable {110} or random sputtering texture. Ti-Ni films with {111} texture and Cu-based SMA films with {100} texture are predicted to have large recoverable strains.

- In view of large recoverable strains, flat grains are preferable to long grains in columnar films.

- Multilayer thin films provide a promising avenue for making materials with novel properties.

We conclude with a few comments.

Other Models

Various authors [66, 45] have used a model that is equivalent to what we call the outer bound to predict the effect of texture on recoverable strain. This bound ignores the constraints of neighboring grains which turn out to be very important and, consequently, their predictions are much larger (often by a factor of two) than the observed recoverable strains.

Inoue *et al.* [43] have used a different model, which they found agreed well with their observations. In the language of this paper, rather than using the set $\mathcal{S}$ for a single crystal, they use only a small subset of it, the size of which is determined by a parameter q. They then average over the grains; in other words they use an outer bound based on this smaller set. In the examples they consider, the underestimate in the single crystal for a choice $q = 0.5$ in each grain compensates for the overestimate inherent in the outer bound, and they obtain very good agreement with experiment. However, it is unclear whether this choice gives good results in other situations, especially for different materials, textures and multiaxial loading.

R-phase Ti-Ni

Ti-Ni alloys often transform from the cubic to a trigonal R-phase before transforming to the monoclinic martensite [60, 62, 65]. This cubic-trigonal transformation also display SME and superelasticity. Though the strains are smaller, this transformation is often preferable compared to the cubic-monoclinic transformation in view of small hysteresis and ease of control [74]. According to the symmetry arguments of Bhattacharya and Kohn [11], a random polycrystal of cubic-trigonal material will not display any SME. However, a polycrystalline wire with $\langle 111 \rangle$ texture has about 0.9% recoverable uniaxial strain. A rolled sheet with γ-fiber texture also has a nontrivial inner bound of about 0.2% recoverable extension in any rolling plane direction. Many shape-memory wires do possess the $\langle 111 \rangle$ texture and once again this prediction is consistent with observation. Thus, texture produces the good behavior in Ti-Ni even in the case of the R-phase.

Texture Formation

Various researchers are conducting experiments to systematically study the effect of texture on SME. Apart from those cited above, we report on the interesting work of Matsumura *et al.* [56] on rolled sheets of Fe-Mn-Si alloys. This alloy undergoes a face-centered-cubic (FCC) to hexagonal-close-packed (HCP) transformation. By extracting specimens from different parts, Matsumura *et al.* have found that the surface layer with a shear texture has a larger SME than the less anisotropic mid-thickness layer. This suggests an opportunity to improve shape-memory behavior by targeting special textures using novel processing techniques.

Effective Moduli of Thin Films

The theoretical framework developed in Chapter 4 can also be used to study the effective conductivity or elastic modulus of linear composites. We show in [92] that in general the effective conductivity of composites made of anisotropic materials can depend on the ratio $\beta = \frac{h}{d}$ (the film thickness to the grain size). It is clear that similar results must hold for elasticity; and there is some suggestive experimental evidence in this direction. However, optimal bounds exploring the whole range of $\frac{h}{d}$ still generally remain open due to reasons discussed at the end of Section 4.7.1. An exception is a composite made of two isotropic conductors; Damlamian and Vogelius [26] have obtained optimal bounds for a composite thin structure. They consider the case $\varphi = \varphi(\mathbf{f}, \frac{\mathbf{z}_p}{h}, z_3)$ ($\beta = 1$ in our notation and fully three dimensions). However, their optimal bounds are β-independent and hence their bounds hold for all β. Further, their optimal microstructure are z_3-independent. Proposition 2 in [92] shows that their β-independent bound may not be optimal if the conductivity is anisotropic and the film normal is not an eigenvector of the conductivity tensor. We speculate that their lower bound is optimal only for $\beta = 0$ and upper bound only for $\beta = \infty$.

Bibliography

[1] E. Acerbi, G. Buttazzo, and Percivale. A Variational Definition of the Strain Energy for an Elastic String. *J. Elasticity*, **25**:137–148, 1991.

[2] E. Acerbi and N. Fusco. Semicontinuity Problems in the Calculus of Variations. *Arch. Rat. Mech. Anal.*, **86**:125–145, 1984.

[3] G. Arlt. Twinning in the Ferroelectric and Ferroelastic Ceramics: Stress Relief. *J. Mater. Sci.*, **25**:2655–2666, 1990.

[4] H. Attouch. *Variational Convergence for Functions and Operators.* Pitman, London, 1984.

[5] J. M. Ball and R. D. James. Fine Phase Mixtures as Minimizers of Energy. *Arch. Rat. Mech. Anal.*, **100**:13–52, 1987.

[6] J. M. Ball and R. D. James. Proposed Experimental Tests of a Theory of Fine Microstructure and the Two Well Problem. *Phil. Trans. Royal Soc. London A*, **338**:389–450, 1992.

[7] J. M. Ball and F. Murat. $W^{1,p}$-quasiconvexity and Variational Problems for Multiple Integrals. *J. Funct. Anal.*, **58**:225–253, 1984.

[8] K. Bhattacharya. Self-accommodation in Martensite. *Arch. Rat. Mech. Anal.*, **120**:201–244, 1992.

[9] K. Bhattacharya. Comparison of the Geometrically Nonlinear and Linear Theories of Martensitic Transformation. *Cont. Mech. Thermodyn.*, **5**:205–242, 1993.

[10] K. Bhattacharya and R. D. James. A Theory of Thin Films of Martensitic Materials with Applications to Microactuators. *To appear in J. Mech. Phys. Solids*, 1998.

[11] K. Bhattacharya and R. V. Kohn. Symmetry, Texture and the Recoverable Strain of Shape-Memory Polycrystals. *Acta Mater.*, **44**:529–542, 1996.

[12] K. Bhattacharya and R. V. Kohn. Elastic Energy Minimization and the Recoverable Strains of Polycrystalline Shape-Memory Materials. *Arch. Rat. Mech. Anal.*, **139**:99–180, 1997.

[13] J. Bohong and T. Y. Hsu. Influence of Order, Grain Size and Pre-strain on Shape Memory Effect in Cu-Zn-Al Alloys. *Mater. Sci. Forum*, **56-58**:457–462, 1990.

[14] A. Braides. Private Communciation. 1998.

[15] A. Braides. Homogenization of Some Almost Periodic Coercive Functional. *Rend. Accad. Naz. Sci. XL*, **103**:313–322, 1985.

[16] A. Braides and A. Defranceschi. *Homogenization of Multiple Integrals.* Oxford University Press, Oxford, 1998.

[17] A. Braides, I. Fonseca, and G. Francfort. Asymptotic Models for Thin Structures. 1998. In preparation.

[18] O. P. Bruno, F. Reitich, and P. H. Leo. The Overall Elastic Energy of Polycrystalline Martensitic Solids. *J. Mech. Phys. Solids*, **44**:1051–1101, 1996.

[19] H. J. Bunge. *Texture Analysis in Materials Science.* Butterworths, London, 1982.

[20] D. Caillerie. Thin Elastic and Periodic Plates. *Math. Meth. in the Appl. Sci.*, **6**:159–191, 1994.

[21] S. Chakravorty. Ph.D. Thesis. University of Illinois at Urbana-Champaign, 1975.

[22] S. Chakravorty and C. M. Wayman. Electron Microscopy of Internally Faulted Cu-Zn-Al Martensite. *Acta Metall.*, **25**:989–1000, 1977.

[23] L. W. Chang and D. S. Grummon. Phase-Transformations in Sputtered Thin-Films of Ti-X(Ni,Cu)(1-X) .2. Displacive Transformations. *Phil. Mag. A*, **76**:191–219, 1997.

[24] L. W. Chang and D. S. Grummon. Structure Evolution in Sputtered Thin-Films of Ti-X(Ni,Cu)(1-X) .1. Diffusive Transformations. *Phil. Mag. A*, **76**:163–189, 1997.

[25] B. Dacorogna. Quasiconvexity and Relaxation of Nonconvex Problems in the Calculus of Variations. *J. Funct. Anal.*, **46**:102–118, 1982.

[26] A. Damlamian and M. Vogelius. Homogenization Limits of Diffusion Equations in Thin Domains. *Mathematical Modeling and Numerical Analysis*, **22**:53–74, 1988.

[27] P. Donner. Microstructure and Phase-Transformation in Meltspun Shape Memory Alloys. *J. de Physique IV, Colloque C4*, **1**:355–360, 1991.

[28] P. Donner and S. Eucken. The Shape Memory Effect in Meltspun Ribbons. *Mater. Sci. Forum*, **56-58**:723–728, 1990.

[29] H. Le Dret and A. Raoult. The Nonlinear Membrane Model as Variational Limit of Nonlinear Three-dimensional Elasticity. *J. Math. Pures. Appl.*, **74**:549–578, 1995.

[30] F. Emren, U. von Schlippenbach, and K. Lücke. Investigation of the Development of the Recrystallization Textures in Deep Drawing Steels by ODF Analysis. *Acta Metall.*, **34**:2105–2117, 1986.

[31] J. L. Ericksen. On the Symmetry of Deformable Crystals. *Arch. Rat. Mech. Anal.*, **72**:1–13, 1979.

[32] J. L. Ericksen. Some Phase Transitions in Crystals. *Arch. Rat. Mech. Anal.*, **73**:99–124, 1980.

[33] S. Eucken, P. Donner, and E. Hornbogen. On Improvement in the Mechanical Properties of Rapidly Solidified Shape Memory Alloys. *Mater. Sci. Engng.*, **98**:469–474, 1988.

[34] S. Eucken and J. Hirsch. The Effect of Textures on Shape Memory Behaviour. *Mater. Sci. Forum*, **56-58**:487–492, 1990.

[35] S. Eucken, J. Hirsch, and E. Hornbogen. Texture and Microstructure of Melt-spun Shape Memory Alloys. *Textures and Microstructures*, **8-9**:415–426, 1988.

[36] I. Fonseca and G. Francfort. 3D-2D Asymptotic Analysis of an Optimal Design Problem for Thin Films. *J. Reine Angew. Math.*, 1998. To appear.

[37] G. A. Francfort and S. Müller. Combined Effects of Homogenization and Singular Perturbations in Elasticity. *J. Reine Angew. Math.*, **454**:1–35, 1994.

[38] E. De Giorgi. Sulla convergenza di alcune successioni di integrali del tipo dell'area. *Rendi Conti di Mat.*, **8**:277–294, 1975.

[39] E. De Giorgi and T. Franzoni. Su un tipo di convergenza variazionale. *Atti. Accad. Naz. Lincei Rend. Cl. Sci. Mat.* (8), **58**:842–850, 1975.

[40] K. R. C. Gisser, J. D. Busch, A. D. Johnson, and A. B. Ellis. Oriented Nickel-Titanium Shape Memory Alloy Films Prepared by Annealing During Deposition. *Appl. Phys. Lett.*, **61**:1632–1634, 1992.

[41] W. F. Hosford. *The Mechanics of Crystals and Textured Polycrystals.* Oxford University Press, New York, 1993.

[42] L. Hou and D. S. Grummon. Transformational Superelasticity in Sputtered Titanium-Nickel Thin Films. *Scripta Metall.*, **33**:989–995, 1995.

[43] H. Inoue, N. Miwa, and N. Inakazu. Texture and Shape Memory Strain in TiNi Alloy Sheets. *Acta Mater.*, **44**:4825–4834, 1996.

[44] A. Ishida, A. Takei, and S. Miyazaki. Shape Memory Thin Film of Ti-Ni Formed by Sputtering. *Thin Solid Films*, **228**:210–214, 1993.

[45] K. Kitamura, S. Miyazaki, H. Iwai, and M. Kohl. Effect of Heat-Treatment on the Texture in Rolled Ti-Ni Thin Plates. In *Proc. Inter. Conf. on Shape Memory and Superelastic Technologies*, Pacific Grove, California, 1997. SMST-97. In press.

[46] K. M. Knowles and D. A. Smith. The Crystallography of the Martensitic Transformation in Equiatomic Nickel-Titanium. *Acta Metall.*, **29**:101–110, 1981.

[47] R. V. Kohn. The Relaxation of a Double-Well Energy. *Cont. Mech. Thermodyn.*, **3**:981–1000, 1991.

[48] R. V. Kohn and B. Niethammer. 1998. In preparation.

[49] R. V. Kohn and M. Vogelius. A New Model for Thin Plates with Rapidly Varying Thickness. *Int. J. Solids & Structures*, **20**:333–350, 1984.

[50] R. V. Kohn and M. Vogelius. A New Model for Thin Plates with Rapidly Varying Thickness II: A Convergence Proof. *Quarterly of Applied Mathematics*, **XLIII**:1–22, 1985.

[51] P. Krulevitch, A. P. Lee, P. B. Ramsey, J. C. Trevino, J. Hamilton, and M. A. Northrup. Thin Film Shape Memory Alloy Microactuators. *Journal of Microelectromechanical Systems*, **5**:270–282, 1996.

[52] P. Krulevitch, P. B. Ramsey, D. M. Makowiecki, A. P. Lee, M. A. Northrup, and G. C. Johnson. Mixed-Sputter Deposition of Ni-Ti-Cu Shape Memory Films. *Thin Solid Films*, **274**:101–105, 1996.

[53] Ch. Lexcellent and P. Vacher. Thermomechanical Behavior of Polycrystalline Shape Memory Alloys Cu-Zn-Al. *Arch. Mech.*, **45**:135–155, 1993.

[54] D. Y. Li, X. F. Wu, and T. Ko. The Texture of Ti-51.5 at.% Ni Rolling Plate and its Effect on the All-Round Shape Memory Effect. *Acta Metall.*, **38**:19–24, 1990.

[55] H. C. Lin and S. K. Wu. The Tensile Behavior of a Cold-Rolled and Reverse-Transformed Equiatomic TiNi Alloy. *Acta Metall.*, **42**:1623–1630, 1994.

[56] O. Matsumura, S. Furusako, T. Furukawa, and H. Otsuka. Formation of Surface Texture and Anisotropy of Shape Memory Effect in an Fe-Mn-Si Alloy. *ISIJ International*, **36**:1103–1108, 1996.

[57] G. W. Milton. A Link between Sets of Tensors Stable under Lamination and Quasiconvexity. *Communications on Pure and Applied Mathematics*, **47**:959–1003, 1994.

[58] S. Mishra, C. Därmann, and K. Lücke. On the Development of the Goss Texture in Iron–3% Silicon. *Acta Metall.*, **32**:2185–2201, 1984.

[59] S. Miyazaki and A. Ishida. Shape Memory Characteristics of Sputter-Deposited Ti-Ni Thin Films. *Mater. Trans., JIM*, **35**:14–19, 1994.

[60] S. Miyazaki, S. Kimura, and K. Otsuka. Shape-Memory Effect and Pseudoelasticity Associated with the R-Phase Transition in Ti-50.5 at.% Ni Single Crystals. *Phil. Mag. A*, **57**:467–478, 1988.

[61] S. Miyazaki, S. Kimura, K. Otsuka, and Y. Suzuki. The Habit Plane and Transformation Strains Associated with the Martensitic Transformation in Ti-Ni Single Crystals. *Scripta Metall.*, **18**:883–888, 1984.

[62] S. Miyazaki and K. Otsuka. Deformation and Transition Behavior Associated with the R-Phase in Ti-Ni Alloys. *Metall. Trans.*, **17A**:53–63, 1986.

[63] S. Miyazaki and K. Otsuka. Development of Shape Memory Alloys. *ISIJ International*, **29**:353–377, 1989.

[64] S. Miyazaki, K. Otsuka, and Y. Suzuki. Transformation Pseudoelasticity and Deformation Behavior in a Ti-50.6 at.% Ni Alloy. *Scripta Metall.*, **15**:287–292, 1981.

[65] S. Miyazaki and C. M. Wayman. The R-Phase Transition and Associated Shape Memory Mechanism in Ti-Ni Single Crystals. *Acta Metall.*, **36**:181–192, 1988.

[66] J. H. Mulder, P. E. Thoma, and J. Beyer. Anisotropy of the Shape Memory Effect in Tension of Cold-Rolled 50.8 Ti 49.2 Ni (at.%) Sheet. *Z. Metallkd.*, **84**:501–508, 1993.

[67] S. Müller. Homogenization of Nonconvex Integral Functionals and Cellular Elastic Materials. *Arch. Rat. Mech. Anal.*, **99**:189–212, 1987.

[68] S. Müller. Reiterated Homogenization. Manuscript, 1998.

[69] T. H. Nam, T. Saburi, Y. Nakata, and K. Shimizu. Shape Memory Characteristics and Lattice Deformation in Ti-Ni-Cu Alloys. *Mater. Trans., JIM*, **31**:1050–1056, 1990.

[70] K. Oishi and L. C. Brown. Stress-Induced Martensite Formation in Cu-Al-Ni Alloys. *Metall. Trans.*, **2**:1971–1977, 1971.

[71] N. Ono. Pseudoelastic Deformation in a Polycrystalline CuAlN Shape Memory Alloy in Comparison with the Modified Taylor Model. *Mat. Trans. Jap. Inst. Metals*, **31**:855–860, 1990.

[72] N. Ono and A. Sato. Plastic Deformation Governed by the Stress Induced Martensitic Transformation in Polycrystals. *Mat. Trans. Jap. Inst. Metals*, **29**:267–273, 1988.

[73] N. Ono, A. Sato, and H. Ohta. A Discussion on the Mechanical Properties of Shape Memory Alloys Based on a Polycrystal Model. *Mat. Trans. Jap. Inst. Metals*, **30**:756–764, 1989.

[74] K. Otsuka. Introduction to the R-Phase Transition. In T. W. Duerig, K. N. Melton, D. Stöckel, and C. M. Wayman, editors, *Engineering Aspects of Shape Memory Alloys*, pages 36–45, London, 1990. Butterworth-Heinemann.

[75] K. Otsuka, T. Nakamura, and K. Shimizu. Electron Microscopy Study of Stress-Induced Acicular β_1' Martensite in Cu-Al-Ni Alloy. *Trans. Jap. Inst. Metals*, **15**:200–210, 1974.

[76] K. Otsuka, H. Sakamoto, and K. Shimizu. Successive Stress-Induced Martensitic Transformations and Associated Transformation Pseudoelasticity in Cu-Al-Ni Alloys. *Acta Metall.*, **27**:585–601, 1979.

[77] K. Otsuka, T. Sawamura, and K. Shimizu. Crystal Structure and Internal Defects of Equiatomic TiNi Martensite. *Phys. Stat. Sol. (a)*, **5**:457–470, 1971.

[78] K. Otsuka and K. Shimizu. Morphology and Crystallography of Thermoelastic Cu-Al-Ni Martensite Analyzed by the Phenomenological Theory. *Trans. Jap. Inst. Metals*, **15**:103–108, 1974.

[79] N. J. Park and H. J. Bunge. Determination of the Orientation Distribution Function of a CuZnAl Shape Memory Alloy. *Z. Metallkd.*, **81**:636–645, 1990.

[80] N. J. Park and H. J. Bunge. Texture Development and Texture Inhomogeneities in a Hot-Rolled CuZnAl Shape Memory Alloy. *J. de Physique IV, Colloque C4*, **1**:323–328, 1991.

[81] N. J. Park and H. J. Bunge. Texture Transformation due to Martensitic Phase Transformation in CuZnAl Shape Memory Alloys. *Mater. Sci. Forum*, **157-162**:563–570, 1994.

[82] N. J. Park, C. Q. Wang, and H. J. Bunge. Texture Development of Cold Drawn Wires in $(\alpha + \beta)$ CuZnAl Shape Memory Alloys. *Mater. Sci. Forum*, **157-162**:827–834, 1994.

[83] P. Perin, G. Bourbon, B. C. Goo, A. Charai, J. Bernardini, and Ch. Lexcellent. Growth and Characterization of Shape Memory Cu-Zn-Al Single Crystals. *J. de Physique IV, Colloque C2*, **5**:263–268, 1995.

[84] M. Piao, K. Otsuka, S. Miyazaki, and H. Horikawa. Mechanism of the A_s Temperature Increase by Pre-deformation in Thermoelastic Alloys. *Mater. Trans., JIM*, **34**:919–929, 1993.

[85] D. Raabe and K. Lücke. Rolling and Annealing Textures of BCC Metals. *Mater. Sci. Forum*, **157-162**:597–610, 1994.

[86] T. Saburi and S. Nenno. The Shape Memory Effect and Related Phenomena. In H. I. Aaronson, D. E. Laughlin, R. F. Sekerka, and C. M. Wayman, editors, *Proc. Int. Conf. on Solid-Solid Phase Transformations*, pages 1455–1479, New York, 1981. The Metall. Soc. AIME.

[87] T. Saburi, T. Tatsumi, and S. Nenno. Effects of Heat Treatment on Mechanical Behavior of Ti-Ni Alloys. *J. de Physique, Colloque C4*, **43**:261–266, 1982.

[88] T. Saburi, Y. Watanabe, and S. Nenno. Morphological Characteristics of the Orthorhombic Martensite in a Shape Memory Ti-Ni-Cu Alloy. *ISIJ International*, **29**:405–411, 1989.

[89] T. Saburi and C. M. Wayman. Crystallographic Similarities in Shape Memory Martensites. *Acta Metall.*, **27**:979–995, 1979.

[90] T. Saburi, M. Yoshida, and S. Nenno. Deformation Behavior of Shape Memory Ti-Ni Alloy Crystals. *Scripta Metall.*, **18**:363–366, 1984.

[91] H. Sakamoto and K. Shimizu. Experimental Investigation on Cyclic Deformation and Fatigue Behavior of Polycrystalline Cu-Al-Ni Shape Memory Alloys above M_s. *Trans. Japan Inst. Metals*, **27**:592–600, 1986.

[92] Y. C. Shu. Heterogeneous Thin Films of Martensitic Materials. 1998. In Preparation.

[93] Y. C. Shu and K. Bhattacharya. The Influence of Texture on the Shape-Memory Effect in Polycrystals. *To appear in Acta Materialia*, 1998.

[94] P. Sittner, Y. Hara, and M. Tokuda. Experimental Study on the Thermoelastic Martensitic Transformation in Shape Memory Alloy Polycrystal Induced by Combined External Forces. *Metall. Trans.*, **26A**:2923–2935, 1995.

[95] V. P. Smyshlyaev and J. R. Willis. A Nonlocal Variational Approach to the Elastic Energy Minimization of Martensitic Polycrystals. *P. Roy. Soc. Lond. A*, **454**:1573–1613, 1998.

[96] Q. Su, S. Z. Hua, and M. Wuttig. Martensitic Transformation in $Ni_{50}Ti_{50}$ Films. *J. Alloys and Compounds*, **211/212**:460–463, 1994.

[97] U. von Schlippenbach, F. Emren, and K. Lücke. Investigation of the Development of the Cold Rolling Texture in Deep Drawing Steels by ODF-Analysis. *Acta Metall.*, **34**:1289–1301, 1986.

[98] P. F. Willemse, B. J. Koopman, and J. Beyer. The Texture Development of Ti-Ni-Cu Wire During Thermomechanical Cycling. *J. de Physique IV, Colloque C4*, **1**:329–333, 1991.

[99] K. Yamauchi, M. Nishida, I. Itai, K. Kitamura, and A. Chiba. Specimen Preparation for Transmission Electron Microscopy of Twins in B19′ Martensite of Ti-Ni Shape Memory Alloys. *Mater. Trans., JIM*, **37**:210–217, 1996.

[100] L. Zhao. Texture Development and Anisotropic Behaviour in a Ti-45Ni-5Cu (at.%) Shape Memory Alloy. Ph.D. Thesis. University of Twente. The Netherlands. 1997.

[101] L. Zhao and J. Beyer. 1998. In preparation.

Appendix A Expression of $\mathcal{S}$

In this appendix, we give the expression for $\mathcal{S}$ in the different cases. In cubic-tetragonal, cubic-trigonal and cubic-orthorhombic transformation, $\mathcal{S}$ is the convex hull of stress-free martensite variants; i.e.,

$$\mathcal{S} = \left\{ e : e = \sum_{i=1}^{k} \mu_i e^{(i)}, \quad \mu_i \geq 0, \ \sum_{i=1}^{k} \mu_i = 1 \right\}. \tag{A.1}$$

In the case of cubic-monoclinic transformation, $\mathcal{S}_{\text{mono}}$ is estimated using the sets we call $\mathcal{S}_{\text{orth}}$ and $\mathcal{S}^{c}_{\text{mono}}$ such that $\mathcal{S}_{\text{orth}} \subset \mathcal{S}_{\text{mono}} \subset \mathcal{S}^{c}_{\text{mono}}$ as described in Section 3.1. We assume $\alpha > \beta$ for Monoclinic-I martensites and $\alpha - \epsilon > \beta$ for Monoclinic-II martensites and use the notation {ijk}=perm{123} to denote that {ijk} is some permutation of {123}; i.e., {ijk} = {123} or {231} or {312}, etc.

Tetragonal Martensite

$$\mathcal{S}_{\text{tetr}} = \left\{ e \left\| \begin{array}{c} e_{11} + e_{22} + e_{33} = 2\alpha + \beta, \\ \min\{\alpha, \beta\} \leq e_{11}, e_{22}, e_{33} \leq \max\{\alpha, \beta\}, \\ e_{12} = e_{13} = e_{23} = 0 \end{array} \right. \right\}. \tag{A.2}$$

Trigonal Martensite

$$\mathcal{S}_{\text{trig}} = \left\{ e \left\| \begin{array}{c} e_{11} = e_{22} = e_{33} = \beta, \\ \min\{-\alpha, 3\alpha\} \leq e_{12} + e_{13} + e_{23} \leq \max\{-\alpha, 3\alpha\}, \\ \min\{-\alpha, 3\alpha\} \leq e_{12} - e_{13} - e_{23} \leq \max\{-\alpha, 3\alpha\}, \\ \min\{-\alpha, 3\alpha\} \leq -e_{12} - e_{13} + e_{23} \leq \max\{-\alpha, 3\alpha\}, \\ \min\{-\alpha, 3\alpha\} \leq -e_{12} + e_{13} - e_{23} \leq \max\{-\alpha, 3\alpha\} \end{array} \right. \right\}. \tag{A.3}$$

Orthorhombic Martensite

$$\mathcal{S}_{\text{orth}} = \left\{ e \;\middle\|\; \begin{array}{c} e_{11} + e_{22} + e_{33} = 2\alpha + \beta, \\ \min\{\alpha, \beta\} \leq e_{11}, e_{22}, e_{33} \leq \max\{\alpha, \beta\}, \\ -(\frac{\alpha - e_{ii}}{\alpha - \beta})\delta \leq e_{jk} \leq (\frac{\alpha - e_{ii}}{\alpha - \beta})\delta, \\ \text{for each } \{\text{ijk}\} = \text{perm}\{123\} \end{array} \right\}. \tag{A.4}$$

Monoclinic-I Martensite

$$\mathcal{S}^{c}_{\text{mono}} = \left\{ e \;\middle\|\; \begin{array}{c} e_{11} + e_{22} + e_{33} = 2\alpha + \beta, \\ \beta \leq e_{11}, e_{22}, e_{33} \leq \alpha, \\ -(\frac{\alpha - e_{ii}}{\alpha - \beta})\delta - (\frac{e_{ii} - \beta}{\alpha - \beta})\epsilon \leq e_{jk} \leq (\frac{\alpha - e_{ii}}{\alpha - \beta})\delta + (\frac{e_{ii} - \beta}{\alpha - \beta})\epsilon, \\ \text{for each } \{\text{ijk}\} = \text{perm}\{123\} \end{array} \right\}. \tag{A.5}$$

Monoclinic-II Martensite

The exact formula for $\mathcal{S}^{c}_{\text{mono}}$ is quite difficult, but the following estimate suffices for our purposes.

$$\mathcal{S}^{c}_{\text{mono}} \subset \left\{ e \;\middle\|\; \begin{array}{c} e_{11} + e_{22} + e_{33} = 2\alpha + \beta, \\ \beta \leq e_{11}, e_{22}, e_{33} \leq \alpha + \epsilon, \\ -(\frac{\alpha + \epsilon - e_{ii}}{\alpha + \epsilon - \beta})\delta \leq e_{jk} \leq (\frac{\alpha + \epsilon - e_{ii}}{\alpha + \epsilon - \beta})\delta, \\ \text{for each } \{\text{ijk}\} = \text{perm}\{123\} \end{array} \right\}. \tag{A.6}$$